Non-linear Composite Shells

Formulation & Implementation

Master Thesis by Peter Wilson

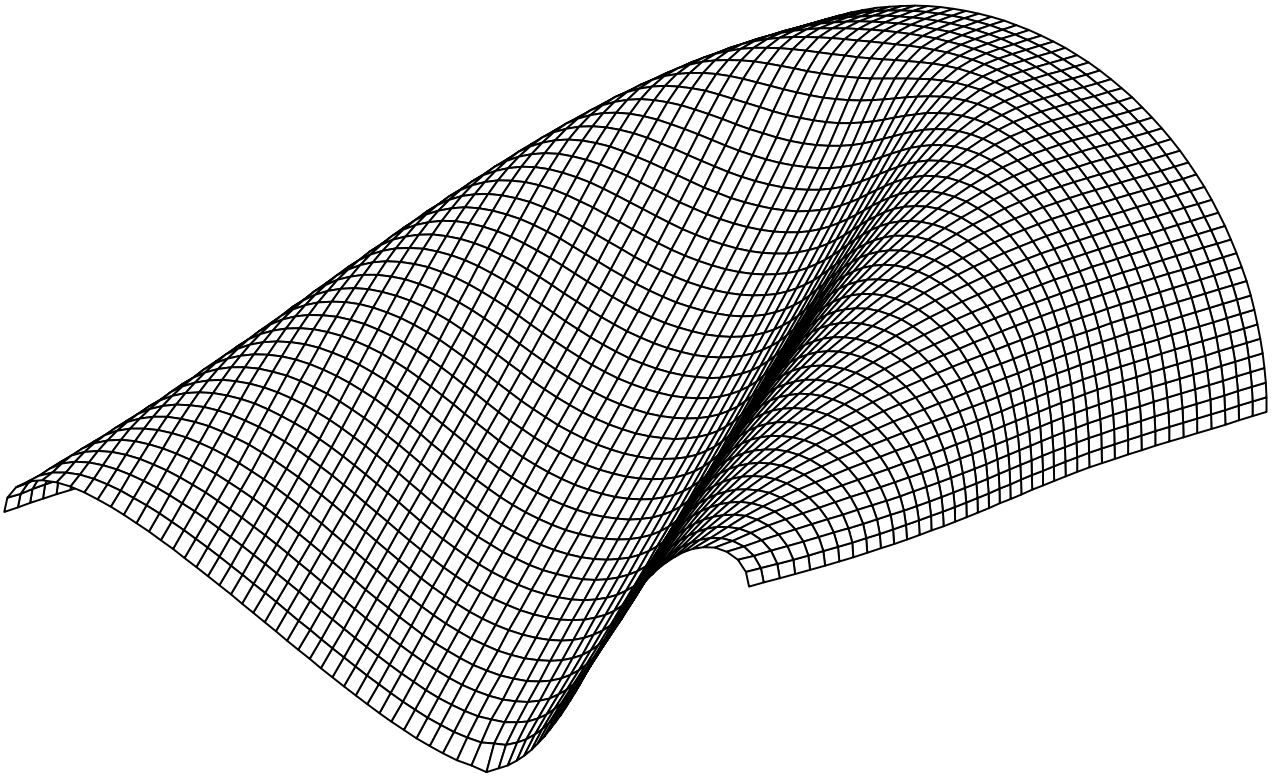

Non-linear Composite Shells

Formulation & Implementation

Submitted to the Department of Civil, Geo and Environmental Engineering
in partial fulfillment of the requirements for the degree of
M.Sc.
at the Technical University of Munich.

Supervised by Andreas Winterstein (MSc)
Prof. Dr.-Ing. Kai-Uwe Bletzinger
Chair of Structural Analysis

Submitted by Peter Wilson
Apianstraße 7
85774 Unterföhring

Submitted on Munich, Datum

Abstract

In this work, a thin quadrilateral shell element implemented in the multiphysics code KRATOS is presented. The element considered is composed of an Assumed Natural Deviatoric Strains (ANDES) membrane formulation and a Discrete Kirchhoff Quadrilateral (DKQ) bending formulation. Both of these formulations are examined, as well as the general implementation of them in the KRATOS code. Finally, the shell element is tested with the well known shell obstacle course and future work pertaining to the element is identified.

Keywords

FEM; Shell structures; ANDES; DKT; DSG

Table of Contents

1 Introduction 1
2 Shell finite elements 2
2.1 Structural modelling with shells 2
2.2 Shell models 3
2.3 Locking in shell finite elements 11
2.4 Shell finite element technologies 13
2.5 Identification of Kratos shell element formulations 19
3 Composite shells 21
3.1 Composite material basics 22
3.2 Orthotropic shell laminates: internal virtual work 27
3.3 Laminate strain and stress recovery 31
3.4 Laminate Tsai-Wu failure criterion 34
4 DSG triangle shell element 36
4.1 Stiffness matrix formulation 36
4.2 Stiffness matrix implementation 39
4.3 Mass matrix formulation and implementation 41
4.4 Stress and strain recovery 43
5 ANDES-DKQ quadrilateral shell element 46
5.1 Stiffness matrix formulation 46
5.2 Stiffness matrix implementation 57
5.3 Mass matrix formulation 60
5.4 Stress and strain recovery 60
6 Composite orthotropic laminates 63
6.1 Formulation 63
6.2 Implementation 64
7 Validation of elements 65
7.1 Static tests: shell obstacle course 65
7.2 Geometically non-linear tests 69
7.3 Dynamic tests 70
7.4 Quantity recovery tests 72
7.5 Composite tests 78
8 Conclusions and Outlook 86
8.1 Future work 86
Appendix A Basic-DKQ formulation 87
Appendix B Basic-T3 formulation 89
Appendix C Analytical membrane analysis of dome 90
Appendix D Analytical solution of Navier supported plate 91

Chapter 1 Introduction

KRATOS is a relatively recent multiphysics code emerging from the International Center for Numerical Methods in Engineering (CIMNE) in Barcelona. Primarily aimed at developers, researchers and students, KRATOS's extensibility accommodates the introduction of new functionalities with relative ease.

The additional functionality considered in this paper is the implementation of a thin quadrilateral shell element. This new contribution fills an existing gap in the structural mechanics capabilities of KRATOS, which is currently missing thin quadrilateral and thick triangular shell elements.

Shell elements themselves result from the combination of membrane and bending behaviours into a single element. The thin quadrilateral shell element presented in this paper consists of an Assumed Natural Deviatoric Strains (ANDES) membrane formulation and a complementing Discrete Kirchhoff Quadrilateral (DKQ) bending formulation. Both of these component formulations are discussed in section 1 of the paper. Following this, a high level overview of the element's implementation in KRATOS is presented in section 2, while section 3 covers element benchmarking with the well known shell obstacle course. Future work is discussed in section 4 of this paper.

Chapter 2 **Shell finite elements**

THE employment of shell structures is ubiquitous throughout both nature and the built environment. Eggs, nuts, blood vessels and cell walls are examples of shell designs being the result of structural optimisation via natural evolution over millennia. It is no doubt that man drew inspiration from the optimal natural shell design and quickly realised the efficacy of the shell structure, perhaps the pre-eminent example of early shell structures is the Roman Pantheon (126). Throughout time, as the understanding of shell structures increased, so did their prevalence, leading to notable structures such as the Hagia Sophia (537), Notre Dame (1345) and St. Peter's Basilica (1626). Indeed, the efficiency of shell structures lies in their high in-plane (membrane) load carrying capacity in slender low-weight constructions. The membrane action serves to stress all fibres approximately equally in the cross section, realising the full mechanical performance of the structure. Contrasting this, shells are incredibly sensitive to a variety of effects such as imperfections, bending, transverse normal forces and support conditions, leading to significant compromise of the membrane structural performance and possibly manifesting in catastrophic failure. To examine one such sensitivity, bending actions result in a non-uniform stressing of material fibres over the cross section, with the outer fibres stressed significantly more than those closer to the neutral axis. Consequently, the limit of the structure in bending is realised when only the outer-most fibre fails instead of the entire cross section of fibres failing under membrane action. This basic example offers a snapshot of the stellar performance of shells juxtaposed against their sensitivity to a multitude of conditions, earning them the title of the *Prima Donna of structures* [35].

2.1. Structural modelling with shells

Although shells present the opportunity of an optimally loaded structure, their delicate position in a sharply varying landscape of performance demands consideration of phenomena critical to the analysis undertaken. When this potentially volatile behaviour is held against the scientific ethos of *everything should be made as simple as possible, but no simpler*, the arising tension is immediately recognized, one that can only be curtailed by an in depth knowledge of the working problem and shells themselves. Within the engineering design context of a particular scenario, there exists as many opportunities to reduce complexity as there are to incorrectly exclude critical phenomena. Typical structural modelling decisions such as: inclusion or

exclusion of inertial and damping effects, non-linear or linear material models, large or small deformation assumptions and dimensional reduction are examples of large brush strokes limiting the canvas of possibilities resolved. Focussing on the rendering of shells, the structural models assumed determine the behaviour they can exhibit.

Inherent in the use of shells in structural models is the concept of dimensional reduction from 3 dimensions to 2 dimensions, relying on the assumption that one dimension (thickness) is significantly smaller than the other two (length and width).

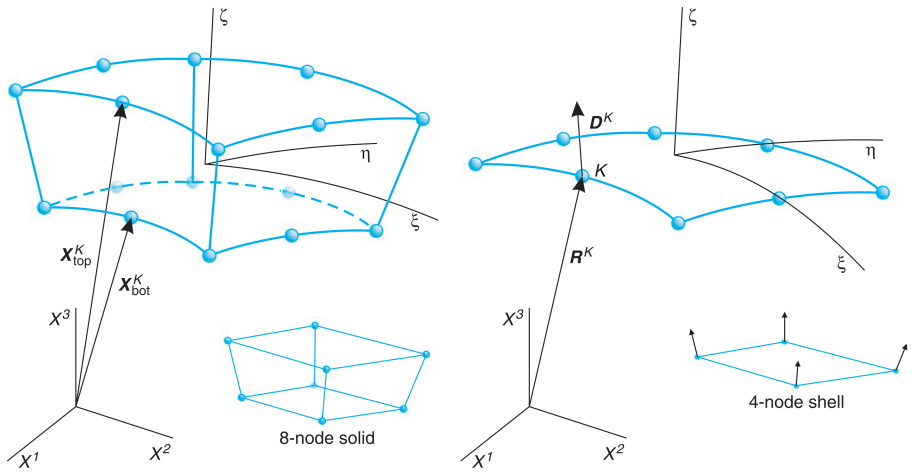

Figure 1 Dimensional reduction of a solid to a shell [8]

Already, it is apparent that the through-thickness response of the shell now must be modelled instead of resolved, with the results now a function of the approximation employed. This apparent simplification promptly begs a key question: what shall the model consider such that it is simple as possible, but not simpler? Can the thickness vary under deformation? Is the shell one uniform material or multi-layered? Is shear deformation of the thickness negligible or not? One may also impose far stricter modelling assumptions by only considering the bending or membrane behaviour of the shell. These common structural modelling decisions, amongst others, have yielded typical shell models.

2.2. Shell models

Commencing in the Renaissance and continuing into the present day, the mathematical development of shell models has facilitated the construction of increasingly elaborate shell structures. The main mathematically-based shell models considered in this work are illustrated below.

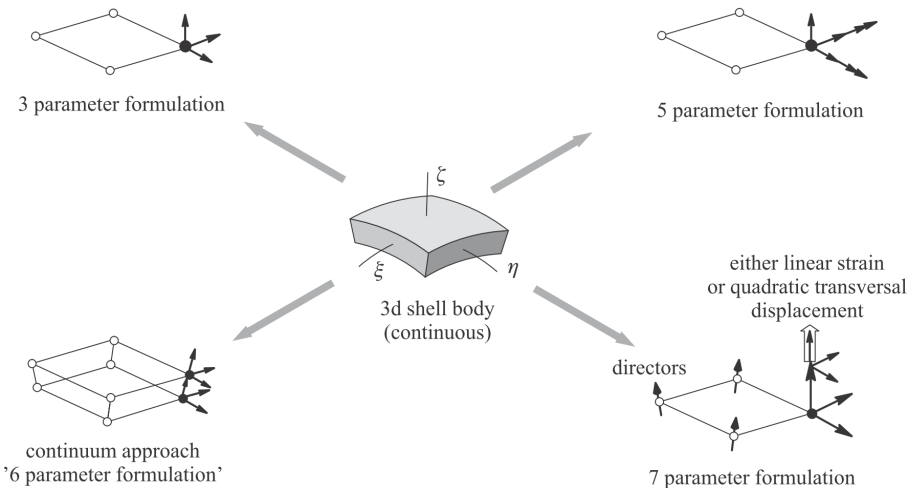

Figure 2 Various shell models [41]

Each of the shell models above are based on different assumptions and physics, which essentially act as a filter of what phenomena the structural model can resolve. These models, as well as the basic membrane model, will be briefly discussed in the following section (further details can be found in References [8] [36] and [16]). To gain further insight, high level formulations of the models are presented with a focus of the mathematical representation of the key assumptions. The follow figure illustrates the configurations and notation of the formulations.

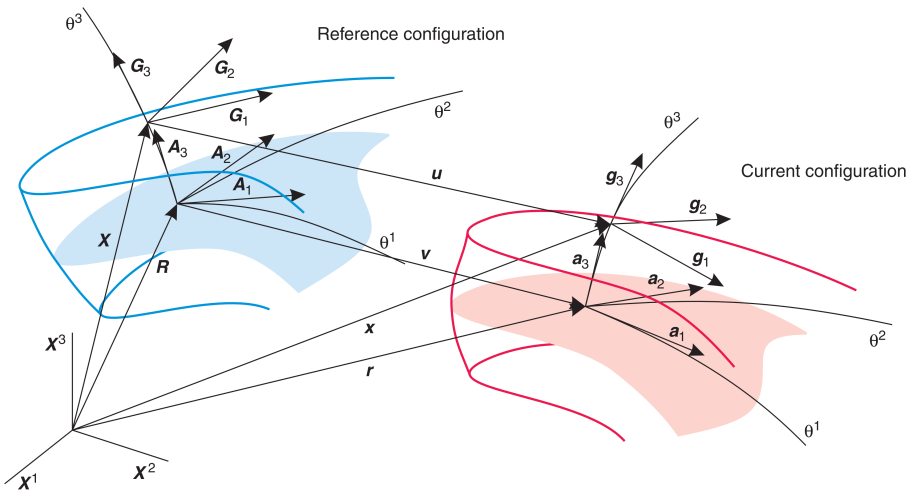

Figure 3 Deformation, reference and current configuration [8]

Quantities in the reference configuration are expressed in upper case while quantities in lower case are in the deformed configuration. The reference shell mid-plane $\theta^3 = 0$ position vector of a point is denoted $\mathbf{R}$, while an arbitrary point is denoted $\mathbf{X}$. Correspondingly, base vectors on the mid-plane are denoted $\mathbf{A}_i$ and $\mathbf{a}_i$ while $\mathbf{G}_i$ and $\mathbf{g}_i$ denote arbitrary base vectors. It is noted that Einstein notation is employed here, with Latin characters corresponding to summation over three dimensions while Greek characters sum over two dimensions. Lastly, $\mathbf{v}$ and $\mathbf{u}$

indicate displacements on the mid-plane and arbitrary location respectively.

2.2.1. Membrane model

Despite not truly being a shell model, the membrane model is the simplest model available as it completely ignores bending behaviour. Thus, the structural behaviour of the whole element is described by in plane components. Typically it is assumed that all stress and strain components are constant over the thickness. A key model choice is the specification of either plane stress or plane strain behaviour which is implemented in material matrix.

Commencing a high level formulation of the membrane model, the assumption of constant strain and stress components over the thickness allows collapsing the body into an infinitely thin shell. Thus thickness can be ignored in the position vectors.

$$\mathbf{X} = \mathbf{R} \ , \qquad \mathbf{x} = \mathbf{r} \ , \qquad \mathbf{r} = \mathbf{R} + \mathbf{v} \tag{2.1}$$

Using the notation of $(\ )_{,\alpha} = \frac{\partial(\ )}{\partial \alpha}$ and explicitly writing the base vectors of the coordinate system yields:

$$\mathbf{A}_\alpha = \mathbf{R}_{,\alpha} = \mathbf{X}_{,\alpha} \ , \qquad \mathbf{a}_\alpha = \mathbf{r}_{,\alpha} = \mathbf{A}_\alpha + \mathbf{v}_{,\alpha} \tag{2.2}$$

Considering the metrics of the reference and deformed configuration, the in-plane Green-Lagrange strain components read:

$$\epsilon_{\alpha\beta} = \frac{1}{2}(a_{\alpha\beta} - A_{\alpha\beta}) \qquad with \qquad a_{\alpha\beta} = \mathbf{a}_\alpha \cdot \mathbf{a}_\beta \qquad A_{\alpha\beta} = \mathbf{A}_\alpha \cdot \mathbf{A}_\beta \tag{2.3}$$

Corresponding to the membrane assumptions, all out of plane strain components are 0.

$$\epsilon_{3i} = 0 \tag{2.4}$$

At this point, one notices that all strain terms are completely contained within the two in-plane mid-surface displacements $\mathbf{v}_\alpha$.

By introducing the elasticity tensor $\mathbf{C}_0$ (typically plane stress) the stress components can be recovered from the strains.

$$\sigma^{\alpha\beta} = C_0^{\alpha\beta\gamma\delta}\epsilon_{\gamma\delta} \tag{2.5}$$

With stresses and strains determined, the internal and a generalised (where $\mathbf{f}$ is a generalised traction vector and $\delta\mathbf{v}$ are virtual displacements) external virtual work can be expressed:

$$-\delta\Pi_{int} = \int_\Omega \boldsymbol{\epsilon} : \mathbf{C}_{mem} : \delta\boldsymbol{\epsilon}\, d\Omega\,, \qquad \delta\Pi_{ext} = \int_\Omega \mathbf{f}^T \delta\mathbf{v}\, d\Omega \tag{2.6}$$

It's apparent that the internal work is composed solely of in-plane action, corresponding to the general descriptive assumptions of the membrane model above. By extension, it can be understood that the membrane model provides no resistance to out of plane action. Thus, unless the membrane-modelled structure is pre-stressed, the system will be rendered singular under out of plane loads. This lack of out of plane stiffness can also lead to buckling under compressive stresses. Considering the reduced phenomena that the membrane model can resolve, it is crucial to understand the critical physics of the system before employing it.

2.2.2. 3 parameter model: Kirchhoff-Love shell

The first actual shell model considered is the 3 parameter model, often referred to as the Kirchhoff-Love (KL) shell. This model includes all membrane considerations, but also describes bending behaviour too. The bending behaviour is constrained to a description similar to the Bernoulli beam: shell directors across the thickness are always straight and normal to the mid-surface. Graphically, this is represented in the following figure:

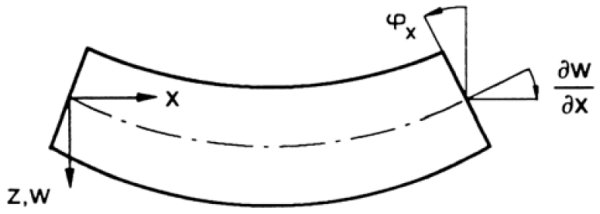

Figure 4 Kirchhoff-Love shell kinematics [11]

A consequence of the above kinematics is that this model ignores transverse shear strains. Thus, the applicability of the 3 parameter model is clearly limited to thin plates in the range of $\frac{1}{5} < \frac{l}{t} < \frac{1}{50}$ where transverse deformations are negligible. Similar to the membrane model, thickness deformation is ignored.

Establishing the geometry of the KL shell requires incorporation of the shell director along θ^3 in the reference $\mathbf{D}$ and deformed configuration $\mathbf{d}$.

$$\mathbf{X} = \mathbf{R} + \theta^3 \mathbf{D} \ , \qquad \mathbf{x} = \mathbf{r} + \theta^3 \mathbf{d} \ , \qquad \mathbf{r} = \mathbf{R} + \mathbf{v} \ , \qquad \mathbf{d} = \mathbf{\Lambda D} \tag{2.7}$$

The above equation enforces the KL condition of a straight director with the linear description of $\theta^3 \mathbf{d}$. $\mathbf{\Lambda}$ is a rotation tensor composed of two independent rotation parameters β^α relating the reference and deformed directors to each other. In a Cartesian frame the linearised rotation components are: $\beta^1 = \mathbf{v}_{3,2}$ and $\beta^2 = -\mathbf{v}_{3,1}$ [8].

The displacement is thus expressed:

$$\mathbf{u} = \mathbf{x} - \mathbf{X} = \mathbf{v} + \theta^3 (\mathbf{\Lambda} - \mathbf{G}) \mathbf{D} = \mathbf{v} + \theta^3 \mathbf{d} \tag{2.8}$$

!!!!!!!!!!!!!!!!!!!!!!!!!!!! Gotta figure out lamda - G = lamda !!!!!!!!!!!!!!!!!!!!!!!!!!!!

The KT requirement of the director being normal to the mid surface is expressed via the following dot product:

$$\mathbf{d} \cdot \mathbf{r}_{,\alpha} = (\mathbf{\Lambda D}) \cdot (\mathbf{A}_\alpha + \mathbf{v}_{,\alpha}) = 0 \tag{2.9}$$

Explicitly writing the base vectors of the coordinate system:

$$\mathbf{A}_\alpha = \mathbf{R}_{,\alpha} \qquad \mathbf{a}_\alpha = \mathbf{r}_{,\alpha} = \mathbf{A}_\alpha + \mathbf{v}_{,\alpha} \tag{2.10}$$

Eqn (2.9), requiring the director to be normal to the mid-surface, is guaranteed by employing cross products of the base vectors to construct the directors:

$$\mathbf{D} = \frac{\mathbf{A}_1 \times \mathbf{A}_2}{||\mathbf{A}_1 \times \mathbf{A}_2||} = \mathbf{A}_3 \ , \qquad \mathbf{d} = \frac{\mathbf{a}_1 \times \mathbf{a}_2}{||\mathbf{a}_1 \times \mathbf{a}_2||} = \mathbf{a}_3 \ , \tag{2.11}$$

As the KT model considers bending, which is related to curvature, the second fundamental form of the system is defined in the reference and deformed configuration:

$$B_{\alpha\beta} = \frac{1}{2} (\mathbf{A}_\alpha \cdot \mathbf{A}_{3,\beta} + \mathbf{A}_\beta \cdot \mathbf{A}_{3,\alpha}) = \mathbf{A}_\alpha \cdot \mathbf{A}_{3,\beta} = \mathbf{A}_\alpha \cdot \mathbf{D}_{,\beta} \tag{2.12}$$

$$b_{\alpha\beta} = \frac{1}{2}(\mathbf{a}_\alpha \cdot \mathbf{a}_{3,\beta} + \mathbf{a}_\beta \cdot \mathbf{a}_{3,\alpha}) = \mathbf{a}_\alpha \cdot \mathbf{a}_{3,\beta} = (\mathbf{A}_\alpha + \mathbf{v}_{,\alpha}) \cdot \left(\frac{(\mathbf{A}_1 + \mathbf{v}_{,1}) \times (\mathbf{A}_2 + \mathbf{v}_{,2})}{||(\mathbf{A}_1 + \mathbf{v}_{,1}) \times (\mathbf{A}_2 + \mathbf{v}_{,2})||} \right)_{,\beta} \tag{2.13}$$

Contrasting to the membrane model, the KT strain tensor components now include linearly varying terms corresponding to bending phenomena:

$$E_{\alpha\beta} = \frac{1}{2}(a_{\alpha\beta} - A_{\alpha\beta}) + \theta^3(b_{\alpha\beta} - B_{\alpha\beta}) = \epsilon_{\alpha\beta} + \theta^3 \kappa_{\alpha\beta} \tag{2.14}$$

According to the KT assumptions all out of plane strains are zero.

$$E_{3i} = \epsilon_{3i} = \kappa_{3i} = 0 \tag{2.15}$$

Studying the strain components, especially the deformed second fundamental form, reveals that there are now 3 midplane displacements $\mathbf{v}_i$ involved in the description of the KT shell model, hence the name 3 parameter model.

Combining the above developments, and assuming the same general external work as equation (2.6), the internal virtual work can be presented:

$$-\delta\Pi_{int} = \int_\Omega \boldsymbol{\epsilon} : \mathbf{C}_{mem} : \delta\boldsymbol{\epsilon} \; d\Omega + \int_\Omega \boldsymbol{\kappa} : \mathbf{C}_{bend} : \delta\boldsymbol{\kappa} \; d\Omega \tag{2.16}$$

The internal work equation illustrates the 3 parameter model considers in-plane membrane behaviour as well as the additional bending behaviour related to the second integral. Furthermore, under the condition of homogeneous linear material models the membrane and bending behaviour of the model are uncoupled. Due to the kinematics of the 3 parameter model (director remains straight and normal, no transverse shear strains), it can correctly resolve analyses as the thickness tends towards zero. This is in contrast the to 5 parameter model, which exhibits significant shear locking. Despite this, a pure rendition of the 3 parameter model is not commonly seen in practical FEM due to the required C_1 continuity at element boundaries (arising from rotations expressed as derivatives of transverse displacement) and the additional complication of effective shear forces on boundaries [8].

2.2.3. 5 parameter model: Reissner-Mindlin shell

By relaxing the assumptions made in the 3 parameter shell model, the Reissner-Mindlin (RM) 5 parameter shell model can be derived. This model includes both membrane and bending

action. While the KL model required that the shell directors remain normal to the mid-surface, the RM model relaxes this, analogous to the relationship between Bernoulli and Timoshenko beam models. Graphically, this is represented in the following figure:

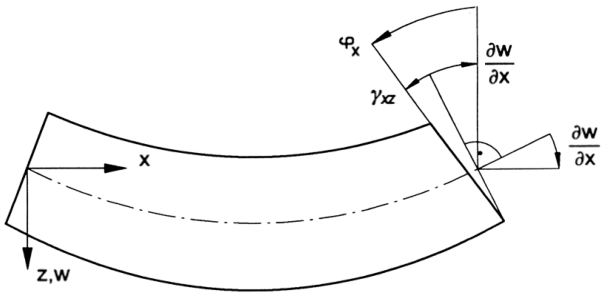

Figure 5 Reissner-Mindlin shell kinematics [11]

Studying the above kinematics confirms this model now considers transverse shear strains, limiting the range of validity of this model to thick plates $\frac{1}{5} < \frac{l}{t} < \frac{1}{10}$ where transverse deformations are a key component of structural behaviour. Similar to the membrane and KL model, thickness deformation is ignored.

The geometry of the RM model is established similar to the KL model:

$$\mathbf{u} = \mathbf{x} - \mathbf{X} = \mathbf{v} + \theta^3(\mathbf{\Lambda} - \mathbf{G})\mathbf{D} = \mathbf{v} + \theta^3\mathbf{d} \tag{2.17}$$

However, the strict requirement of maintaining the director remain normal to the mid-surface, as expressed in the KL theory equation (2.9), is no longer enforced. Correspondingly, the rotation tensor $\mathbf{\Lambda}$ must now include 2 additional parameters related to these 2 introduced degrees of freedom.

The general strain components are expressed as:

$$E_{\alpha\beta} = \frac{1}{2}(a_{\alpha\beta} - A_{\alpha\beta}) + \theta^3(b_{\alpha\beta} - B_{\alpha\beta}) = \epsilon_{\alpha\beta} + \theta^3\kappa_{\alpha\beta} \tag{2.18}$$

Once again it is noted the assumption of straight directors is enforced by the linear coupling of $\theta^3\kappa_{\alpha\beta}$. Following the assumption of no thickness strain, it is seen:

$$E_{33} = \epsilon_{33} = \kappa_{33} = 0 \tag{2.19}$$

By relaxing the director normality requirements, additional transverse shear strains must be

accounted for:

$$E_{\alpha 3} = E_{3\alpha} = \frac{1}{2}(a_{\alpha 3} - A_{\alpha 3}) = \frac{1}{2}\gamma_{3\alpha} \tag{2.20}$$

The internal virtual work is therefore expressed as:

$$-\delta\Pi_{int} = \int_{\Omega} \boldsymbol{\epsilon} : \mathbf{C}_{mem} : \delta\boldsymbol{\epsilon}\ d\Omega + \int_{\Omega} \boldsymbol{\kappa} : \mathbf{C}_{bend} : \delta\boldsymbol{\kappa}\ d\Omega + \int_{\Omega} \boldsymbol{\gamma} : \mathbf{C}_{shear} : \delta\boldsymbol{\gamma}\ d\Omega \tag{2.21}$$

The 3 integrals of the virtual work equation represent the membrane, bending and shear work components, corresponding to the phenomena this model resolves. Furthermore, all these components are decoupled from each other in flat shells with homogeneous linear material models. The consideration of transverse shear deformations in the kinematics render the model applicable to thick shells where these strains are not insignificant. Incorrectly applying this model to thin shells in FEM yields spurious results due to a phenomena called shear locking (discussed in section 2.3.1). Despite this disadvantage, the 5 parameter forms the basis of many shell elements often used in FEM thanks to the lower C_0 continuity required at element boundaries.

2.2.4. 7 parameter model

The previously discussed models all operate under the assumption that the transverse normal strains are zero. The 7 parameter model considers thickness deformation by introducing additional free parameters. Only a brief overview of the 7 parameter model is offered here as shell elements in FEM, the focus of this work, are predominately based off 3 and 5 parameter based formulations. For further details refer Bischoff et al. [8] and Ramm and Wall [36].

Intuitively, one may realise that shell behaviour including thickness change may be described by 6 parameters: 3 mid-surface displacements, 1 thickness change and 2 rotations. However, thickness locking occurs under this regime due to a mismatch of a linearly varying normal thickness stress θ^{33} conjugated with a constant thickness strain ϵ_{33}. Thus the 7th parameter is the enhancement of the through thickness strain ϵ_{33} to a linear field.

It's clear that the additional modelling power of the 7 parameter shell can resolve physics that lower parameter models can't. A prime example of this is the Eigenvalue spectra presented below:

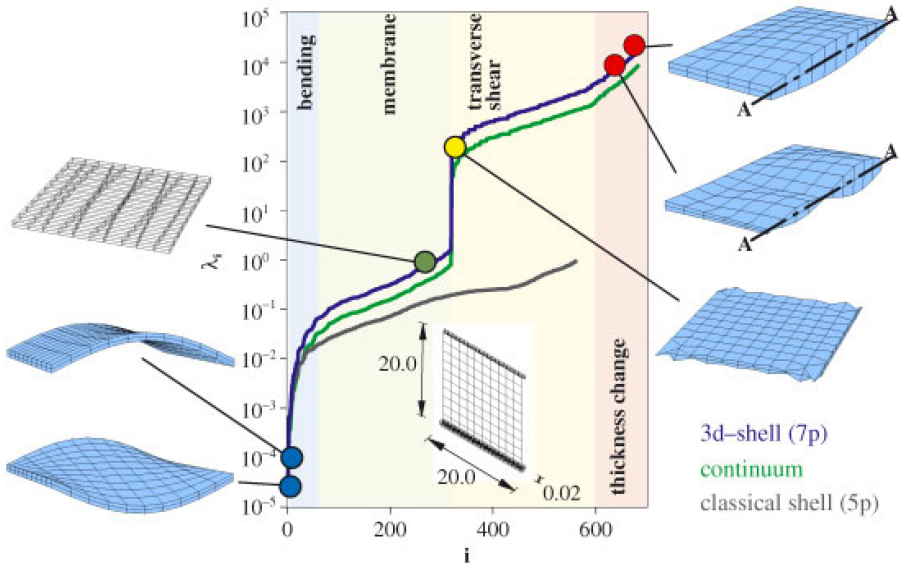

Figure 6 Eigenvalue spectra of various shell models [36]

As expected, the 7 parameter model captures higher Eigen-frequencies associated with thickness modes, while the 5 parameter is unable to resolve these. This is yet another example of model selection limiting the possibility of phenomena resolved.

2.3. Locking in shell finite elements

Surveying a range of shell models has confirmed that not all of them are appropriate for every type of analysis. One must consider the capabilities of the model in conjunction with the supposed critical phenomena of the analysis at hand. Thus, the analysis results are a function of physics the shell model can *express*. This concept of expression limitation is vital to the correct understanding of shells in the FEM. If the isogeometric approach to the FEM is employed, the field of quantities in the problem are interpolated between discrete nodal values $\hat{(\,)}$ using shape functions $\mathbf{N}$. In general:

$$\begin{pmatrix} \mathbf{R} \\ \mathbf{v} \\ \epsilon_{ij} \\ \vdots \end{pmatrix} (\xi,\eta) = \sum_{m=1}^{n\ nodes} N(\xi,\eta)_m \begin{pmatrix} \hat{\mathbf{R}}_m \\ \hat{\mathbf{v}}_m \\ \hat{\epsilon_{ij}}_m \\ \vdots \end{pmatrix} \tag{2.22}$$

The resolving power of the shape functions undoubtedly restricts what continuous fields can be described from discrete values. They govern not only the description of geometry, but also the deformation modes the element can express. This forms another layer of expression limitation

added to shell models in FEM. Given the propensity to use linear or quadratic shape functions in modern FEM codes, these limitations are often not insignificant. These, together with the physics assumptions and limitations of each shell model, give rise to common numerical inaccuracies, generally termed locking.

2.3.1. Transverse shear locking

Transverse shear locking is perhaps the most recognized and problematic locking phenomena amongst the three considered in this work. As it is related to transverse shear strains, transverse shear locking is possible in the 5 parameter model and impossible for membrane and 3 parameter models. Phenomenologically, transverse shear locking occurs when thin shells incorrectly described by a 5 parameter model are subject to bending situations, with the signature of significantly reduced displacements (ie. 'locked') than expected. By indicating specific material matrices, and removing membrane work for clarity, the internal bending and shear virtual work of the 5 parameter model can be expressed as follows:

$$\bar{\mathbf{C}} = \begin{pmatrix} 1 & \nu & 0 \\ \nu & 1 & 0 \\ 0 & 0 & \frac{1-\nu}{2} \end{pmatrix} \qquad \mathbf{C}_{bend} = \frac{Et^3}{12(1-\nu^2)}\bar{\mathbf{C}} \qquad \mathbf{C}_{shear} = \alpha G t \mathbf{I} \tag{2.23}$$

$$-(\delta\Pi_{int} - \delta\Pi_{int\ mem}) = -(\Pi_{bend} + \Pi_{shear}) = \int_\Omega \boldsymbol{\kappa} : \frac{Et^3}{12(1-\nu^2)}\bar{\mathbf{C}} : \delta\boldsymbol{\kappa}\, d\Omega + \int_\Omega \boldsymbol{\gamma} : \alpha G t \mathbf{I} : \delta\boldsymbol{\gamma}\, d\Omega \tag{2.24}$$

As phenomenologically described, transverse shear locking comes into effect with thin shells. One can see that as $t \to 0$ the bending internal work ($\Pi_{bend} \propto t^3$) will be far less than the shear internal work ($\Pi_{shear} \propto t$), leading to an incorrect allocation of internal energy. Since the bending internal work is associated with bending deflections, these resulting deflections will be less than they should be and the element will appear locked. The over-representation of shear strains also leads to strong shear force oscillations - another classic symptom of transverse shear locking.

2.3.2. Membrane locking

Membrane locking is the inability to undergo inextensional bending deformations without parasitic membrane contributions. Physically, a primary symptom of this is significantly reduced deformations under pure bending action. Element curvature is a necessary condition for membrane locking, while increasing slenderness exacerbates the problem. Similar to transverse shear locking, as $t \to 0$ the bending internal work ($\Pi_{bend} \propto t^3$) reduces at a far greater rate than the membrane internal work ($\Pi_{mem} \propto t$) leading to artificial membrane contributions. Thus, membrane locking is possible in 3, 5, and 7 parameter models. The following figure

illustrates the increasing severity of membrane locking as slenderness increases for 3 and 5 parameter NURBS based shell models.

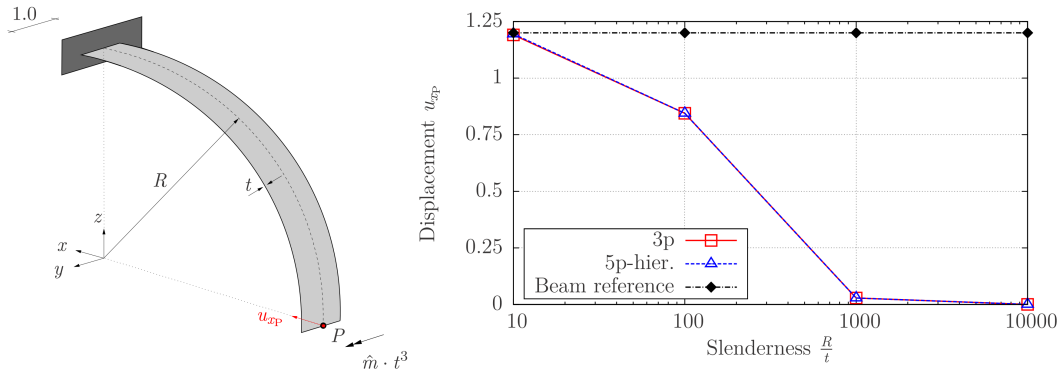

Figure 7 Convergence of cylindrical shell problem demonstrating membrane locking [16]

Despite the bleak results of the above problem, especially in high slenderness range, Bischoff et al. [8] suggest that the adverse effects of membrane locking are mild when using bilinear shape functions, and completely ignored in linear triangle elements (where curvature is always zero). These lower order finite elements form the bulk of what used in commercial FEM codes and are the focus of this work.

2.3.3. Curvature thickness locking

Curvature locking is another locking consideration that only occurs in curved structures with 7 parameter models. The hallmark of curvature thickness locking is artificial through-thickness strains ϵ_{33} under pure bending action. Since the focus of this work is 3 and 5 parameter models that don't include normal strains ϵ_{33}, the reader is referred to Bischoff et al. [8] and Echter [16] for further information.

2.4. Shell finite element technologies

The previous discussion of locking phenomena associated with pure displacement formulations of shell finite elements has given rise to a number of shell finite element technologies to improve element performance. Broadly speaking, these mitigation approaches fall into two categories: reduced integration and B-Bar ($\bar{\mathbf{B}}$) approaches which modify the strain displacement matrix $\mathbf{B}$.

2.4.1. Reduced integration

One of the simplest and oldest methods of curbing locking is reduced integration, which deliberately uses less Gauss points than required to integrate the element stiffness matrix. Typically implemented as selective reduced integration (SRI), where the bending component is fully integrated and only the shear part undergoes reduced integration, the efficacy of the

method relies on how susceptible the reduced integration Gauss point locations are to parasitic strains. Despite this 'chance' aspect, it is often used in crash worthiness simulations with the benefits of reduced locking and reduced computational time. The following graph compares the performance (scaled displacement vs. slenderness) of a fully and reduced integrated 5 parameter shell against the reference solution for a square plate in bending.

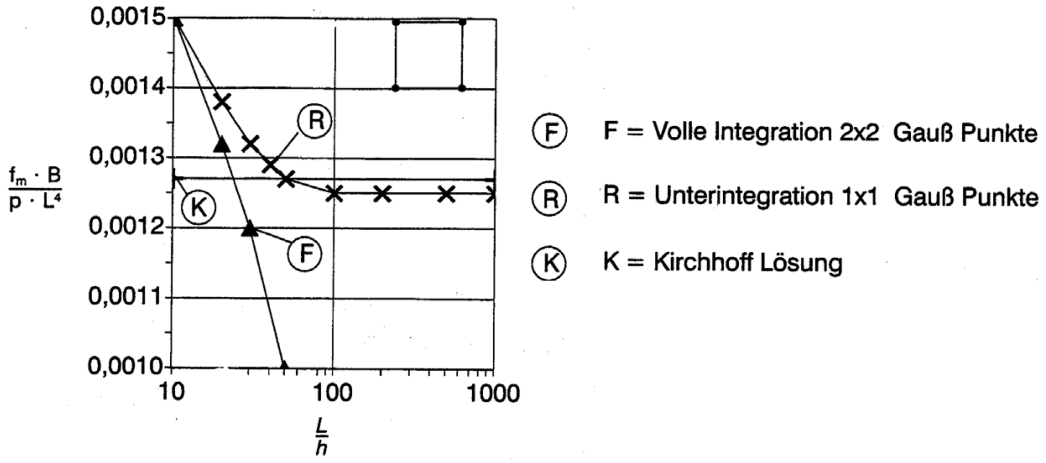

Figure 8 Reduced integration of a 5 parameter Quad 4 shell [11]

F = Full integration, R = Reduced integration, K = Kirchhoff (3 parameter model) solution

It's clear that the normal fully integrated element exhibits severe locking, while the element with reduced integration converges to a value close to the reference solution. Despite this, SRI in general still doesn't guarantee complete removal of shear locking and also introduces spurious zero energy modes. These zero energy modes are often combated by stabilizing matrices ("hourglass" control [43]) which are designed to be activated under the spurious zero-energy regimes and noted as quite complex to formulate [29]. An additional drawback of reduced integration is element performance deterioration as the mesh becomes distorted and warped [33] [42].

2.4.2. Assumed Natural Strains

The Assumed Natural Strain (ANS) approach forms a main umbrella of B-Bar methods, which alters the strain-displacement matrix $\mathbf{B}$ to mitigate locking. The ANS approach [27] works by computing the strain values at particular co-location points less susceptible to parasitic strains in the element (normally chosen as mid-edge and/or centre points) and then interpolating these discrete values through the element to define a new "assumed" shear strain field. As a general approach, many subsequent technologies fall under the ANS umbrella.

2.4.3. Mixed Interpolation of Tensorial Components

Falling within the ANS framework, Dvorkin and Bathe [15] [3] developed the Mixed Interpolation of Tensorial Components (MITC) approach which relies on an assumed shear strain field. A graphical example of this formulation is demonstrated below on a Quad 4 element, with linear interpolation of the shear strain field at mid-side points.

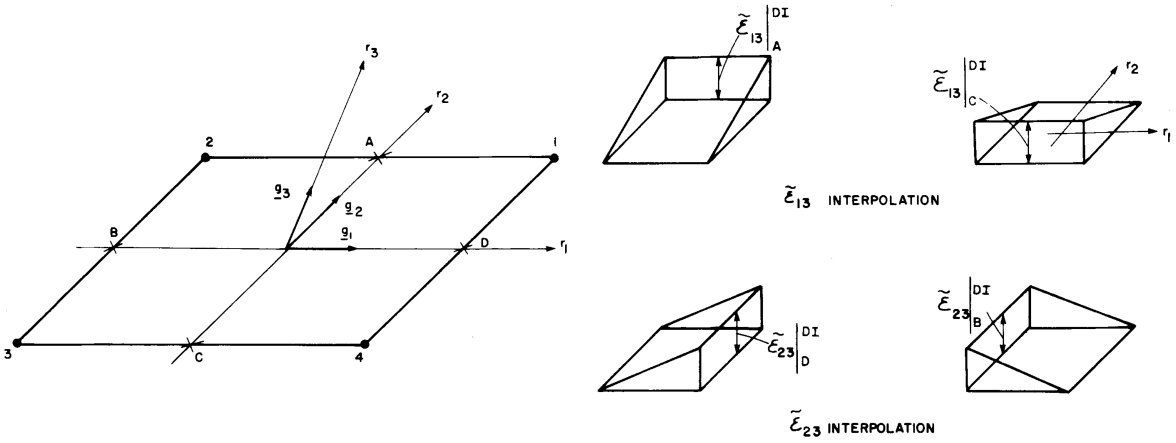

Figure 9 Assumed shear strain field of the MITC4 element [3]

The performance of the MITC formulation clearly depends on the location of the sampling points, and their susceptibility to parasitic shear strains under the case considered. Despite this, the MITC elements have proven resistant to membrane and transverse shear locking [3] and are amongst the most widely used elements throughout FEM codes.

2.4.4. Assumed Natural Deviatoric Strains

The ANS approach was extended into Free Formulation (FF) [7], where the element stiffness matrix is the sum of a basic and higher order stiffness, by Militello and Felippa [18] under the name of the Assumed Natural Deviatoric Strains (ANDES) formulation. An advantage that the ANDES formulation inherits from the FF is that it untethers the derivation of element stiffness from the principle of minimum potential energy, the function continuity requirements of which often result in elements that "tend to be too stiff" [7]. The ANDES basic stiffness ensures consistency of the element and arrises from the basic strain field comprising constant strain states and those associated with rigid body motion. Complementing this, the higher order stiffness is responsible for stability and accuracy [20] based on a enhanced strain field where the element enhancements are realised. The FF framework requires this potentially non-conforming higher order field be energy orthogonal to the basic field, which the ANDES formulation fulfils with a deviatoric higher order strain field [19]. The ANDES formulation has proven capable of alleviating membrane and transverse shear locking [30].

2.4.5. Discrete Shear Gap

The Discrete Shear Gap (DSG) approach from Bischoff and Bletzinger [12] [9] is another variant on the ANS approach with the novelty of identifying and manipulating the 'shear gap' field of the element. The shear gap, as illustrated below, is the increase of displacement due to shear, and corresponds to the difference between the actual displacement and that of pure bending (thus the shear gap is always zero in a 3 parameter Kirchhoff-Love model).

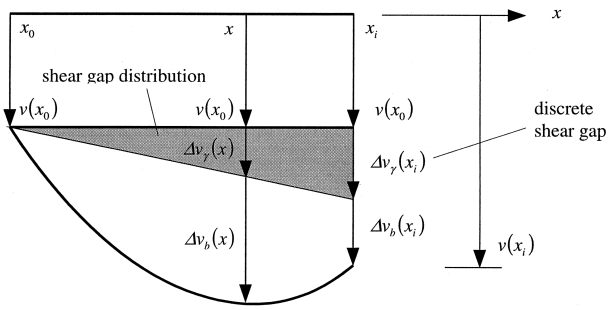

Figure 10 Discrete Shear Gap (DSG) concept [12]

The DSG method aims to set the nodal shear gaps to zero, which, in effect, alters and defines the underlying shear strain field. In bilinear rectangular applications of the DSG method, Bletzinger [12] notes that the MITC4 element is recovered. For a linear triangle element, the shear gap of only two nodes can be set to zero, rendering the element stiffness dependent on node ordering [12]. Despite this drawback, which diminishes with mesh refinement, the DSG method offers an advantage of very fast computational construction of element stiffness matrices and effective mitigation of transverse shear locking.

2.4.6. Discrete Kirchhoff Theory

Elements based on the Discrete Kirchhoff Theory (DKT) are obtained by modifying a basic 5 parameter element and ignoring the transverse shear energy [4]. Since the underlying kinematics of the 5 parameter model are different to Kirchhoff bending theory, the Kirchhoff constraints are enforced via discrete points (typically nodes and mid-edge points) along the element edges relating the rotations to translational displacements. The geometry and tying-points of the Discrete Kirchhoff Quadrilateral (DKQ) element are shown below:

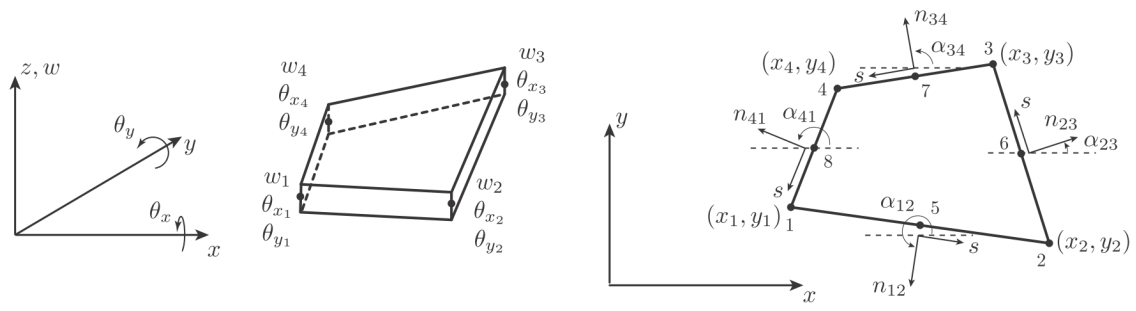

Figure 11 DKQ DOF arrangement and geometry [2]

For example, the Kirchhoff conditions are imposed at corner nodes $i = 1,2,3,4$ and mid-side nodes $k = 5,6,7,8$ [2]:

$$\beta_{xi} + \frac{\partial w}{\partial x}|_i = 0 \ , \qquad \beta_{yi} + \frac{\partial w}{\partial y}|_i = 0 \ , \qquad \beta_{sk} + \frac{\partial w}{\partial s}|_k = 0 \tag{2.25}$$

Mohan [29] noted that a major drawback of DKT elements is that the transverse displacement isn't explicitly defined within the interior of the element. Despite this, the advantages of DKT formulated elements is that they combine the shear locking free performance of KL models and the lower C_0 continuity requirements of RM models [11].

2.4.7. Enhanced Assumed Strains

The Enhanced Assumed Strain (EAS) approach [39] utilises the three field Hu-Washizu variational principle which allows the simultaneous variation of displacements, stresses and strains. Unlike the other technologies presented which attempt to remove problematic strain terms associated with locking, EAS derived elements feature additional enhanced strain fields designed to balance the parasitic displacement based strain terms. To prevent singular matrices the enhanced strains must be linearly independent from the displacement based strains. Furthermore, orthogonality of the stress functions to the enhanced strains must be ensured such that the associated energy vanish [16]. The application of EAS techniques to elements has been found to improve transverse shear and membrane locking performance [39] [8] [16].

2.4.8. Drilling degrees of freedom

Although drilling degrees of freedom (DOFs) don't counter locking problems, it is a commonly employed finite element technique. The common analysis of structural connections and custom steelwork are instances where shell elements will intersect with each other at arbitrary orientations. The discussion of 3 and 5 parameter shell models confirmed the nodal DOFs to be 3 translation and 2 rotational components:

$$\mathbf{v}_i^T = \begin{pmatrix} v_{xi} & v_{yi} & v_{zi} & \beta_{xi} & \beta_{yi} \end{pmatrix} \tag{2.26}$$

It can be seen that the shell formulations don't require a rotational DOF around the z axis β_{zi}, referred to as the drilling DOF. However, as discussed, shell elements in practical FEA may meet at arbitrary orientations, such as the perpendicular intersection below:

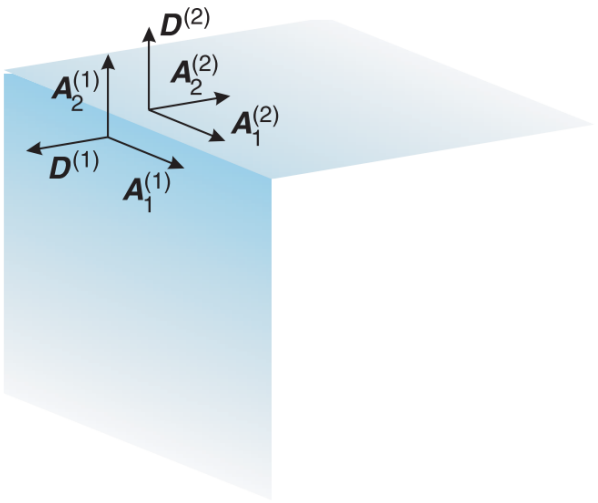

Figure 12 Shell assembly benefitting from drilling DOFs [8]

The figure above illustrates that the real twisting DOF associated with $A_2^{(2)}$ mates with the drilling DOF associated with $D^{(1)}$, which has no theoretically based stiffness value according to the shell formulations. In the current arrangement the connection will clearly be modelled too flexibly. A remedy for this is the addition of an artificial drilling DOF stiffness to the element, however the magnitude of such a fictitious torsional spring has no decisive theoretical foundation. Intuitively, it should be done on an element by element basis and should vary with the characteristic size and stiffness of the element, as opposed to a global constant drilling stiffness. Among others available, one common technique is to introduce a scaling factor (in the strain-displacement matrix or after the element stiffness matrix is constructed) which takes a fraction of the element stiffness and assigns it to the drilling DOFs.

2.4.9. Summary of selected element technologies

Following the discussion of shell models, their associated locking phenomena and element technologies, a summary of the element technologies considered with their relative merits and drawbacks is tabulated below:

Technology	Formulation	Advantages	Disadvantages
ANDES	5 parameter	Reduced membrane and transverse shear locking Relaxed higher order strain field	Locking reduction depends on tying points More complex implementation
ANS	5 parameter	Reduced membrane and transverse shear locking	Locking reduction depends on tying points
DKT	3 parameter	No transverse shear locking	Transverse disp. not explicitly defined
Drilling DOFs	-	Practical assembly of shells	Artificial stiffness
DSG	5 parameter	Reduced transverse shear locking Computationally fast	Node numbering dependency for linear triangle
EAS	5 parameter	Reduced transverse shear and membrane locking	Potentially complex implementation and possibly slower
MITC	5 parameter	Reduced membrane and transverse shear locking	Locking reduction depends on tying points
Reduced integration	-	Lowered computational cost Reduced locking	Zero energy modes Locking reduction depends on integration points

Table 1 Summary of selected element technologies

The table above confirms the *"no free lunch"* theory, with every technology having its own advantages and drawbacks. In the case of a flat shell (naturally, or via projection), where the bending and membrane response are decoupled, a single finite element can easily employ different technologies in each component.

2.5. Identification of Kratos shell element formulations

The shell elements to be implemented in Kratos are the 5 parameter (Reissner-Mindlin theory) triangular shell and the 3 parameter (Kirchhoff Love theory) quadrilateral shell. Obviously the perfect element choices for Kratos would be computationally quick, possess no locking and easy to implement, but it's clear such an element doesn't exist yet. If the requirements are relaxed to computationally quick elements that are relatively free of locking effects the following candidates are selected:

Element	Membrane formulation	Bending formulation
Thick triangular shell	DSG + Drilling DOFs	DSG
Thin quadrilateral shell	ANDES including Drilling DOFs	Discrete Kirchhoff Quadrilateral (DKQ)

Table 2 Selected formulations of implemented shell elements

With the various components of the KRATOS shell elements selected, they shall be implemented in the following sections of this work, commencing with the DSG triangle element.

Chapter 3 Composite shells

As is the case with shell structures, composite materials are widely encountered throughout nature and man-made structures. Truly isotropic materials are relatively rare to find in naturally occurring structures, with the phenotypical material usually being anisotropic due to varying demands in different directions. Intuitively, inspecting nature suggests that the best material for a structure subject to spatially non-uniform requirements will be non-uniform itself. This same approach has recently began to dominate the cutting edge of man-made engineering structures where specialized high-performance is demanded, leading to greater adoption of composite materials. The increasing proportion of composite materials in the aerospace industry is but one example of their increasing traction.

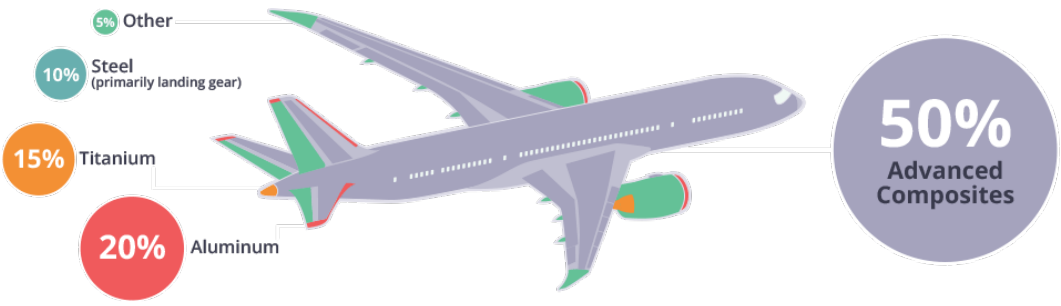

Figure 13 Material composition of the Boeing 787 [14]

The reason behind this increased propensity to use composites in high performance engineering applications is their customisability. Material properties such conductivity, density, wear resistance, and directional stiffness can be tailored to suit the exact needs of a design region. Directionally-varying stiffness is effectively leveraged in modern carbon-fiber road bicycles by simultaneously providing high stiffness for efficient power transfer and deliberate compliance for rider comfort and increased traction. This is one example of a composite material fulfilling seemingly mutually exclusive objectives due to finely tuned material properties built upon a knowledge of composite material basics.

3.1. Composite material basics

Composite materials are typically the combination of a high strength/stiffness fibre reinforcement material and a base matrix material which is usually weaker/softer than the fibres. Although a wide range composites exist, they are broadly grouped into fibrous composites (reinforcement material are fibres), particulate composites (reinforcement material are particles) and laminate composites composed of layers of different materials, including fibrous and particulate composites. Of these, this work focusses on laminates composed of fibrous composites which are commonly use in engineering.

3.1.1. Laminae and laminates

Laminae are individual layers or plies of composite materials, which, when stacked together, form a laminate. Each lamina consists of a volume percentage of reinforcement fibres embedded within the matrix material aligned at a particular orientation to a common coordinate system. Common fibre reinforcement materials are various glass fibres (including E-glass and S-glass), carbon/graphite fibres and boron fibres while common matrix materials are thermosetting polymers such as polyester and epoxy resins and metals including aluminium and titanium. The reinforcement fibres may be arranged in the lamina matrix in a variety of patterns and orientations, either continuous or discontinuous [1].

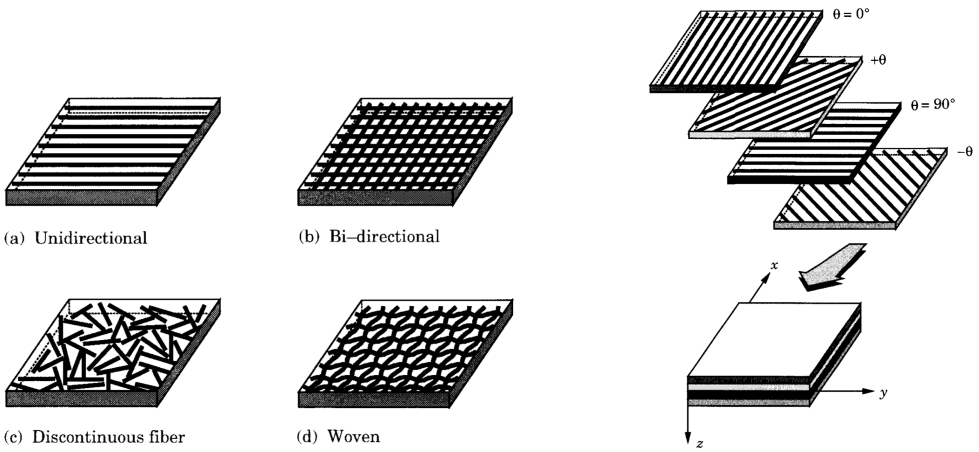

(a) Various composite laminae

(b) Composite laminate composed of laminae arranged in a stacking sequence

Figure 14 Components of composite laminates [38]

Considering the four laminae in figure 14 examples of anisotropy to varying degrees can be intuited. The unidirectional continuous fibre pattern is incredibly stiff and strong in the fibre direction while being relatively compliant and weak perpendicular to this fibre direction. Contrasting this, a practically in-plane isotropic lamina may be achieved with very fine discontinuous fibres randomly oriented within the matrix substrate. Thus, the importance of

individual lamina makeup forms a critical determinant of the structural behaviour of the total laminate as a whole. Another critical determinant of the laminate behaviour is the stacking sequence of the laminate, which prescribes the number of laminae, their vertical order and their orientation. The control that these two determinants offer designers facilitate highly optimized structures for well defined structural requirements. An industrial example of this is spoolable Glass Reinforced Epoxy (GRE) oil piping, which has a central structural lamina sandwiched between two non-structural Polyethylene (PE) laminae intended to provide the structural layer chemical and environmental protection. Furthermore, the alignment of the GRE structural lamina is often orientated at an optimal pressure-capacity angle since the stress field of the pipe operating under internal pressure is well defined.

3.1.2. Constitutive equations of orthotropic laminae

A pre-requisite of modelling complex laminates is the characterisation of each lamina. The general constitutive equations of laminae are thus established under the assumption of perfectly continuous linear elastic materials without fibre breakages or matrix voids. For a generally anisotropic material the stresses can be related to the strains as follows:

$$\sigma^{ij} = C_0^{ijkl}\epsilon_{kl} \tag{3.1}$$

Equivalently, adopting Reddy's [38] notation:

$$\begin{pmatrix} \sigma_{11} \\ \sigma_{22} \\ \sigma_{33} \\ \sigma_{23} \\ \sigma_{13} \\ \sigma_{12} \end{pmatrix} = \begin{pmatrix} C_{11} & C_{12} & C_{13} & C_{14} & C_{15} & C_{16} \\ & C_{22} & C_{23} & C_{24} & C_{25} & C_{26} \\ & & C_{33} & C_{34} & C_{35} & C_{36} \\ & & & C_{44} & C_{45} & C_{46} \\ & sym. & & & C_{55} & C_{56} \\ & & & & & C_{66} \end{pmatrix} \begin{pmatrix} \epsilon_{11} \\ \epsilon_{22} \\ \epsilon_{33} \\ 2\epsilon_{23} \\ 2\epsilon_{13} \\ 2\epsilon_{12} \end{pmatrix} \tag{3.2}$$

The preceding discussion of laminae illustrated there are innumerable design variants for any ply. In practise however, one of the most common lamina arrangements are orthotropic laminae. Orthotropic laminae have three mutually orthogonal planes of symmetry, which reduces the unique entries of the lamina-orientated constitutive tensor from 21 (anisotropic materials) to 9:

$$\begin{pmatrix} \sigma_{11} \\ \sigma_{22} \\ \sigma_{33} \\ \sigma_{23} \\ \sigma_{13} \\ \sigma_{12} \end{pmatrix} = \begin{pmatrix} C_{11} & C_{12} & C_{13} & 0 & 0 & 0 \\ & C_{22} & C_{23} & 0 & 0 & 0 \\ & & C_{33} & 0 & 0 & 0 \\ & & & C_{44} & 0 & 0 \\ & sym. & & & C_{55} & 0 \\ & & & & & C_{66} \end{pmatrix} \begin{pmatrix} \epsilon_{11} \\ \epsilon_{22} \\ \epsilon_{33} \\ 2\epsilon_{23} \\ 2\epsilon_{13} \\ 2\epsilon_{12} \end{pmatrix} \tag{3.3}$$

Furthermore, if the lamina is suitably thin, as is typically the case in composite shell structures, a plane state of stress can be assumed. This corresponds to $\sigma_{33} = 0$ as per the following illustration.

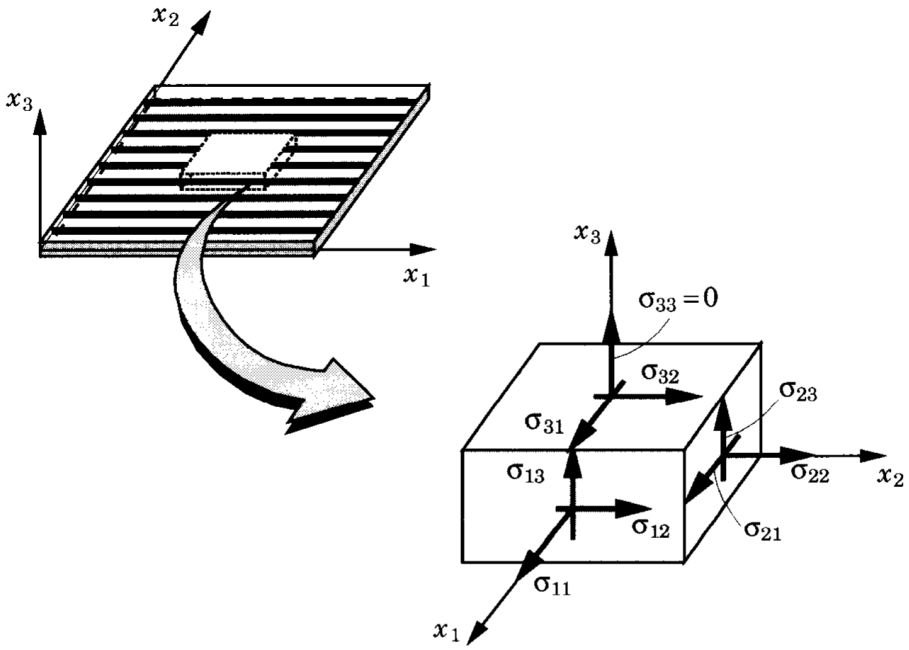

Figure 15 Lamina in a plane stress state [38]

The reduced plane stress orthotropic lamina constitutive tensor is therefore:

$$\begin{pmatrix} \sigma_{11} \\ \sigma_{22} \\ \sigma_{12} \\ \sigma_{23} \\ \sigma_{13} \end{pmatrix} = \begin{pmatrix} Q_{11} & Q_{12} & 0 & 0 & 0 \\ & Q_{22} & 0 & 0 & 0 \\ & & Q_{66} & 0 & 0 \\ & sym. & & Q_{44} & 0 \\ & & & & Q_{55} \end{pmatrix} \begin{pmatrix} \epsilon_{11} \\ \epsilon_{22} \\ 2\epsilon_{12} \\ 2\epsilon_{23} \\ 2\epsilon_{13} \end{pmatrix} \tag{3.4}$$

The entries Q_{ij} are derived from the bulk structural properties of the lamina at the macro-mechanical level. For example, the bulk lamina properties of a continuous fibre unidirectional design depicted in the following figure is considered.

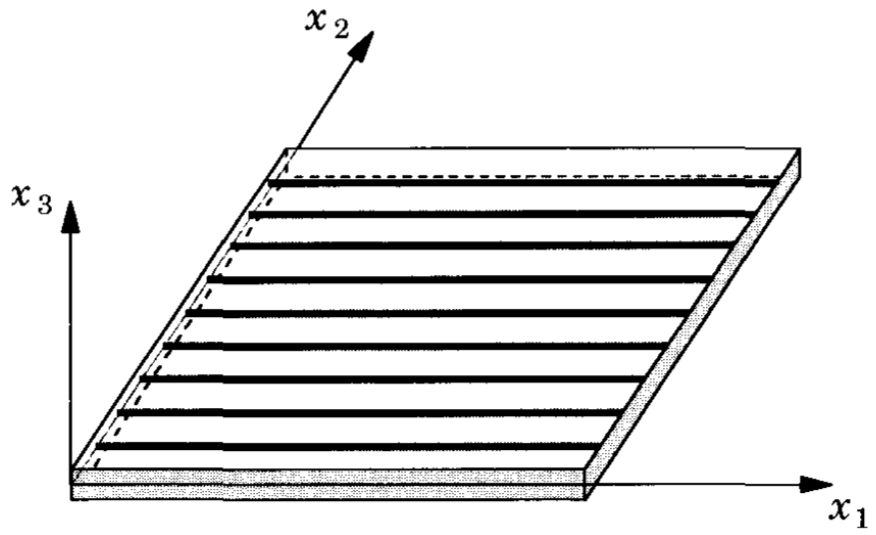

Figure 16 Continuous unidirectional fibre lamina arrangement [38]

If the Young's moduli and the Poisson ratios of both the individual fibre (E_f, ν_f) and matrix (E_m, ν_m) materials are known, along with the volume fraction of each (v_f, v_m), the resulting bulk lamina moduli can be determined.

Consider that the bulk modulus E_1, along x_1 and parallel to the fibres, is activated by tension σ_{11} along x_1. The constraint $\epsilon_{11_f} = \epsilon_{11_m} = \epsilon_{11}$ must be satisfied at every cross sectional area A along x_1. Thus:

$$\sigma_{11} = E_1 \epsilon_{11} \ , \qquad \sigma_{11_f} = E_f \epsilon_{11_f} \ , \qquad \sigma_{11_m} = E_m \epsilon_{11_m} \tag{3.5}$$

Applying force equilibrium:

$$\sigma_{11} A = \sigma_{11_f} A v_f + \sigma_{11_m} A v_m \tag{3.6}$$

Substituting and rearranging yields the longitudinal Young's modulus of the lamina:

$$E_1 = E_f v_f + E_m v_m \tag{3.7}$$

A similar line of analysis can be performed for the other lamina moduli, yielding the following results:

$$E_2 = \frac{E_f E_m}{E_f v_m + E_m v_f} \ , \qquad \nu_{12} = \nu_f v_f + \nu_m v_m \ , \qquad G_{12} = \frac{G_f G_m}{G_f v_m + G_m v_f} \tag{3.8}$$

The example of continuous unidirectional fibre laminae highlight that the material description of laminae can be shifted from a micro-mechanical level to a macro-mechanical level characterised by equivalent parameters. These are related to the entries Q_{ij} of the reduced plane stress orthotropic lamina constitutive tensor in equation 3.4 as follows:

$$Q_{11} = \frac{E_1}{1-\nu_{12}\nu_{21}} , \qquad Q_{12} = \frac{\nu_{12}E_1}{1-\nu_{12}\nu_{21}} , \qquad Q_{22} = \frac{E_2}{1-\nu_{12}\nu_{21}} \tag{3.9}$$

$$Q_{66} = G_{12} , \qquad Q_{44} = G_{23} , \qquad Q_{55} = G_{13} \tag{3.10}$$

The lamina macro-mechanical parameters $E_1,\ E_2,\ \nu_{12}, G_{12},\ G_{23}$ and G_{13} can be derived from the micro-mechanical properties of the lamina, as demonstrated, or, as is more common, are obtained experimentally. Regardless of their method of origin, these parameters are always aligned with the lamina local coordinate system, which may not necessarily coincide with the laminate coordinate system, or, more generally, the global reference coordinate system of the analysis.

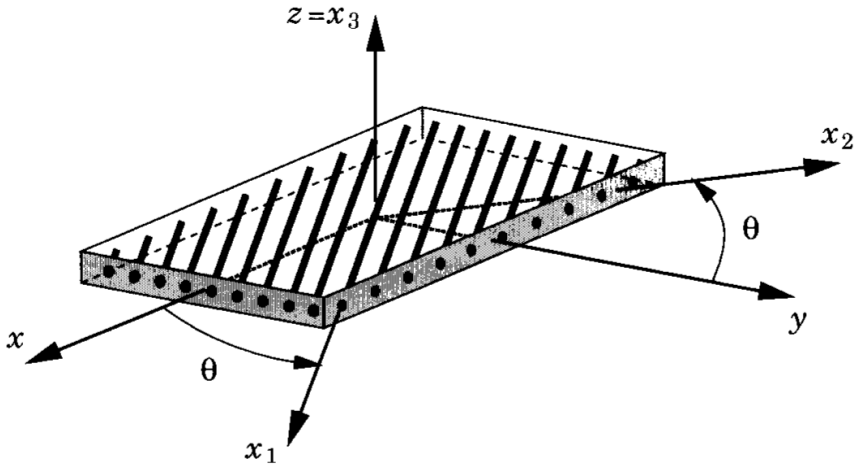

Figure 17 Arbitrary orientation of lamina [38]

The transformation of a locally oriented $(x_1,\ x_2,\ x_3)$ lamina constitutive tensor $\mathbf{Q}$ to one aligned with a reference coordinate system $(x,\ y,\ z)$ $\bar{\mathbf{Q}}$ through an angle θ about $\mathbf{z} = \mathbf{x_3}$ is achieved as follows ($c = cos\theta,\ s = sin\theta$):

$$\bar{\mathbf{Q}} = \mathbf{T}^T\mathbf{Q}\mathbf{T} , \qquad \mathbf{T} = \begin{pmatrix} c^2 & s^2 & -2sc & 0 & 0 \\ s^2 & c^2 & 2sc & 0 & 0 \\ sc & -sc & c^2-s^2 & 0 & 0 \\ 0 & 0 & 0 & c & s \\ 0 & 0 & 0 & -s & c \end{pmatrix} \tag{3.11}$$

Thus, stresses and strains in the reference coordinate system $(x,\ y,\ z)$ are related as such:

$$\begin{pmatrix} \sigma_{xx} \\ \sigma_{yy} \\ \sigma_{xy} \\ \sigma_{yz} \\ \sigma_{xz} \end{pmatrix} = \begin{pmatrix} \bar{Q}_{11} & \bar{Q}_{12} & \bar{Q}_{16} & 0 & 0 \\ & \bar{Q}_{22} & \bar{Q}_{26} & 0 & 0 \\ & & \bar{Q}_{66} & 0 & 0 \\ & sym. & & \bar{Q}_{44} & \bar{Q}_{45} \\ & & & & \bar{Q}_{55} \end{pmatrix} \begin{pmatrix} \epsilon_{xx} \\ \epsilon_{yy} \\ 2\epsilon_{xy} \\ 2\epsilon_{yz} \\ 2\epsilon_{xz} \end{pmatrix} \tag{3.12}$$

This transformation is required correctly assembly laminae in laminates that have non-zero stacking angles, which, by virtue of their customizability, is almost all laminates. With the individual
up and modelled.

3.2. Orthotropic shell laminates: internal virtual work

Orthotropic shell laminates are composites made from a stacking sequence of orthotropic laminae. As per their application in shells, the assumption of plane stress is continued.

The 5 parameter shell theory internal virtual work is recalled as:

$$-\delta\Pi_{int} = \int_{\Omega} \boldsymbol{\epsilon} : \mathbf{C}_{mem} : \delta\boldsymbol{\epsilon}\ d\Omega\ + \int_{\Omega} \boldsymbol{\kappa} : \mathbf{C}_{bend} : \delta\boldsymbol{\kappa}\ d\Omega\ + \int_{\Omega} \boldsymbol{\gamma} : \mathbf{C}_{shear} : \delta\boldsymbol{\gamma}\ d\Omega \tag{3.13}$$

The integral over the volume can split into area and laminate thickness integrals:

$$-\delta\Pi_{int} = \int_h \int_A \boldsymbol{\sigma}_{mem} : \delta\boldsymbol{\epsilon}\ dAdh\ + \int_h \int_A \boldsymbol{\sigma}_{bend} : \delta\boldsymbol{\kappa}\ \ dAdh\ + \int_h \int_A \boldsymbol{\tau} : \delta\boldsymbol{\gamma}\ \ dAdh \tag{3.14}$$

By pre-integrating the stress quantities, and restricting the scope of the equations to 2D plane stress conditions, the following equivalent form can be presented in vector notation:

$$-\delta\Pi_{int} = \int_A \mathbf{N}^T \delta\boldsymbol{\epsilon}\ dA\ + \int_A \mathbf{M}^T \delta\boldsymbol{\kappa}\ \ dA\ + \int_A \mathbf{Q}^T \delta\boldsymbol{\gamma}\ \ dA \tag{3.15}$$

The introduced quantities $\mathbf{N}$, $\mathbf{M}$ and $\mathbf{Q}$ are force and moment resultants over the entire laminate as per the following figure:

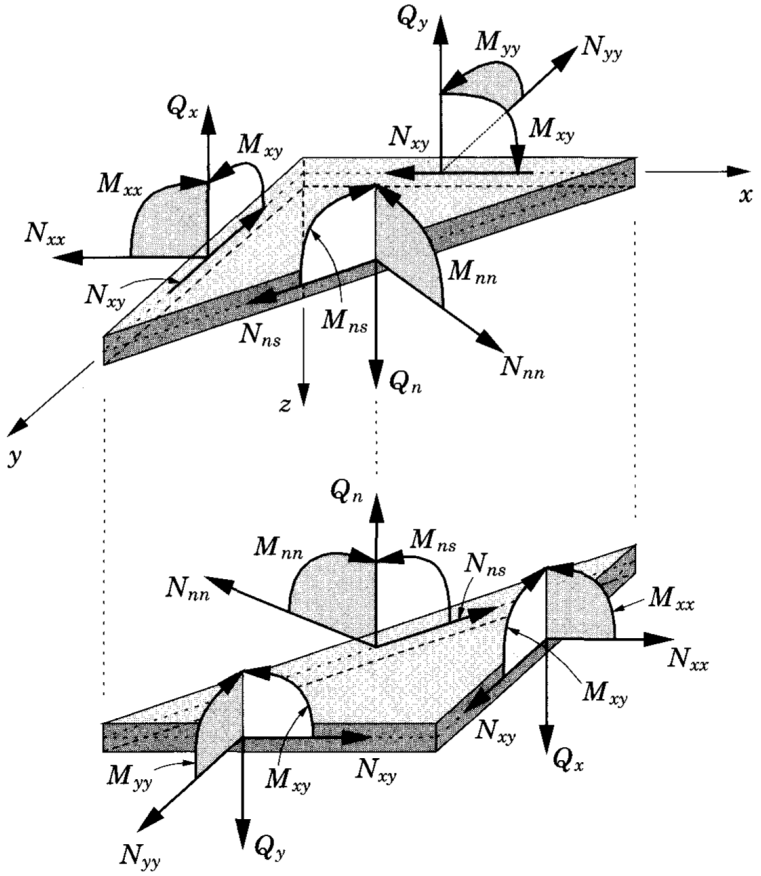

Figure 18 Force and moment resultants of a plate [38]

The force and moment resultants are defined as follows:

$$\mathbf{N} = \begin{pmatrix} N_{xx} \\ N_{yy} \\ N_{xy} \end{pmatrix} = \int_{\frac{-h}{2}}^{\frac{h}{2}} \begin{pmatrix} \sigma_{xx} \\ \sigma_{yy} \\ \sigma_{xy} \end{pmatrix} dz \ , \quad \mathbf{M} = \begin{pmatrix} M_{xx} \\ M_{yy} \\ M_{xy} \end{pmatrix} = \int_{\frac{-h}{2}}^{\frac{h}{2}} \begin{pmatrix} \sigma_{xx} \\ \sigma_{yy} \\ \sigma_{xy} \end{pmatrix} z \, dz \tag{3.16}$$

The shear resultants only applicable for the 5 parameter model are similarly defined, including a shear energy correction factor of $\alpha = \frac{5}{6}$:

$$\mathbf{Q} = \begin{pmatrix} Q_x \\ Q_y \end{pmatrix} = \alpha \int_{\frac{-h}{2}}^{\frac{h}{2}} \begin{pmatrix} \sigma_{xz} \\ \sigma_{yz} \end{pmatrix} dz \tag{3.17}$$

3.2.1. Laminate constitutive equations

At this point, the laminate force resultants, by way of the stress integrals, must be related back to strains across all laminae via laminate constitutive equations. A laminate of total thickness

h with n laminae is considered below:

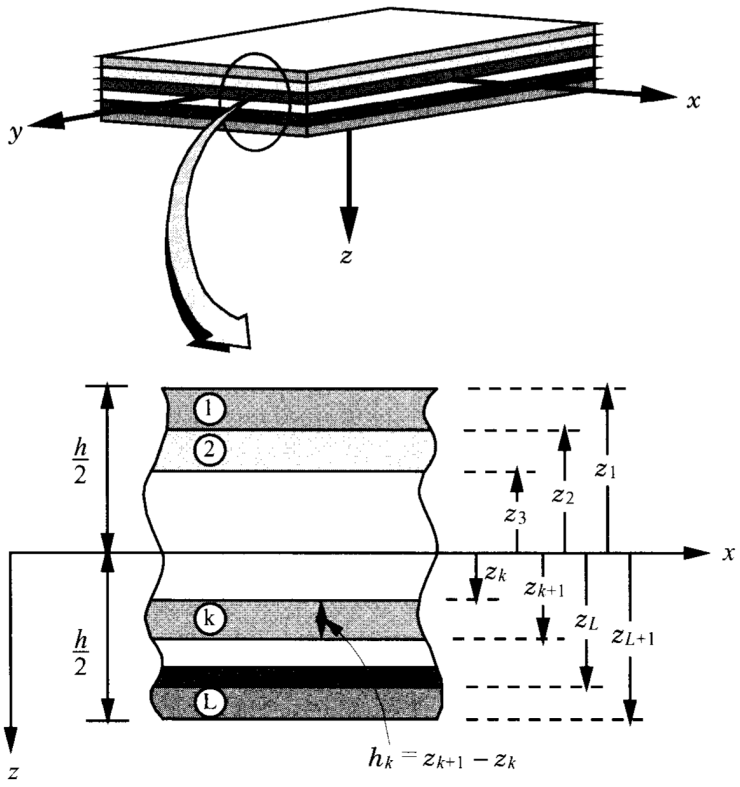

Figure 19 Coordinate system and lamina numbering in a laminate [38]

The force resultants can be determined as:

$$\mathbf{N} = \begin{pmatrix} N_{xx} \\ N_{yy} \\ N_{xy} \end{pmatrix} = \int_{\frac{-h}{2}}^{\frac{h}{2}} \begin{pmatrix} \sigma_{xx} \\ \sigma_{yy} \\ \sigma_{xy} \end{pmatrix} dz = \sum_{k=1}^{n} \int_{z_k}^{z_{k+1}} \begin{pmatrix} \sigma_{xx} \\ \sigma_{yy} \\ \sigma_{xy} \end{pmatrix} dz \tag{3.18}$$

Invoking the laminae constitutive properties previously established in equation 3.12 leads to the 'mathematical assemblage' of the laminae into the laminate via the following integral:

$$\begin{aligned} \begin{pmatrix} N_{xx} \\ N_{yy} \\ N_{xy} \end{pmatrix} &= \sum_{k=1}^{n} \int_{z_k}^{z_{k+1}} \begin{pmatrix} \bar{Q}_{11} & \bar{Q}_{12} & \bar{Q}_{16} \\ \bar{Q}_{12} & \bar{Q}_{22} & \bar{Q}_{26} \\ \bar{Q}_{16} & \bar{Q}_{26} & \bar{Q}_{66} \end{pmatrix}^{(k)} \begin{pmatrix} \epsilon_{xx} + z\kappa_{xx} \\ \epsilon_{yy} + z\kappa_{xx} \\ 2\epsilon_{xy} + 2z\kappa_{xy} \end{pmatrix} dz \\ &= \begin{pmatrix} A_{11} & A_{12} & A_{16} \\ A_{12} & A_{22} & A_{26} \\ A_{16} & A_{26} & A_{66} \end{pmatrix} \begin{pmatrix} \epsilon_{xx} \\ \epsilon_{yy} \\ 2\epsilon_{xy} \end{pmatrix} + \begin{pmatrix} B_{11} & B_{12} & B_{16} \\ B_{12} & B_{22} & B_{26} \\ B_{16} & B_{26} & B_{66} \end{pmatrix} \begin{pmatrix} \kappa_{xx} \\ \kappa_{xx} \\ 2\kappa_{xy} \end{pmatrix} \end{aligned} \tag{3.19}$$

Similarly, the moment and shear force resultants can be related to strains:

$$\begin{aligned}\begin{pmatrix} M_{xx} \\ M_{yy} \\ M_{xy} \end{pmatrix} &= \sum_{k=1}^{n} \int_{z_k}^{z_{k+1}} \begin{pmatrix} \bar{Q}_{11} & \bar{Q}_{12} & \bar{Q}_{16} \\ \bar{Q}_{12} & \bar{Q}_{22} & \bar{Q}_{26} \\ \bar{Q}_{16} & \bar{Q}_{26} & \bar{Q}_{66} \end{pmatrix}^{(k)} \begin{pmatrix} \epsilon_{xx} + z\kappa_{xx} \\ \epsilon_{yy} + z\kappa_{xx} \\ 2\epsilon_{xy} + 2z\kappa_{xy} \end{pmatrix} z \, dz \\ &= \begin{pmatrix} B_{11} & B_{12} & B_{16} \\ B_{12} & B_{22} & B_{26} \\ B_{16} & B_{26} & B_{66} \end{pmatrix} \begin{pmatrix} \epsilon_{xx} \\ \epsilon_{yy} \\ 2\epsilon_{xy} \end{pmatrix} + \begin{pmatrix} D_{11} & D_{12} & D_{16} \\ D_{12} & D_{22} & D_{26} \\ D_{16} & D_{26} & D_{66} \end{pmatrix} \begin{pmatrix} \kappa_{xx} \\ \kappa_{yy} \\ 2\kappa_{xy} \end{pmatrix}\end{aligned} \tag{3.20}$$

$$\begin{pmatrix} Q_x \\ Q_y \end{pmatrix} = \alpha \sum_{k=1}^{n} \int_{z_k}^{z_{k+1}} \begin{pmatrix} \bar{Q}_{44} & \bar{Q}_{45} \\ \bar{Q}_{45} & \bar{Q}_{55} \end{pmatrix}^{(k)} \begin{pmatrix} 2\epsilon_{yz} \\ 2\epsilon_{xz} \end{pmatrix} dz = \alpha \begin{pmatrix} A_{44} & A_{45} \\ A_{45} & A_{55} \end{pmatrix} \begin{pmatrix} 2\epsilon_{yz} \\ 2\epsilon_{xz} \end{pmatrix} \tag{3.21}$$

The three introduced matrices represent the extensional stiffnesses A_{ij}, the bending stiffnesses D_{ij} and the bending-extensional coupling stiffnesses B_{ij}, and are determined from the lamina stiffnesses $\bar{Q}_{ij}^{(k)}$:

$$A_{ij} = \int_{\frac{-h}{2}}^{\frac{h}{2}} \bar{Q}_{ij} \, dz \, , \quad B_{ij} = \int_{\frac{-h}{2}}^{\frac{h}{2}} \bar{Q}_{ij} z \, dz \, , \quad D_{ij} = \int_{\frac{-h}{2}}^{\frac{h}{2}} \bar{Q}_{ij} z^2 \, dz \tag{3.22}$$

By organising the resultants into a generalised resultant vector $\bar{\mathbf{N}}$ and the strains into a generalized strain vector $\bar{\boldsymbol{\epsilon}}$, the following summary is produced:

$$\bar{\mathbf{N}} = \bar{\mathbf{C}}\bar{\boldsymbol{\epsilon}} = \begin{pmatrix} N_{xx} \\ N_{yy} \\ N_{xy} \\ M_{xx} \\ M_{yy} \\ M_{xy} \\ Q_x \\ Q_y \end{pmatrix} = \begin{pmatrix} \mathbf{A} & \mathbf{B} & \mathbf{0} \\ \mathbf{B} & \mathbf{D} & \mathbf{0} \\ \mathbf{0} & \mathbf{0} & \alpha \begin{pmatrix} A_{44} & A_{45} \\ A_{45} & A_{55} \end{pmatrix} \end{pmatrix} \begin{pmatrix} \epsilon_{xx} \\ \epsilon_{yy} \\ 2\epsilon_{xy} \\ \kappa_{xx} \\ \kappa_{yy} \\ 2\kappa_{xy} \\ 2\epsilon_{yz} \\ 2\epsilon_{xz} \end{pmatrix} \tag{3.23}$$

The internal virtual work of the 5 parameter shell model presented in equation 3.15 can therefore be reduced down to:

$$-\delta\Pi_{int} = \int_A \bar{\mathbf{N}}^T \delta\bar{\boldsymbol{\epsilon}}\, dA \tag{3.24}$$

3.3. Laminate strain and stress recovery

Critical to the practical design of laminates is the evaluation of stresses and strains not only on the laminate mid-plane, but throughout the thickness across laminae. The following describes the procedure of recovering these quantities at arbitrary positions within the laminate thickness.

3.3.1. Laminate strain recovery

Owing to the dimensional reduction from 3D to 2D, the generalized shell strains $\bar{\epsilon}$ of equation 3.23 are referred to the mid-plane $(z = 0)$ of the laminate. Thus, within a local convective laminate coordinate system describing the z-axis orientation as per figure 19:

$$\bar{\boldsymbol{\epsilon}}(x,\, y) = \boldsymbol{\epsilon}(x,\, y,\, 0) \tag{3.25}$$

A consequence of the straight director assumption common to both the 3 and 5 parameter shell models is the membrane strains vary proportionally to the distance from the mid-plane. This can be observed in the following diagram of a plate in pure bending highlighting the linear variation of in-plane stresses (which, in simple cases, are merely scaled strains):

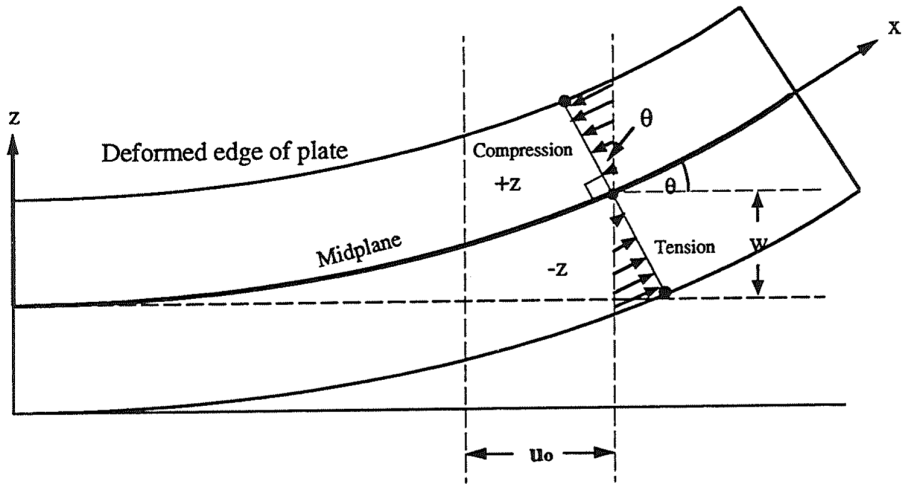

Figure 20 Deformation of 3 parameter plate [31]

Thus the in-plane strains at any position z in the laminate are determined from:

$$\begin{pmatrix} \epsilon_{xx} \\ \epsilon_{yy} \\ 2\epsilon_{xy} \end{pmatrix}_{(z)} = \begin{pmatrix} \epsilon_{xx} \\ \epsilon_{yy} \\ 2\epsilon_{xy} \end{pmatrix}_{(z=0)} + z \begin{pmatrix} \kappa_{xx} \\ \kappa_{yy} \\ 2\kappa_{xy} \end{pmatrix}_{(z=0)} \tag{3.26}$$

The in-plane strains of a surface in any lamina within the laminate can be determined by appropriately setting the corresponding z value.

Applicable only to 5 parameter shell models is the recovery of transverse shear strains. A perusal of Kreja's literature review on composite models [25] indicates the amount of academic effort dedicated to accurately modelling transverse shear strains in first order shear deformation theories. The contradiction driving this effort is that 5 parameter models are limited to expressing constant transverse shear strain over the shell thickness, while it is known that for an isotropic material they are actually distributed parabolically. This is the reason behind the shear correction factor of $\alpha = \frac{5}{6}$ which is actually the ratio of internal transverse shear strain energy in a 5 parameter plate to that of 3D elasticity. Without delving into exotic laminate shell theories, two options for recovering the transverse shear strain avail themselves: (1) accept the limitations of the 5 parameter model and consider the transverse shear strain constant across the section, or; (2) reconstruct a parabolic profile from the mid-plane values, as is often done for isotropic materials.

The first approach of accepting constant transverse shear stress is expressed as follows:

$$\begin{pmatrix} 2\epsilon_{yz} \\ 2\epsilon_{xz} \end{pmatrix}_{(z)} = \begin{pmatrix} 2\epsilon_{yz} \\ 2\epsilon_{xz} \end{pmatrix}_{(z=0)} \tag{3.27}$$

The second approach of constructing a parabolic strain profile using limiting expressions from [17] is described below, starting with the distribution of the transverse shear stress σ_{xz} in an isotropic plate:

$$\sigma_{xz}(z) = \sigma_{xz}^{max}(1 - \frac{4z^2}{h^2}) = \frac{3Q_x}{2h}(1 - \frac{4z^2}{h^2}) = \frac{3}{2}\sigma_{xz}^{av}(1 - \frac{4z^2}{h^2}) \tag{3.28}$$

Unlike laminate stresses, which are generally discontinuous across the thicknesss, laminate strains are continuous. Therefore, the strain distribution of the isotropic plate will be transferred to the laminate. The strain distribution of an isotropic plate must follow the stress distribution, thus:

$$\gamma_{xz}(z) = \frac{3}{2}\gamma_{xz}^{av}(1 - \frac{4z^2}{h^2}) = \frac{3}{2}2\epsilon_{xz}^{(z=0)}(1 - \frac{4z^2}{h^2}) \tag{3.29}$$

Summarising, the approximated transverse shear distribution for the laminate is:

$$\begin{pmatrix} 2\epsilon_{yz} \\ 2\epsilon_{xz} \end{pmatrix}_{(z)} = \frac{3}{2}(1 - \frac{4z^2}{h^2}) \begin{pmatrix} 2\epsilon_{yz} \\ 2\epsilon_{xz} \end{pmatrix}_{(z=0)} \tag{3.30}$$

The in-plane and transverse shear strains determined thus far are referred to the reference coordinate system of the laminate $(x,\ y,\ z)$. However, it is often of interest to transform these strains so they are aligned with the individual lamina considered $(x_1,\ y_1,\ z_1)$. For a lamina oriented at θ to the laminate coordinate system, the strain components can be transformed as such ($c = cos\theta,\ s = sin\theta$):

$$\begin{pmatrix} \epsilon_{11} \\ \epsilon_{22} \\ 2\epsilon_{12} \\ 2\epsilon_{23} \\ 2\epsilon_{13} \end{pmatrix} = \begin{pmatrix} c^2 & s^2 & sc & 0 & 0 \\ s^2 & c^2 & -sc & 0 & 0 \\ -sin2\theta & sin2\theta & c^2 - s^2 & 0 & 0 \\ 0 & 0 & 0 & c & -s \\ 0 & 0 & 0 & s & c \end{pmatrix} \begin{pmatrix} \epsilon_{xx} \\ \epsilon_{yy} \\ 2\epsilon_{xy} \\ 2\epsilon_{yz} \\ 2\epsilon_{xz} \end{pmatrix} \tag{3.31}$$

3.3.2. Laminate stress recovery

With the laminate strains across the thickness described, the stresses can be recovered by simply applying the considered lamina constitutive law as per equation 3.12. Naturally, the material coefficients Q_{ij} should correspond to the k^{th} lamina considered at the height of inspection z:

$$\begin{pmatrix} \sigma_{xx} \\ \sigma_{yy} \\ \sigma_{xy} \\ \sigma_{yz} \\ \sigma_{xz} \end{pmatrix}_{(z)} = \begin{pmatrix} \bar{Q}_{11} & \bar{Q}_{12} & \bar{Q}_{16} & 0 & 0 \\ & \bar{Q}_{22} & \bar{Q}_{26} & 0 & 0 \\ & & \bar{Q}_{66} & 0 & 0 \\ & sym. & & \bar{Q}_{44} & \bar{Q}_{45} \\ & & & & \bar{Q}_{55} \end{pmatrix}_{(k)} \begin{pmatrix} \epsilon_{xx} \\ \epsilon_{yy} \\ 2\epsilon_{xy} \\ 2\epsilon_{yz} \\ 2\epsilon_{xz} \end{pmatrix}_{(z)} \tag{3.32}$$

As previously hinted at, although the strain distribution is continuous across laminates, the stress distribution is generally discontinuous due to the varying material properties of the laminae. Indeed, if the laminae of a laminate are the exact same orthotropic composite material, but are stacked at varying angles, the resulting stress distribution will be discontinuous. The following example of a 4 ply laminate with a [0, 45, 45, 0] stacking sequence subject to pure bending highlights the nature of stress and strain distributions through the thickness despite all laminae being the same material.

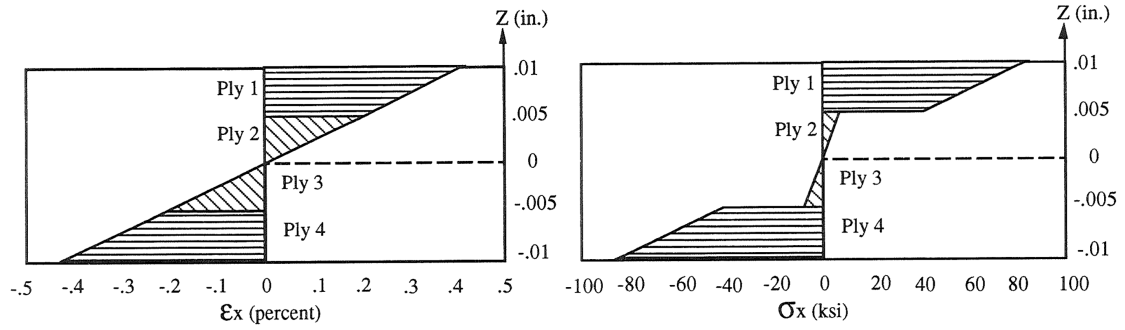

(a) Continuous strain distribution

(b) Discontinuous stress distribution

Figure 21 Stress and strain thickness distribution of 4 ply plate subject to pure bending [31]

Similar to the laminate strains, the in-plane and transverse shear stresses determined thus far are referred to the reference coordinate system of the laminate. For a lamina oriented at θ to the laminate coordinate system $(x,\ y,\ z)$, the stress components can be transformed to the lamina coordinate system $(x_1,\ y_1,\ z_1)$ as such ($c = cos\theta,\ s = sin\theta$):

$$\begin{pmatrix} \sigma_{11} \\ \sigma_{22} \\ 2\sigma_{12} \\ 2\sigma_{23} \\ 2\sigma_{13} \end{pmatrix} = \begin{pmatrix} c^2 & s^2 & sin2\theta & 0 & 0 \\ s^2 & c^2 & -sin2\theta & 0 & 0 \\ -sc & sc & c^2 - s^2 & 0 & 0 \\ 0 & 0 & 0 & c & -s \\ 0 & 0 & 0 & s & c \end{pmatrix} \begin{pmatrix} \sigma_{xx} \\ \sigma_{yy} \\ 2\sigma_{xy} \\ 2\sigma_{yz} \\ 2\sigma_{xz} \end{pmatrix} \tag{3.33}$$

3.4. Laminate Tsai-Wu failure criterion

The Tsai-Wu failure criterion is a relatively simple method to approximate the safety of composite materials under combined loading. As an extension of the Von Mises distortion energy theory, it provides an invariant scalar indication of how proximate the current stress state of a lamina is to breaching the closed convex failure surface [21]. The closed convex failure surface is defined by material strength parameters F_i and F_{ij}, with failure predicted by fulfilling the following inequality [38]:

$$\sum_{i=1}^{6} F_i\sigma_i + \sum_{i=1}^{6}\sum_{j=1}^{6} F_{ij}\sigma_{ij} \geq 1.0 \qquad with \qquad \begin{pmatrix}\sigma_1\\ \sigma_2\\ \sigma_3\\ \sigma_4\\ \sigma_5\\ \sigma_6\end{pmatrix} = \begin{pmatrix}\sigma_{11}\\ \sigma_{22}\\ \sigma_{33}\\ \sigma_{23}\\ \sigma_{13}\\ \sigma_{12}\end{pmatrix} \tag{3.34}$$

By considering the tensile $(X_T,\ Y_T,\ Z_T)$ and compressive $(X_C,\ Y_C,\ Z_C)$ strengths in the lamina principal material directions (1, 2, 3) and the shear strengths $(R,\ S,\ T)$ corresponding to (23, 13, 12), the non-zero material strength parameters in a plane stress regime are expressed as:

$$\begin{gathered} F_1 = \frac{1}{X_T} - \frac{1}{X_C}\ , \quad F_2 = \frac{1}{Y_T} - \frac{1}{Y_C}\ , \quad F_{11} = \frac{1}{X_T X_C}\ , \quad F_{22} = \frac{1}{Y_T Y_C} \\ F_{44} = \frac{1}{R^2}\ , \quad F_{55} = \frac{1}{S^2}\ , \quad F_{66} = \frac{1}{T^2}\ , \quad F_{12} = \frac{-0.5}{\sqrt{X_T X_C Y_T Y_C}} \end{gathered} \tag{3.35}$$

The strength parameter F_{12} is termed the in-plane interaction factor and is generally difficult to determine experimentally. Thus, it is often approximated from other more readily available strengths, as per equation 3.35 or set to zero entirely. Further information regarding F_{12} can be found in Reference [21]. In the scope of this work F_{12} is determined as per equation 3.35.

Although equation 3.34 describes the Tsai-Wu criterion, it does so in terms of a Failure Index (FI). That is, if the calculated FI is greater than 1.0, failure occurs. Contrasting this, engineers are often interested in safety factors, or more specifically, the ratio with which to increase loads to just achieve failure. This parameter is commonly referred to as either the Reserve Factor (RF) or Strength Ratio (SR), with values less than 1.0 indicating failure while those above 1.0 correspond to safety. The Tsai-Wu RF can be determined as follows [24]:

$$RF = \frac{-b + \sqrt{b^2 + 4a}}{2a} \quad with \quad a = \sum_{i=1}^{6}\sum_{j=1}^{6} F_{ij}\sigma_{ij}\ , \quad b = \sum_{i=1}^{6} F_i\sigma_i \tag{3.36}$$

Chapter 4 DSG triangle shell element

The follow exposition clarifies the stiffness matrix, mass matrix and quantity recovery of the DSG triangle shell element in Kratos.

4.1. Stiffness matrix formulation

Based on the 5 parameter Reissner-Mindlin shell theory, the thick shell considers internal energy contributions from membrane, bending and shear components. As discussed in Chapter 2, basic finite elements derived from this shell theory face locking problems as the shell slenderness ratio increases. The element implemented is Bletzinger's Discrete Shear Gap (DSG) shell [12] which incorporates an enhanced shear strain formulation to mitigate the aforementioned locking. This triangular element has 18 DOFs ordered as such:

$$\mathbf{u}^T = \begin{pmatrix} \mathbf{u_1} & \mathbf{u_2} & \mathbf{u_3} \end{pmatrix} \qquad where \qquad \mathbf{u}_i^T = \begin{pmatrix} u_{xi} & u_{yi} & u_{yi} & \beta_{xi} & \beta_{yi} & \beta_{zi} \end{pmatrix} \tag{4.1}$$

The element displacement field is related to the discrete nodal values via shape functions.

$$\mathbf{u}(x,y) = \sum_{i=1}^{3} N_i(x,y)\mathbf{u}_i \tag{4.2}$$

N_i are the standard linear triangle shape functions, referred to the cartesian system.

$$\begin{aligned} N_1(x,y) &= \frac{1}{2A}\left[(x_2y_3 - x_3y_2) + x(y_2 - y_3) + y(x_3 - x_2)\right] \\ N_2(x,y) &= \frac{1}{2A}\left[(x_3y_1 - x_1y_3) + x(y_3 - y_1) + y(x_1 - x_3)\right] \\ N_3(x,y) &= \frac{1}{2A}\left[(x_1y_2 - x_2y_1) + x(y_1 - y_2) + y(x_2 - x_1)\right] \end{aligned} \tag{4.3}$$

Analogous to internal energy, the element stiffness matrix of the DSG triangle can be decomposed into membrane, bending and shear contributions.

$$\mathbf{K} = \mathbf{K}_{mem} + \mathbf{K}_{bend} + \mathbf{K}_{shear} \tag{4.4}$$

The above expression can be expanded into strain-displacement and material matrices relevant for each component.

$$\mathbf{K} = \int_A (\mathbf{B}_{mem}^T \mathbf{C}_{mem} \mathbf{B}_{mem} + \mathbf{B}_{bend}^T \mathbf{C}_{bend} \mathbf{B}_{bend} + \mathbf{B}_{shear}^T \mathbf{C}_{shear} \mathbf{B}_{shear})\, dA \tag{4.5}$$

Rama et al. [35] present the DSG formulation in a similar manner, detailing the strain displacement matrix and material material of each constituent separately.

The membrane strain displacement matrix can be expressed as:

$$\mathbf{B}_{mem} = \begin{pmatrix} \mathbf{B}_{mem_1} & \mathbf{B}_{mem_2} & \mathbf{B}_{mem_3} \end{pmatrix} \tag{4.6}$$

$$\mathbf{B}_{mem_i} = \begin{pmatrix} N_{i,x} & 0 & 0 & 0 & 0 & 0 \\ 0 & N_{i,y} & 0 & 0 & 0 & 0 \\ N_{i,y} & N_{i,x} & 0 & 0 & 0 & 0 \end{pmatrix} \tag{4.7}$$

The bending strain displacement matrix can be presented in a similar manner:

$$\mathbf{B}_{bend} = \begin{pmatrix} \mathbf{B}_{bend_1} & \mathbf{B}_{bend_2} & \mathbf{B}_{bend_3} \end{pmatrix} \tag{4.8}$$

$$\mathbf{B}_{bend_i} = \begin{pmatrix} 0 & 0 & 0 & 0 & N_{i,x} & 0 \\ 0 & 0 & 0 & -N_{i,y} & 0 & 0 \\ 0 & 0 & 0 & -N_{i,x} & N_{i,y} & 0 \end{pmatrix} \tag{4.9}$$

Finally, the shear strain displacement matrix, which has the DSG element technology 'baked' into it, is as follows:

$$\mathbf{B}_{shear} = \frac{1}{2A}\begin{pmatrix} 0 & 0 & b-c & 0 & A & 0 & 0 & 0 & c & \frac{-bc}{2} & \frac{ac}{2} & 0 & 0 & 0 & -b & \frac{bc}{2} & \frac{bd}{2} & 0 \\ 0 & 0 & d-a & -A & 0 & 0 & 0 & 0 & -d & \frac{bd}{2} & \frac{-ad}{2} & 0 & 0 & 0 & a & \frac{-ac}{2} & \frac{ad}{2} & 0 \end{pmatrix}$$

$$with:\ a = x_2 - x_1,\ b = y_2 - y_1,\ c = y_3 - y_1,\ d = x_3 - x_1 \tag{4.10}$$

The material matrices for the membrane and bending parts are presented below:

$$\mathbf{C}_{mem} = \frac{Et}{(1-\nu^2)}\begin{pmatrix} 1 & \nu & 0 \\ \nu & 1 & 0 \\ 0 & 0 & \frac{(1-\nu)}{2} \end{pmatrix} \tag{4.11}$$

$$\mathbf{C}_{bend} = \frac{Et^3}{12(1-\nu^2)}\begin{pmatrix} 1 & \nu & 0 \\ \nu & 1 & 0 \\ 0 & 0 & \frac{(1-\nu)}{2} \end{pmatrix} \tag{4.12}$$

To further improve the DSG element performance, Bischoff and Bletzinger [9] [10] applied the enhancement approach that Lyly suggested for MITC-4 elements [26]. This approach modifies the internal shear energy term by scaling the shear constitutive matrix with a correction term τ incorporating the element thickness and an indicator of element size (h_k = longest element side length). The revised shear constitutive matrix is thus:

$$\mathbf{C}_{shear} = \tau\kappa G t \begin{pmatrix} 1 & \nu \\ \nu & 1 \end{pmatrix} = \frac{\kappa G t^3}{t^2 + \alpha h_k^2}\begin{pmatrix} 1 & \nu \\ \nu & 1 \end{pmatrix} \tag{4.13}$$

where $\kappa = \frac{5}{6}$ is the shear correction factor and $\alpha = 0.1$ as per [26].

As described in section 2.3.1, transverse shear locking is driven by a mismatch of internal energy allocation between bending ($\Pi_{bend} \propto t^3$) and shear components ($\Pi_{shear} \propto t$) as $t \to 0$. This modification somewhat alleviates the locking by 'encouraging' the internal shear energy to scale with the cube of the thickness too, thus reducing the artificial energy disparity.

Although all stiffness components are assembled, one notices that lack of entries corresponding to the drilling DOF β_{zi} currently renders the element stiffness matrix singular. The technology of drilling DOFs discussed in 2.4.8 in thus introduced. Nguyen-Thoi et al. [32]

proposed to remedy this rotational singularity by setting the drilling DOF entries to one one-thousandth of the maximum diagonal entry in the element stiffness matrix.

$$K_{\beta_z} = \frac{max(K_{ij}\delta_{ij})}{1000} \tag{4.14}$$

4.2. Stiffness matrix implementation

Despite the relatively simple and decoupled stiffness formulation presented, the practical programming of it invariably introduces it's own complexities. Furthermore, leveraging the existing functionality that the Kratos code possesses not only prevents re-inventing the wheel, but also makes the code more readable and functionally cohesive.

The new DSG triangle element is implemented in the files `shell_thick_element_3D3N.hpp` and `shell_thick_element_3D3N.cpp`, which are compiled into the 'StructuralMechanicsApplication' module of Kratos. Without extending into extraneous details, the DSG triangle element is derived from the Kratos `element` class and makes extensive use of other existing Kratos utility classes including those offering: coordinate transformations, material properties and response and pre-defined stiffness matrix and residual vector "containers". Correspondingly, it is also subject to the constraints associated with each of these. From a high level view, however, the element stiffness matrix follows the subsequent workflow:

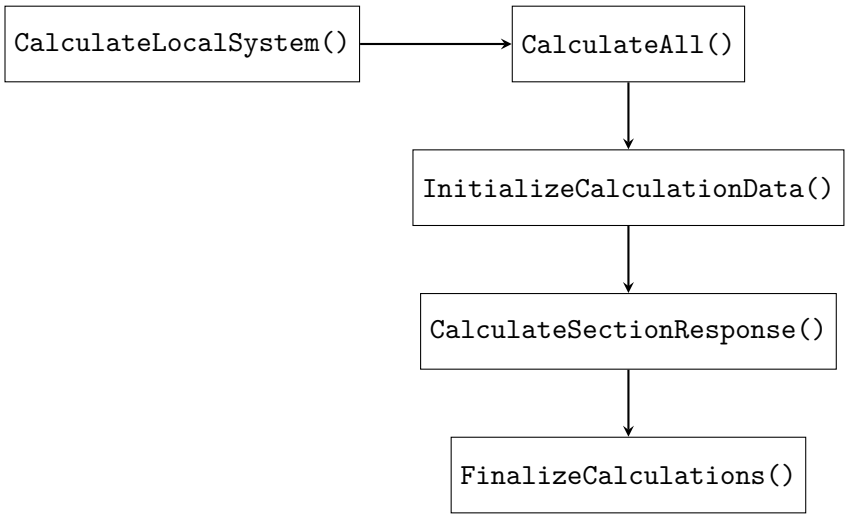

Figure 22 High level overview of DSG element workflow

Initially, the re-implemented virtual method `CalculateLocalSystem()` is called by the Kratos framework automatically for every `ShellThickElement3D3N` in the job definition. This method redirects to `CalculateAll()`, which is the main pipeline of the element stiffness calculation, itself calling three key methods: `InitializeCalculationData()`,

`CalculateSectionResponse()` and `FinalizeCalculations()`.

Following the general form of the existing shell elements in Kratos, all the data which remains constant through the Gauss Integration loop is calculated beforehand in the function `InitializeCalculationData()`. The DSG element follows this tradition for consistency, although it isn't strictly necessary because it only requires one Gauss point for the numerical integration. Following `InitializeCalculationData()`, `CalculateSectionResponse()` is called and the material matrix is populated with existing Kratos material classes. It must be noted here that a single 8×8 material matrix $\mathbf{C}$ is returned which is structured as follows (for the setting of 'thick' shell kinematics):

$$\mathbf{C}_{Kratos} = \begin{pmatrix} \mathbf{C}_{mem} & \mathbf{0} & \mathbf{0} \\ \mathbf{0} & \mathbf{C}_{bend} & \mathbf{0} \\ \mathbf{0} & \mathbf{0} & \mathbf{C}_{shear} \end{pmatrix} \tag{4.15}$$

At this stage the shear component of the material matrix is unmodified, and is corrected with τ as per equation (4.13). The DOF arrangement of the material matrix also motivates a slight departure from the strain displacement matrices as presented above. Although the element stiffness matrix can certainly be programmed in it's constitutive parts, as per equation (4.5), it is more concise to calculate it as follows:

$$\mathbf{K} = \int_A (\mathbf{B}_{comb}^T \mathbf{C}_{Kratos} \mathbf{B}_{comb})\, dA = A\, \mathbf{B}_{comb}^T \mathbf{C}_{Kratos} \mathbf{B}_{comb} \tag{4.16}$$

A consequence of this arrangement is that the combined strain displacement matrix created in `InitializeCalculationData()` must conform to the DOF ordering of the material matrix layout.

The element stiffness matrix is calculated according to equation (4.16) and subsequently modified to include an artificial drilling DOF stiffness as per equation (4.14). Lastly, this is followed by a call to the Kratos function `FinalizeCalculations()` which handles the transformation from the element to the global orientation.

The following pseudocode summarises the key calls and operations involved in calculating the DSG element stiffness matrix.

Algorithm 1 DSG triangle element stiffness matrix pseudocode

Require: Coordinate transformation instance

call `CalculateAll`()
Resize LHS and RHS
call `InitializeCalculationData`($data$)
    Calculate combined strain-displacement matrix B
call `CalculateSectionResponse`($data$)
    Retrieve material properties C
    Apply shear stabilization to material matrix C
Calculate LHS stiffness matrix
Add in artificial drilling stiffness
Modify RHS residual vector
call `FinalizeCalculations`($data$, $displacements$, LHS, RHS)
call `AddBodyForces`($data$, RHS)

4.3. Mass matrix formulation and implementation

The specification of a mass matrix is necessary to facilitate dynamic analysis with the thick triangular shell element. Both lumped and consistent mass matrices are offered, with the lumped mass matrix used by default.

4.3.1. Lumped mass matrix

The default mass matrix employed is a lumped approach, which results in a diagonal mass matrix that ignores rotary inertia.

$$\mathbf{M} = \begin{pmatrix} \mathbf{M}_1 & \mathbf{0} & \mathbf{0} \\ \mathbf{0} & \mathbf{M}_2 & \mathbf{0} \\ \mathbf{0} & \mathbf{0} & \mathbf{M}_3 \end{pmatrix} \qquad where \qquad \mathbf{M}_i = \begin{pmatrix} \bar{m} & 0 & 0 & 0 & 0 & 0 \\ 0 & \bar{m} & 0 & 0 & 0 & 0 \\ 0 & 0 & \bar{m} & 0 & 0 & 0 \\ 0 & 0 & 0 & 0 & 0 & 0 \\ 0 & 0 & 0 & 0 & 0 & 0 \\ 0 & 0 & 0 & 0 & 0 & 0 \end{pmatrix} \tag{4.17}$$

The general lumped mass is determined for a multi-ply material with n plies each of t_i thickness and ρ_i density as follows:

$$\bar{m} = \frac{A}{3} \sum_{i=1}^{n} \rho_i t_i \tag{4.18}$$

For a single layer material of area A this reduces to:

$$\bar{m} = \frac{A}{3}\rho t \tag{4.19}$$

4.3.2. Consistent mass matrix

If the virtual work expression of a general shell element is expanded to include dynamics, the virtual kinetic energy δK, virtual internal strain energy δU and virtual external potential δV are related over a time interval T as such:

$$\int_0^T \delta K - (\delta U - \delta V)\, dt = 0 \tag{4.20}$$

Focussing solely on the kinetic energy, pertinent to the consistent mass matrix, clarifying motion in three dimensions yields:

$$\delta K = \int_V \rho(\dot{u_1}\delta\dot{u_1} + \dot{u_2}\delta\dot{u_2} + \dot{u_3}\delta\dot{u_3})\, dV \tag{4.21}$$

The volume integral can be split into area and thickness integrals and referred to mid-plane velocities $(\dot{u_0},\ \dot{v_0},\ \dot{w_0})$:

$$\begin{aligned}\delta K = \int_\Omega \int_{\frac{-h}{2}}^{\frac{h}{2}} \rho\Big[&(\dot{u_0} + z\dot{\phi_1})(\delta\dot{u_0} + z\delta\dot{\phi_1}) + (\dot{v_0} + z\dot{\phi_2})(\delta\dot{v_0} + z\delta\dot{\phi_2}) + \\ &(\dot{w_0} + z\dot{\phi_3})(\delta\dot{w_0} + z\delta\dot{\phi_3})\Big]\, dz\, d\Omega\end{aligned} \tag{4.22}$$

The through-thickness integration can be simplified with the help of defining the following translational and rotational inertias under the assumption of constant density throughout the shell thickness:

$$\begin{aligned} I_i &= \int_{\frac{-h}{2}}^{\frac{h}{2}} \rho z^i\, dz \qquad (i = 0,\ 1,\ 2) \\ I_0 = \rho h\ , &\qquad I_1 = 0\ , \qquad I_2 = \frac{\rho h^3}{12} \end{aligned} \tag{4.23}$$

Substituting the inertias into equation 4.22 yields:

$$\delta K = \int_\Omega \rho\Big[I_0(\dot{u_0}\delta\dot{u_0} + \dot{v_0}\delta\dot{v_0} + \dot{w_0}\delta\dot{w_0}) + I_2(\dot{\phi_1}\delta\dot{\phi_1} + \dot{\phi_2}\delta\dot{\phi_2})\Big]\, d\Omega \tag{4.24}$$

Analogous to the method of discretized displacement field, the cartesian velocity and acceleration field can be expressed in terms of shape functions and discrete nodal quantities for both translational and rotational dofs, ordered as per equation 4.1:

$$\dot{\mathbf{u}}(x,y) = \sum_{i=1}^{3} N_i(x,y)\hat{\dot{\mathbf{u}}}_i \ , \qquad \ddot{\mathbf{u}}(x,y) = \sum_{i=1}^{3} N_i(x,y)\hat{\ddot{\mathbf{u}}}_i \ , \tag{4.25}$$

Considering equation 4.25, equation 4.24 can be developed into:

$$\delta K = \mathbf{M}_c \hat{\ddot{\mathbf{u}}} \delta\hat{\mathbf{u}} = \int_\Omega \rho \Big[I_0 \mathbf{N}_T^T \mathbf{N}_T + I_2 \mathbf{N}_R^T \mathbf{N}_R \Big] \, d\Omega \ \hat{\ddot{\mathbf{u}}} \delta\hat{\mathbf{u}} \tag{4.26}$$

The matrices $\mathbf{N}_T$ and $\mathbf{N}_R$ arrange shape functions to filter the appropriate translational and rotational DOFs respectively, defined as:

$$\mathbf{N}_T = \begin{pmatrix} \mathbf{N}_{T_1} & \mathbf{N}_{T_2} & \mathbf{N}_{T_3} \end{pmatrix} \ , \qquad \mathbf{N}_R = \begin{pmatrix} \mathbf{N}_{R_1} & \mathbf{N}_{R_2} & \mathbf{N}_{R_3} \end{pmatrix} \tag{4.27}$$

$$\mathbf{N}_{T_i} = \begin{pmatrix} N_i & 0 & 0 & 0 & 0 & 0 \\ 0 & N_i & 0 & 0 & 0 & 0 \\ 0 & 0 & N_i & 0 & 0 & 0 \\ 0 & 0 & 0 & 0 & 0 & 0 \\ 0 & 0 & 0 & 0 & 0 & 0 \\ 0 & 0 & 0 & 0 & 0 & 0 \end{pmatrix} \qquad \mathbf{N}_{R_i} = \begin{pmatrix} 0 & 0 & 0 & 0 & 0 & 0 \\ 0 & 0 & 0 & 0 & 0 & 0 \\ 0 & 0 & 0 & 0 & 0 & 0 \\ 0 & 0 & 0 & N_i & 0 & 0 \\ 0 & 0 & 0 & 0 & N_i & 0 \\ 0 & 0 & 0 & 0 & 0 & N_i \end{pmatrix} \tag{4.28}$$

4.4. Stress and strain recovery

While the stiffness and mass matrices enable the calculation of nodal displacements, velocities and accelerations, practical engineering analysis is usually more concerned with the strains and stresses of the structure. The non-zero local strains ($\epsilon_{zz} = 0$) of the 5 parameter element can be arranged in a vector form:

$$\boldsymbol{\epsilon}^T = \begin{pmatrix} \boldsymbol{\epsilon}_1 & \boldsymbol{\epsilon}_2 & \boldsymbol{\epsilon}_3 \end{pmatrix} \quad with \quad \boldsymbol{\epsilon}_i^T = \begin{pmatrix} \epsilon_{xx} & \epsilon_{xx} & 2\epsilon_{xy} & \kappa_{xx} & \kappa_{yy} & 2\kappa_{xy} & 2\epsilon_{xz} & 2\epsilon_{yz} \end{pmatrix} \tag{4.29}$$

The strain field within the element can be recovered from the displacement field by using the strain displacement matrix, which is constant over the element for the DSG triangle.

$$\boldsymbol{\epsilon}(\xi,\, \eta) = \mathbf{B}\, \mathbf{u}(\xi,\, \eta) \tag{4.30}$$

In typical finite element programs the strains and stresses are calculated at the Gauss points of the element, which is also how Kratos operates. Since the DSG has one Gauss point in the centre of the element, the strain is recovered from the discrete nodal displacements $\hat{\mathbf{u}}_i$ as follows:

$$\boldsymbol{\epsilon}_{GP} = \mathbf{B} \sum_{i=1}^{3\ nodes} N_i(\xi_{GP},\, \eta_{GP}) \hat{\mathbf{u}}_i \tag{4.31}$$

With the strains determined, the stresses at the Gauss points can be recovered with the material matrix at the Gauss point.

$$\boldsymbol{\sigma}_{GP} = \mathbf{C}_{GP}\, \boldsymbol{\epsilon}_{GP} \tag{4.32}$$

The general implementation of the stress and strain recovery described above is illustrated in the following pseudocode.

Algorithm 2 DSG triangle element stress and strain recovery

Require: $requestedQuantity$, calculation of nodal displacements
1: **call** `InitializeCalculationData`$(data)$
2: Calculate strain-displacement matrix B
3: Retrieve element $localDisplacements$
4: $generalizedStrains$ = product$(B,\, localDisplacements)$
5: **if** $requestedQuantity$ requires stress **then**
6: **call** `CalculateSectionResponse`$(data)$
7: $generalizedStresses$ = product $(C,\, generalizedStrains)$
8: Decimal correction of $generalizedStresses$
9: **end if**
10: Decimal correction of $generalizedStrains$
11: **if** $requestedQuantity$ requires local orientation **then**
12: Rotate $requestedQuantity$ to local orientation
13: **end if**
14: Assemble $requestedQuantity$ into $outputMatrix$
15: **if** $requestedQuantity$ requires global orientation **then**
16: Rotate $outputMatrix$ to global orientation
17: **end if**
18: Interpolate $outputMatrix$ to standard Gauss points for visualisation

Chapter 5 ANDES-DKQ quadrilateral shell element

The stiffness matrix, mass matrix and quantity recovery for the ANDES-DKQ quadrilateral shell element in Kratos are covered in this chapter.

5.1. Stiffness matrix formulation

Unlike the DSG triangle, the ANDES-DKQ element uses different finite element technologies for the membrane and bending components, both of which are subsequently developed.

5.1.1. ANDES membrane formulation

The membrane formulation is responsible for providing the membrane stiffness of the element. The membrane formulation chosen was the Assumed Natural Deviatoric Strains (ANDES) formulation as presented in [22]. A full description and theoretical derivation of the ANDES approach falls outside the scope of this document, however, those interested are directed to Militello's and Felippa's initial paper [28] on the formulation. Most importantly, the ANDES approach yields high performance elements that are insensitive to distortion.

Only the membrane portion of the total shell element is considered in this section, in which there are three DOFs per node.

$$\mathbf{u}^T = \begin{pmatrix} \mathbf{u}_1 & \mathbf{u}_2 & \mathbf{u}_3 & \mathbf{u}_4 \end{pmatrix} \qquad where \qquad \mathbf{u}_i{}^T = \begin{pmatrix} u_{xi} & u_{yi} & \beta_{zi} \end{pmatrix} \tag{5.1}$$

The ANDES membrane formulation itself is split into the basic stiffness related to the basic constant strain displacement matrix $\mathbf{L}$ and the higher order stiffness related to the higher order deviatoric strain displacement matrix $\mathbf{B}_d$.

$$\mathbf{K}_{mem} = \mathbf{K}_b + \mathbf{K}_h = \int_A (\mathbf{L} + \mathbf{B}_d)^T \mathbf{C}_{mem} (\mathbf{L} + \mathbf{B}_d)\, dA \tag{5.2}$$

The basic strain displacement matrix $\mathbf{L}$ and the higher order complement $\mathbf{B}_d$ are now developed.

Membrane basic stiffness

The membrane basic stiffness is driven by assuming a constant stress field within the element and lumping this over side edges to consistent nodal forces.

$$\mathbf{f} = \boldsymbol{L\sigma} \qquad where \qquad \boldsymbol{\sigma}^T = \begin{pmatrix} \sigma_{xx} & \sigma_{xx} & \tau_{xy} \end{pmatrix} \tag{5.3}$$

The structure of the above expression is resolved as such:

$$\mathbf{L} = \begin{pmatrix} \mathbf{L}_1 & \mathbf{L}_2 & \mathbf{L}_3 & \mathbf{L}_4 \end{pmatrix} \qquad and \qquad \mathbf{f} = \begin{pmatrix} \mathbf{f}_1 \\ \mathbf{f}_2 \\ \mathbf{f}_3 \\ \mathbf{f}_4 \end{pmatrix} \qquad where \qquad \mathbf{f}_i = \begin{pmatrix} f_{xi} \\ f_{yi} \\ m_{zi} \end{pmatrix} \tag{5.4}$$

where each nodal entry 'j' of the lumping matrix $\mathbf{L}$ is constructed with the following cyclic permutation $(i,\ j,\ k,\ l)$ for the four nodes $(1,\ 2,\ 3,\ 4)$:

$$\mathbf{L}_j = \frac{1}{2A} \begin{pmatrix} y_{ki} & 0 & -x_{ki} \\ 0 & -x_{ki} & y_{ki} \\ \frac{\alpha}{6}(y_{ij}^2 - y_{kj}^2) & \frac{\alpha}{6}(x_{ij}^2 - x_{kj}^2) & \frac{\alpha}{3}(x_{kj}y_{kj} - x_{ij}y_{ij}) \end{pmatrix} \tag{5.5}$$

Throughout this formulation the notation of $x_{ij} = x_i - x_j$ and $y_{ij} = y_i\ -\ y_j$ holds. Furthermore, the value of α is taken as 1.5 [28].

Membrane higher order stiffness

The membrane higher order stiffness considers a set of higher order DOFs expressed in terms of the visible DOFs as per equation (5.1).

It should be noted that the derviation below slightly departs from the formulation of Haugen [22] due to the DOF ordering as per equation (5.1).

The higher order rotational DOFs are related to the visible DOFs as described below:

$$\boldsymbol{\theta}_h = \mathbf{H}_{\theta v}\mathbf{u} \qquad where \qquad \boldsymbol{\theta}_h^T = \begin{pmatrix} \theta_1' & \theta_2' & \theta_3' & \theta_4' & \bar{\theta} \end{pmatrix} \tag{5.6}$$

with

$$\mathbf{H}_{\theta \mathbf{v}} = \begin{pmatrix} 0 & 0 & \frac{3}{4} & 0 & 0 & \frac{-1}{4} & 0 & 0 & \frac{-1}{4} & 0 & 0 & \frac{-1}{4} \\ 0 & 0 & \frac{-1}{4} & 0 & 0 & \frac{3}{4} & 0 & 0 & \frac{-1}{4} & 0 & 0 & \frac{-1}{4} \\ 0 & 0 & \frac{-1}{4} & 0 & 0 & \frac{-1}{4} & 0 & 0 & \frac{3}{4} & 0 & 0 & \frac{-1}{4} \\ 0 & 0 & \frac{-1}{4} & 0 & 0 & \frac{-1}{4} & 0 & 0 & \frac{-1}{4} & 0 & 0 & \frac{3}{4} \\ \frac{x_{42}}{f} & \frac{y_{42}}{f} & \frac{1}{4} & \frac{x_{13}}{f} & \frac{y_{13}}{f} & \frac{1}{4} & \frac{x_{24}}{f} & \frac{y_{24}}{f} & \frac{1}{4} & \frac{x_{31}}{f} & \frac{y_{31}}{f} & \frac{1}{4} \end{pmatrix}$$

$$where \qquad f = 16|\mathbf{J}|$$

$$and \qquad |\mathbf{J}| = \frac{1}{8}[(x_1y_2 - x_2y_1) + (x_2y_3 - x_3y_2) + (x_3y_4 - x_4y_3) + (x_4y_1 - x_1y_4)] \tag{5.7}$$

The higher order translational DOFs are related to the visible DOFs as described below:

$$\widetilde{\mathbf{v}}_t = \mathbf{H}_{tv}\mathbf{u} \qquad where \qquad \widetilde{\mathbf{v}}_t^T = \begin{pmatrix} \widetilde{v}_x & \widetilde{v}_y \end{pmatrix} \tag{5.8}$$

with

$$\mathbf{H}_{tv} = \begin{pmatrix} 1 & 0 & 0 & -1 & 0 & 0 & 1 & 0 & 0 & -1 & 0 & 0 \\ 0 & 1 & 0 & 0 & -1 & 0 & 0 & 1 & 0 & 0 & -1 & 0 \end{pmatrix} \tag{5.9}$$

Combining both mapping matrices together expresses all higher order DOFs in terms of the visible DOFs:

$$\widetilde{\mathbf{v}} = \mathbf{H}\mathbf{v} \qquad where \qquad \mathbf{H} = \begin{pmatrix} \mathbf{H}_{\theta v} \\ \mathbf{H}_{vt} \end{pmatrix} \qquad and \qquad \widetilde{\mathbf{v}}^T = \begin{pmatrix} \theta_1' & \theta_2' & \theta_3' & \theta_4' & \bar{\theta} & \widetilde{v}_x & \widetilde{v}_y \end{pmatrix} \tag{5.10}$$

The descriptions for equations from (5.13) to (5.28) are heavily abridged from the original element derivation [22]. The general idea of these equations is to relate the higher order nodal strain gauge readings to cartesian strain displacement matrices $\mathbf{B}_{hi}$.

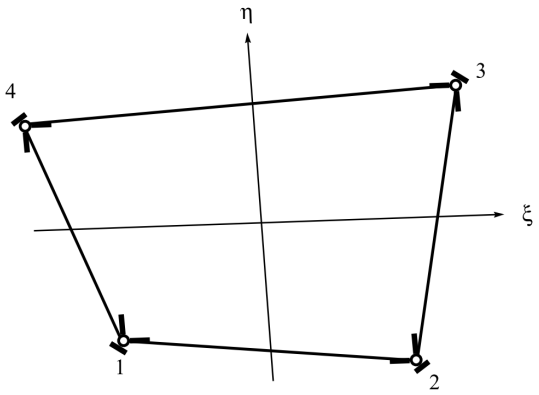

Figure 23 ANDES membrane nodal strain gauges [22]

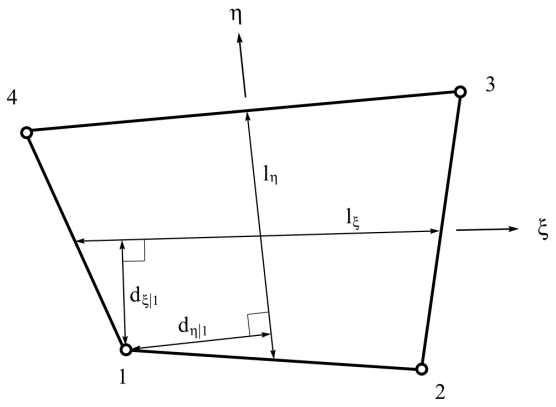

Figure 24 Geometric dimensions of the quadrilateral element [22]

The strain gauges are placed as per figure 23 and read strains along the ξ and η axes as well as the element diagonals. At each strain gauge, the readings are thus:

$$\boldsymbol{\epsilon}_1 = \boldsymbol{\epsilon}_3 = \begin{pmatrix} \epsilon_\xi \\ \epsilon_\eta \\ \epsilon_{24} \end{pmatrix}, \qquad \boldsymbol{\epsilon}_2 = \boldsymbol{\epsilon}_4 = \begin{pmatrix} \epsilon_\xi \\ \epsilon_\eta \\ \epsilon_{13} \end{pmatrix} \tag{5.11}$$

The strain readings are related to the higher order degrees of freedom via the nodal strain templates $\mathbf{Q}_i$.

$$\boldsymbol{\epsilon}_i = \mathbf{Q}_i \widetilde{\mathbf{v}} \tag{5.12}$$

Higher order bending field

As per Haugen's PhD thesis, the primary strain mode the field is trying to match is pure bending of an element in an arbitrary direction. The bending strain field is associated with the higher order DOFs of $\theta_i^{'}, \widetilde{v}_\xi$ and $\widetilde{v}_\eta$, and is intuited to be proportional to the distance from the neutral axis of the direction considered. For instance, bending in the ξ direction is assumed proportional to the distance d_ξ (refer figure 24) and the curvature of the element $\frac{\Delta\theta}{l_\xi}$. Thus the general form of the ξ strains are $\frac{d_{\xi|i}}{l_\xi}$, with the η strains derived in a similar manner. The bending strains at each node are:

$$\chi_{\xi|i} = \frac{d_{\xi|i}}{l_\xi}, \qquad \chi_{\eta|i} = \frac{d_{\eta|i}}{l_\eta}, \tag{5.13}$$

where the quantities in figure 24 are calculated as follows:

$$d_{\xi|i} = \sqrt{(\mathbf{r}_i \times \mathbf{s}_\xi) \cdot (\mathbf{r}_i \times \mathbf{s}_\xi)}\,, \qquad l_\xi = \sqrt{\mathbf{r}_\xi \cdot \mathbf{r}_\xi}\,, \qquad \mathbf{r}_\xi = \frac{1}{2}(\mathbf{r}_2 + \mathbf{r}_3 - \mathbf{r}_1 - \mathbf{r}_4)\,,$$
$$d_{\eta|i} = \sqrt{(\mathbf{r}_i \times \mathbf{s}_\eta) \cdot (\mathbf{r}_i \times \mathbf{s}_\eta)}\,, \qquad l_\xi = \sqrt{\mathbf{r}_\eta \cdot \mathbf{r}_\eta}\,, \qquad \mathbf{r}_\eta = \frac{1}{2}(\mathbf{r}_2 + \mathbf{r}_3 - \mathbf{r}_1 - \mathbf{r}_4)\,,$$

$\mathbf{s}_\xi$ and $\mathbf{s}_\eta$ are the normalized parametric base vectors in cartesian coordinates, while $\mathbf{r}_i$ are the nodal position vectors in cartesian coordinates.

The diagonal strain components of the higher order bending field are also assumed as to be proportional to the distance and curvature along the diagonal, thus yielding:

$$\chi_{24} = \frac{d_{24}}{2l_{24}}, \qquad \chi_{13} = \frac{d_{13}}{2l_{13}}, \tag{5.14}$$

where

$$d_{24} = d_{13} = \sqrt{(\mathbf{r}_{31} \times \mathbf{e}_{24}) \cdot (\mathbf{r}_{31} \times \mathbf{e}_{24})} \qquad l_{24} = \sqrt{\mathbf{r}_{24} \cdot \mathbf{r}_{24}}\,, \qquad \mathbf{r}_{24} = \mathbf{r}_2 - \mathbf{r}_4$$
$$l_{13} = \sqrt{\mathbf{r}_{13} \cdot \mathbf{r}_{13}}\,, \qquad \mathbf{r}_{13} = \mathbf{r}_1 - \mathbf{r}_3 \qquad \mathbf{e}_{24} = \frac{\mathbf{r}_{24}}{l_{24}}$$

Higher order torsional field

The higher order torsional field is associated with the $\bar{\theta}$ higher order DOF. Figure 25 illustrates the general torsional displacement mode shape, indicating that no shear strains are produced in this mode.

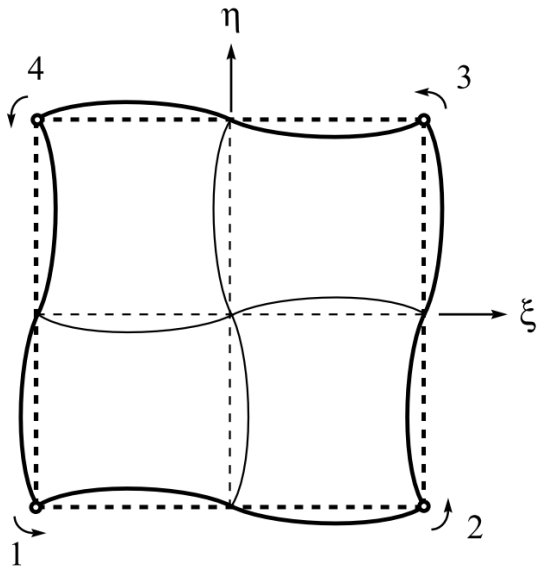

Figure 25 Higher order torsional mode of ANDES membrane formulation [22]

Under this torsional regime, ϵ_ξ is positive in the 1st and 3rd quadrants and negative in the 2nd and 4th quadrants, while ϵ_η has the opposite signs. Furthermore, with a unit rotation at each node the maximum displacement v_ξ will be proportional to l_η. Recalling that ϵ_ξ is the gradient of v_ξ in the ξ direction, one can suppose that ϵ_ξ is proportional to $\frac{1}{l_\xi}$. Considering this approach for ϵ_ξ and ϵ_η, the following torsional strain field terms are determined:

$$\chi_{\xi t} = \frac{l_\eta}{l_\xi} \ , \qquad \chi_{\eta t} = \frac{l_\xi}{l_\eta} \ , \tag{5.15}$$

Higher order nodal strain templates

Considering the higher order bending and torsional components just outlined, the nodal strain gauge readings can be described as follows:

$$\mathbf{Q}_1 = \begin{pmatrix} \rho_1\chi_{\xi|1} & \rho_2\chi_{\xi|1} & \rho_3\chi_{\xi|1} & \rho_4\chi_{\xi|1} & \alpha\chi_{\xi t} & -\beta_1\frac{\chi_{\xi|1}}{\bar{\chi}_\xi l_\xi} & 0 \\ -\rho_1\chi_{\eta|1} & -\rho_4\chi_{\eta|1} & -\rho_3\chi_{\eta|1} & -\rho_2\chi_{\eta|1} & -\alpha\chi_{\eta t} & 0 & -\beta_1\frac{\chi_{\eta|1}}{\bar{\chi}_\eta l_\eta} \\ \rho_5\chi_{24} & \rho_6\chi_{24} & \rho_7\chi_{24} & \rho_8\chi_{24} & 0 & \beta_2\frac{c_{24\xi}}{l_{24}} & -\beta_2\frac{c_{24\eta}}{l_{24}} \end{pmatrix} \tag{5.16}$$

$$\mathbf{Q}_2 = \begin{pmatrix} -\rho_2\chi_{\xi|2} & -\rho_1\chi_{\xi|2} & -\rho_4\chi_{\xi|2} & -\rho_3\chi_{\xi|2} & -\alpha\chi_{\xi t} & -\beta_1\frac{\chi_{\xi|2}}{\bar{\chi}_\xi l_\xi} & 0 \\ \rho_4\chi_{\eta|2} & \rho_1\chi_{\eta|2} & \rho_2\chi_{\eta|2} & \rho_3\chi_{\eta|2} & \alpha\chi_{\eta t} & 0 & \beta_1\frac{\chi_{\eta|2}}{\bar{\chi}_\eta l_\eta} \\ \rho_8\chi_{13} & \rho_5\chi_{13} & \rho_6\chi_{13} & \rho_7\chi_{13} & 0 & -\beta_2\frac{c_{13\xi}}{l_{13}} & \beta_2\frac{c_{13\eta}}{l_{13}} \end{pmatrix} \tag{5.17}$$

$$\mathbf{Q}_3 = \begin{pmatrix} \rho_3\chi_{\xi|3} & \rho_4\chi_{\xi|3} & \rho_1\chi_{\xi|3} & \rho_2\chi_{\xi|3} & \alpha\chi_{\xi t} & \beta_1\frac{\chi_{\xi|3}}{\bar{\chi}_\xi l_\xi} & 0 \\ -\rho_3\chi_{\eta|3} & -\rho_2\chi_{\eta|3} & -\rho_1\chi_{\eta|3} & -\rho_4\chi_{\eta|3} & -\alpha\chi_{\eta t} & 0 & \beta_1\frac{\chi_{\eta|3}}{\bar{\chi}_\eta l_\eta} \\ \rho_7\chi_{13} & \rho_8\chi_{13} & \rho_5\chi_{13} & \rho_6\chi_{213} & 0 & -\beta_2\frac{c_{13\xi}}{l_{13}} & \beta_2\frac{c_{13\eta}}{l_{13}} \end{pmatrix} \tag{5.18}$$

$$\mathbf{Q}_4 = \begin{pmatrix} -\rho_4\chi_{\xi|4} & -\rho_3\chi_{\xi|4} & -\rho_2\chi_{\xi|4} & -\rho_1\chi_{\xi|4} & -\alpha\chi_{\xi t} & \beta_1\frac{\chi_{\xi|4}}{\bar{\chi}_\xi l_\xi} & 0 \\ \rho_2\chi_{\eta|4} & \rho_3\chi_{\eta|4} & \rho_4\chi_{\eta|4} & \rho_1\chi_{\eta|4} & \alpha\chi_{\eta t} & 0 & -\beta_1\frac{\chi_{\eta|4}}{\bar{\chi}_\eta l_\eta} \\ \rho_6\chi_{13} & \rho_7\chi_{13} & \rho_8\chi_{13} & \rho_5\chi_{13} & 0 & \beta_2\frac{c_{13\xi}}{l_{13}} & -\beta_2\frac{c_{13\eta}}{l_{13}} \end{pmatrix} \tag{5.19}$$

where

$$c_{13\xi} = \mathbf{s}_{13}^T\mathbf{s}_\xi \ , \qquad c_{13\eta} = \mathbf{s}_{13}^T\mathbf{s}_\eta \ , \qquad c_{24\xi} = \mathbf{s}_{24}^T\mathbf{s}_\xi \ , \qquad c_{24\eta} = \mathbf{s}_{24}^T\mathbf{s}_\eta$$

An optimisation of element performance has suggested the following coefficients to be used in the nodal strain gauge templates [22].

$$\begin{aligned} &\rho_1 = 0.1\ , \qquad \rho_2 = -0.1\ , \qquad \rho_3 = -0.1\ , \qquad \rho_4 = 0.1\ , \qquad \rho_5 = 0.0\ , \\ &\rho_6 = 0.5\ , \qquad \rho_7 = 0.0\ , \qquad \rho_8 = -0.5\ , \qquad \beta_1 = 0.6\ , \qquad \beta_2 = 0.0 \end{aligned} \tag{5.20}$$

Cartesian higher order strain displacement matrix

The cartesian strain displacement matrices at the nodes are related to the mapping matrices $\mathbf{Q}_i$ as described below:

$$\begin{aligned} &\mathbf{B}_{h1} = \mathbf{T}_{13}\mathbf{Q}_1\ , \qquad \mathbf{B}_{h3} = \mathbf{T}_{13}\mathbf{Q}_3 \\ &where \qquad \mathbf{T}_{13}^{-1} = \begin{pmatrix} s_{\xi x}^2 & s_{\xi y}^2 & s_{\xi x}s_{\xi y} \\ s_{\eta x}^2 & s_{\eta y}^2 & s_{\eta x}s_{\eta y} \\ s_{24x}^2 & s_{24y}^2 & s_{24x}s_{24y} \end{pmatrix} \end{aligned} \tag{5.21}$$

$$\begin{aligned} &\mathbf{B}_{h2} = \mathbf{T}_{24}\mathbf{Q}_2\ , \qquad \mathbf{B}_{h4} = \mathbf{T}_{24}\mathbf{Q}_4 \\ &where \qquad \mathbf{T}_{24}^{-1} = \begin{pmatrix} s_{\xi x}^2 & s_{\xi y}^2 & s_{\xi x}s_{\xi y} \\ s_{\eta x}^2 & s_{\eta y}^2 & s_{\eta x}s_{\eta y} \\ s_{13x}^2 & s_{13y}^2 & s_{13x}s_{13y} \end{pmatrix} \end{aligned} \tag{5.22}$$

The higher order membrane B matrix $\mathbf{B}_h$ is constructed from the interpolation of the nodal B matrices with standard bi-linear shape functions.

$$\mathbf{B}_h(\xi,\eta) = (1-\xi)(1-\eta)\mathbf{B}_{h1} + (1+\xi)(1-\eta)\mathbf{B}_{h2} + (1+\xi)(1+\eta)\mathbf{B}_{h3} + (1-\xi)(1+\eta)\mathbf{B}_{h4} \tag{5.23}$$

The current strain field interpolation is not energy orthogonal to the basic strain field yet. This deviatoric condition can be achieved by subtracting the mean integral:

$$\mathbf{B}_d(\xi,\eta) = \mathbf{B}_h(\xi,\eta) - \bar{\mathbf{B}}_h \qquad with \qquad \bar{\mathbf{B}}_h = \int_A \mathbf{B}_h(\xi,\eta)\, dA \tag{5.24}$$

5.1.2. DKQ bending formulation

The bending formulation is responsible for providing the bending stiffness of the element. The bending formulation chosen was the Discrete Kirchhoff Quadrilateral (DKQ) formulation originally presented by Batoz [5], presented in a most readable fashion in the PhD dissertation of Barrales [2]. A full description and theoretical derivation of the DKQ approach falls outside the scope of this document, refer [5]. Most importantly for a thin shell element, the transverse shear strain energy is neglected which prohibits element performance deterioration as the ratio $\frac{l}{t}$ encroaches into thin and very thin plate territories.

Only the bending portion of the total shell element is considered in this section, in which there are three nodal DOFs per node (w_i corresponds to u_{zi} in the figure below).

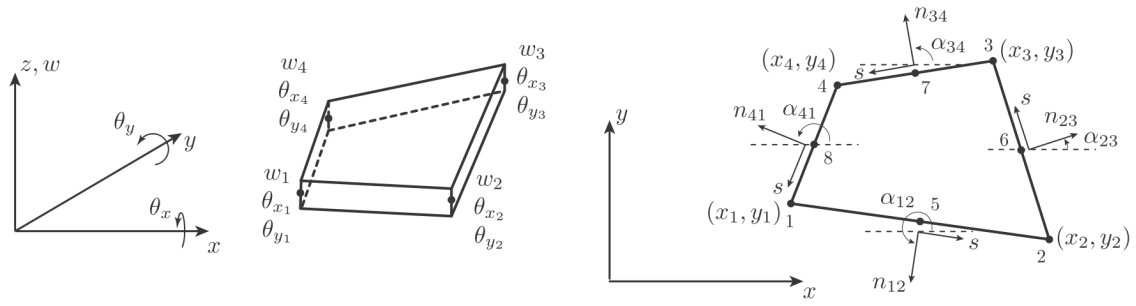

Figure 26 DKQ DOF arrangement and geometry [2]

$$\mathbf{u}^T = \begin{pmatrix} \mathbf{u}_1 & \mathbf{u}_2 & \mathbf{u}_3 & \mathbf{u}_4 \end{pmatrix} \qquad where \qquad \mathbf{u}_i{}^T = \begin{pmatrix} u_{zi} & \theta_{xi} & \theta_{yi} \end{pmatrix} \tag{5.25}$$

The nodal rotational interpolation employed is as per the 8 node serendipity quad element:

$$\begin{pmatrix} \beta_x(\xi,\eta) \\ \beta_y(\xi,\eta) \end{pmatrix} = \sum_{i=1}^{8} \psi_i(\xi,\eta) \begin{pmatrix} \beta_{xi}(\xi,\eta) \\ \beta_{yi}(\xi,\eta) \end{pmatrix} \tag{5.26}$$

where ψ_i are the standard 8 node serendipity shape functions described by Zienkiewicz [44]:

$$\begin{aligned}
\psi_i(\xi,\eta) &= \frac{-1}{4}(1+\xi_i\xi)(1+\eta_i\eta)(1-\xi_i\xi-\eta_i\eta) \qquad i=1,2,3,4 \\
\psi_i(\xi,\eta) &= \frac{1}{2}(1-\xi^2)(1+\eta_i\eta) \qquad i=5,7 \\
\psi_i(\xi,\eta) &= \frac{1}{2}(1+\xi_i\xi)(1-\eta^2) \qquad i=6,8
\end{aligned} \tag{5.27}$$

and ξ_i and η_i are the natural coordinates of the 8 node serendipity element described in figure 26.

The following derivation from equations (5.28) to (5.33) is heavily summarised from that of Barrales [2]. The general idea is the construction of a mapping from the standard 12 DOFs at each node to $\beta_x(\xi,\,\eta)$ and $\beta_y(\xi,\,\eta)$ across the element, the derivatives of which are curvatures as expressed in equation (5.33).

The following quantities are required components for the mapping:

$$L_{ij} = \sqrt{x_{ij}^2+y_{ij}^2}\,, \qquad x_{ij} = x_i - x_j\,, \qquad y_{ij} = y_i - y_j \tag{5.28}$$

$$\begin{aligned}
a_k &= \frac{-x_{ij}}{L_{ij}^2}\,, \qquad b_k = \frac{3}{4}\frac{x_{ij}y_{ij}}{L_{ij}^2}\,, \\
c_k &= \frac{\frac{1}{4}x_{ij}^2 - \frac{1}{2}y_{ij}^2}{L_{ij}^2}\,, \qquad d_k = \frac{-y_{ij}}{L_{ij}^2}\,, \qquad e_k = \frac{\frac{-1}{2}x_{ij}^2 + \frac{1}{4}y_{ij}^2}{L_{ij}^2}
\end{aligned} \tag{5.29}$$

The elements of the mapping matrix are arranged as such:

$$\mathbf{\Psi}^x = \begin{pmatrix} \Psi_1^x \\ \vdots \\ \Psi_{12}^x \end{pmatrix}\,, \qquad \mathbf{\Psi}^y = \begin{pmatrix} \Psi_1^y \\ \vdots \\ \Psi_{12}^y \end{pmatrix} \tag{5.30}$$

where the vectors entries are calculated as per the following scheme:

$$
\begin{aligned}
\Psi^x_{3(i-1)+1}(\xi,\eta) &= \frac{3}{2}(a_r\psi_r(\xi,\eta) - a_s\psi_s(\xi,\eta)) \\
\Psi^x_{3(i-1)+2}(\xi,\eta) &= b_r\psi_r(\xi,\eta) + b_s\psi_s(\xi,\eta) \\
\Psi^x_{3(i-1)+3}(\xi,\eta) &= \psi_i(\xi,\eta) - c_r\psi_r(\xi,\eta) - c_s\psi_s(\xi,\eta)
\end{aligned} \tag{5.31}
$$

$$
\begin{aligned}
\Psi^y_{3(i-1)+1}(\xi,\eta) &= \frac{3}{2}(d_r\psi_r(\xi,\eta) - d_s\psi_s(\xi,\eta)) \\
\Psi^y_{3(i-1)+2}(\xi,\eta) &= -\psi_i(\xi,\eta) + e_r\psi_r(\xi,\eta) + c_s\psi_s(\xi,\eta) \\
\Psi^y_{3(i-1)+3}(\xi,\eta) &= -b_r\psi_r(\xi,\eta) - b_s\psi_s(\xi,\eta)
\end{aligned} \tag{5.32}
$$

with i = 1, 2, 3, 4 and the relationship $(i,\ r,\ s)$ as (1, 5, 8), (2, 6, 5), (3, 7, 6) and (4, 8, 7).

Relating curvatures to displacements yield:

$$
\boldsymbol{\chi} = \mathbf{B}_{bend}\mathbf{U} \tag{5.33}
$$

with $\mathbf{B}_{bend}$ constructed as follows:

$$
\mathbf{B}_{bend} = \begin{pmatrix} \frac{\partial \boldsymbol{\Psi}^{x^T}}{\partial x} \\ \frac{\partial \boldsymbol{\Psi}^{y^T}}{\partial y} \\ \frac{\partial \boldsymbol{\Psi}^{x^T}}{\partial y} + \frac{\partial \boldsymbol{\Psi}^{y^T}}{\partial x} \end{pmatrix} = \begin{pmatrix} j_{11}\frac{\partial \boldsymbol{\Psi}^{x^T}}{\partial \xi} + j_{12}\frac{\partial \boldsymbol{\Psi}^{x^T}}{\partial \eta} \\ j_{21}\frac{\partial \boldsymbol{\Psi}^{y^T}}{\partial \xi} + j_{22}\frac{\partial \boldsymbol{\Psi}^{y^T}}{\partial \eta} \\ j_{11}\frac{\partial \boldsymbol{\Psi}^{y^T}}{\partial \xi} + j_{12}\frac{\partial \boldsymbol{\Psi}^{y^T}}{\partial \eta} + j_{21}\frac{\partial \boldsymbol{\Psi}^{x^T}}{\partial \xi} + j_{22}\frac{\partial \boldsymbol{\Psi}^{x^T}}{\partial \eta} \end{pmatrix} \tag{5.34}
$$

and the inverse Jacobian entries $j_{\alpha\beta}$:

$$
\begin{aligned}
\mathbf{J} &= \frac{1}{4}\begin{pmatrix} x_{21}+x_{34}+\eta(x_{12}+x_{34}) & y_{21}+y_{34}+\eta(y_{12}+y_{34}) \\ x_{32}+x_{41}+\xi(x_{12}+x_{34}) & y_{32}+y_{41}+\xi(y_{12}+y_{34}) \end{pmatrix} = \begin{pmatrix} J_{11} & J_{12} \\ J_{21} & J_{22} \end{pmatrix} \\
j_{11} &= \frac{J_{22}}{det[J]}\ , \qquad j_{12} = \frac{-J_{12}}{det[J]}\ , \qquad j_{21} = \frac{-J_{21}}{det[J]}\ , \qquad j_{22} = \frac{J_{11}}{det[J]}
\end{aligned} \tag{5.35}
$$

5.1.3. Combined formulation

With the separate membrane and bending B matrices developed, the combined shell B matrix $\mathbf{B}_{comb.}$ can be constructed to form the element stiffness matrix.

$$\mathbf{K}_{el} = \mathbf{B}_{comb}^{T}\mathbf{C}\mathbf{B}_{comb} \tag{5.36}$$

$$\mathbf{B}_{comb} = (\mathbf{L}+\mathbf{B}_{h})+\mathbf{B}_{bend} = \mathbf{B}_{mem}+\mathbf{B}_{bend} = \begin{pmatrix} \mathbf{B}_{comb1} & \mathbf{B}_{comb2} & \mathbf{B}_{comb3} & \mathbf{B}_{comb4} \end{pmatrix} \tag{5.37}$$

The combination of $membrane$ and $bending$ matrices must consider the DOF ordering of each component and the relation to the total shell DOF ordering, as shown below:

$$\mathbf{u}_i = \begin{pmatrix} u_{xi} \\ u_{yi} \\ u_{zi} \\ \beta_{xi} \\ \beta_{yi} \\ \beta_{zi} \end{pmatrix} \tag{5.38}$$

Considering this, the addition of the membrane (basic and higher order) B matrices and the bending B matrix is conducted for each node *i* as follows:

$$\mathbf{B}_{comb\ i} = \begin{pmatrix} \mathbf{B}_{mem}[1,3(i-1)+1] & \mathbf{B}_{mem}[1,3(i-1)+2] & 0 \\ \mathbf{B}_{mem}[2,3(i-1)+1] & \mathbf{B}_{mem}[2,3(i-1)+2] & 0 \\ 0 & 0 & \mathbf{B}_{bend}[1,3(i-1)+1] \\ 0 & 0 & \mathbf{B}_{bend}[2,3(i-1)+1] \\ 0 & 0 & \mathbf{B}_{bend}[3,3(i-1)+1] \\ \mathbf{B}_{mem}[3,3(i-1)+1] & \mathbf{B}_{mem}[3,3(i-1)+2] & 0 \end{pmatrix}$$
$$\begin{pmatrix} 0 & 0 & \mathbf{B}_{mem}[1,3(i-1)+3] \\ 0 & 0 & \mathbf{B}_{mem}[2,3(i-1)+3] \\ \mathbf{B}_{bend}[1,3(i-1)+2] & \mathbf{B}_{bend}[1,3(i-1)+3] & 0 \\ \mathbf{B}_{bend}[2,3(i-1)+2] & \mathbf{B}_{bend}[2,3(i-1)+3] & 0 \\ \mathbf{B}_{bend}[3,3(i-1)+2] & \mathbf{B}_{bend}[3,3(i-1)+3] & 0 \\ 0 & 0 & \mathbf{B}_{mem}[3,3(i-1)+3] \end{pmatrix} \tag{5.39}$$

5.2. Stiffness matrix implementation

With the formulation of the ANDES-DKQ shell element established, a high level overview of it's implementation in KRATOS is discussed in this section.

The new quad element is implemented in the files `shell_thin_element_3D4N.hpp` and `shell_thin_element_3D4N.cpp`, which are compiled into the 'StructuralMechanicsApplication' module of Kratos. Similar to the DSG triangle element, the new ANDES-DKQ element class `ShellThinElement3D4N` is inherited from the Kratos base class `Element` and also leverages the existing capabilities other Kratos classes offer. The general workflow of calculating the ANDES-DKQ stiffness matrix is as follows:

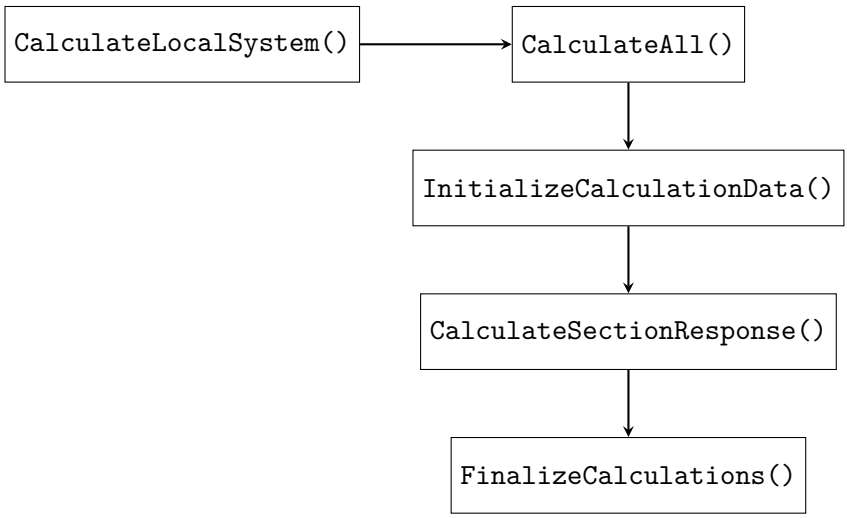

Figure 27 High level overview of ANDES-DKQ element workflow

As per the DSG triangle element, the re-implemented virtual method `CalculateLocalSystem()` is called by the KRATOS framework automatically for every `ShellThinElement3D4N` in the job definition. This method simply calls `CalculateAll()`, which initializes calculating the stiffness matrix by calling `InitializeCalculationData()`, `CalculateGaussPointContribution()` and `FinalizeCalculations()`.

`InitializeCalculationData()` is called first, and pre-calculates quantities so they can be removed from the Gauss loop. These quantities include the ANDES basic lumping matrix **L**, the ANDES higher order strain-displacement matrices $\mathbf{B}_{hi}$ and all DKQ coefficients in equation (5.29).

`CalculateAll()` then calls `CalculateGaussPointContribution()` which starts the Gauss integration loop. At each Gauss point `CalculateGaussPointContribution()` performs Gauss integration of the expression $\mathbf{K}_{contribution} = \mathbf{B}_{comb}^{T}\mathbf{C}\mathbf{B}_{comb}\ dA$, with the current $\mathbf{B}_{comb}$ determined by calling `CalculateBMatrix()`.

With the Gauss integration complete, `CalculateAll()` lastly calls `FinalizeCalculations()` which transforms the calculated element stiffness from local to global coordinates.

The following pseudocode summarises the key calls and operations involved in calculating the ANDES-DKQ element stiffness matrix.

Algorithm 3 ANDES-DKQ element stiffness matrix pseudocode

Require: Coordinate transformation instance

call `CalculateAll()`
Resize LHS and RHS
call `InitializeCalculationData`$(data)$
    Calculate integration areas $dA = w_i \cdot detJ(xi,\ eta)$
    Determine basic membrane strain displacement L
    Construct membrane higher order filter matrix H
    Arrange higher order natural strain matrices Q_i
    Transform Q_i into B_{hi}
    Determine $\bar{B_h}$
    Pre-calculate all DKQ coefficients
while $gaussPoint$ < 4 **do**
    call `CalculateGaussPointContribution`$(data)$
        call `CalculateBMatrix`$(data)$
            Calculate and combine B_{mem} and B_{bend} into B
        call `CalculateSectionResponse`$(data)$
            Calculate material properties C
        Add stiffness matrix Gauss point contribution to LHS
end while
Modify RHS residual vector
call `FinalizeCalculations`$(data,\ displacements,\ LHS,\ RHS)$
call `AddBodyForces`$(data,\ RHS)$

5.3. Mass matrix formulation

The mass matrix is necessary to facilitate dynamic analysis with the thin quadrilateral shell element. As per the existing KRATOS shell elements, a lumped mass approach is employed which results in a diagonal mass matrix.

$$\mathbf{M} = \begin{pmatrix} \mathbf{M}_1 & \mathbf{0} & \mathbf{0} & \mathbf{0} \\ \mathbf{0} & \mathbf{M}_2 & \mathbf{0} & \mathbf{0} \\ \mathbf{0} & \mathbf{0} & \mathbf{M}_3 & \mathbf{0} \\ \mathbf{0} & \mathbf{0} & \mathbf{0} & \mathbf{M}_4 \end{pmatrix} \qquad where \qquad \mathbf{M}_i = \begin{pmatrix} \bar{m} & 0 & 0 & 0 & 0 & 0 \\ 0 & \bar{m} & 0 & 0 & 0 & 0 \\ 0 & 0 & \bar{m} & 0 & 0 & 0 \\ 0 & 0 & 0 & 0 & 0 & 0 \\ 0 & 0 & 0 & 0 & 0 & 0 \\ 0 & 0 & 0 & 0 & 0 & 0 \end{pmatrix} \tag{5.40}$$

The general lumped mass is determined for a multi-ply material with n plies each of t_i thickness and ρ_i density as follows:

$$\bar{m} = \frac{A}{4} \sum_{i=1}^{n} \rho_i t_i \tag{5.41}$$

For a single layer material of area A this reduces to:

$$\bar{m} = \frac{A}{4} \rho t \tag{5.42}$$

5.4. Stress and strain recovery

The stresses and strains of the ANDES-DKT quadrilateral element are recovered in a similar way to the DSG triangle, with the added complication of the multiple Gauss points.

The non-zero local strains ($\epsilon_{zz},\ \epsilon_{xz},\ \epsilon_{yz} = 0$) of the 4 noded 3 parameter element can be arranged in a vector form:

$$\boldsymbol{\epsilon}^T = \begin{pmatrix} \boldsymbol{\epsilon}_1 & \boldsymbol{\epsilon}_2 & \boldsymbol{\epsilon}_3 & \boldsymbol{\epsilon}_4 \end{pmatrix} \quad with \quad \boldsymbol{\epsilon}_i^T = \begin{pmatrix} \epsilon_{xx} & \epsilon_{xx} & 2\epsilon_{xy} & \epsilon_{xx} & \kappa_{xx} & \kappa_{yy} & 2\kappa_{xy} \end{pmatrix} \tag{5.43}$$

The nodal strain vector is recovered from the displacement field by applying the strain displacement matrix, which varies over the element.

$$\boldsymbol{\epsilon}(\xi,\, \eta) = \mathbf{B}(\xi,\, \eta)\mathbf{u}(\xi,\, \eta) \tag{5.44}$$

As per the DSG triangle, the strains and stresses are calculated at the Gauss points of the element, with the ANDES-DKT element having four Gauss points ($j = 1,\, 2,\, 3,\, 4$). Thus, the strain vector at each Gauss point j is recovered from the discrete nodal displacements $\hat{\mathbf{u}}_i$ as follows:

$$\boldsymbol{\epsilon}_{GP_j} = \mathbf{B}(\xi_j,\, \eta_j) \sum_{i=1}^{4\ nodes} N_i(\xi_j,\, \eta_j)\hat{\mathbf{u}}_i \tag{5.45}$$

With the strains determined, the stresses at each Gauss point are recovered with the material matrix (which in the general case may vary over the element).

$$\boldsymbol{\sigma}_{GP_j} = \mathbf{C}_{GP_j}\, \boldsymbol{\epsilon}_{GP_j} \tag{5.46}$$

The general implementation of the stress and strain recovery described above is illustrated in the following pseudocode.

Algorithm 4 ANDES-DKT quadrilateral element stress and strain recovery

Require: $requestedQuantity$, calculation of nodal displacements

call `InitializeCalculationData`$(data)$
    Calculate constant components of strain-displacement matrix B
    Retrieve element $localDisplacements$
while $gaussPoint$ < 4 **do**
    call `CalculateGaussPointContribution`$(data)$
        call `CalculateBMatrix`$(data)$
            Calculate combined B at current $gaussPoint$
    $generalizedStrains$ = product$(B,\ localDisplacements)$
    if $requestedQuantity$ requires stress **then**
        call `CalculateSectionResponse`$(data)$
        $generalizedStresses$ = product $(C,\ generalizedStrains)$
        Decimal correction of $generalizedStresses$
    end if
    Decimal correction of $generalizedStrains$
    if $requestedQuantity$ requires local orientation **then**
        Rotate $requestedQuantity$ to local orientation
    end if
    Assemble $requestedQuantity$ into $outputMatrix$
    if $requestedQuantity$ requires global orientation **then**
        Rotate $outputMatrix$ to global orientation
    end if
    Interpolate $outputMatrix$ to standard Gauss points for visualisation
end while

Chapter 6 Composite orthotropic laminates

6.1. Formulation

asdfasdf

6.2. Implementation

asdf

Chapter 7 Validation of elements

VALIDATION is as important to proper engineering analysis as the calculations performed. The following tests across statics, geometrically non-linear analysis, dynamics and quantity recovery interrogates the correct implementation of the element formulations and also gives an indication of their performance.

7.1. Static tests: shell obstacle course

Considered as the standard benchmark for shell elements, the shell obstacle course proposed by Belytschko [6] runs the elements through 3 problems involving complex loading states. These complex loading states often pose difficulties for un-enhanced elements, which is also tested here.

The *Basic-DKQ* element is a quadrilateral element with an un-enhanced membrane formulation and the DKQ bending formulation. Refer to Appendix A for full details. Any performance differences that arise between this element and the ANDES-DKQ element can be attributed to the ANDES element technology.

The *Basic-T3* element is a triangular element with an un-enhanced shear formulation and no correction to the shear component of the material matrix. Refer to Appendix B for full details. Any performance differences that arise between this element and the DSG element can be attributed to the DSG element technology.

Furthermore, context of element performance is provided by including results from the existing *KRATOS Q4* five parameter quadrilateral element (EAS-MITC formulation) and the *KRATOS T3* three parameter triangle element (ANDES-DKT formulation).

7.1.1. Scordelis-Lo roof - good

The first problem of the shell obstacle course is the Scordelis-Lo roof, which is part of a cylindrical shell fixed by rigid diaphragms at it's axial ends. The loading is a pseudo-gravity distributed load that has a magnitude of 90. Due to symmetry, only a quarter of the shell is modelled. The key result is the vertical displacement of the lateral side at the midpoint, denoted by u in the following diagram. The reference value is $u_{ref} = 0.3024$.

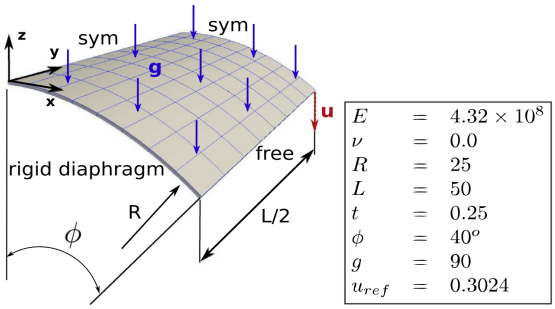

Figure 28 Definition of the Scordelis-Lo roof benchmark[13]

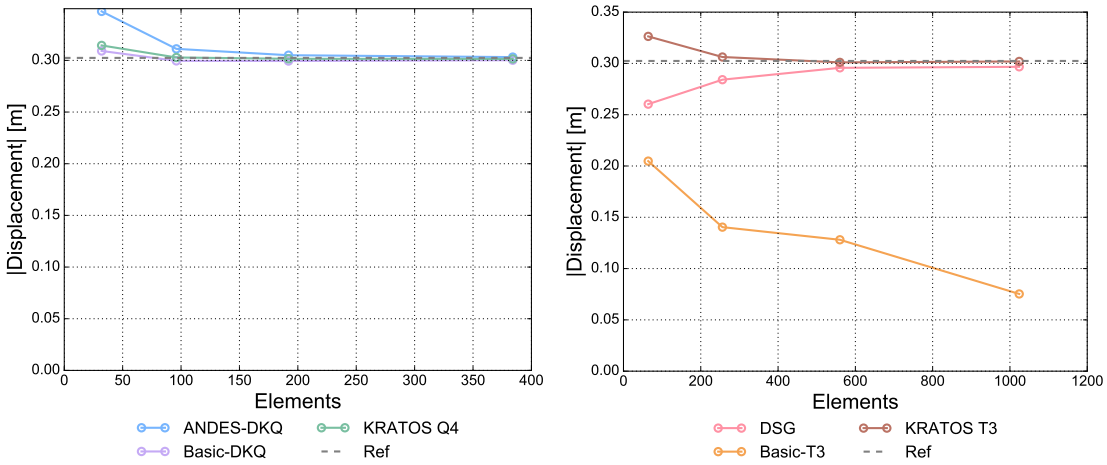

(a) Quadrilateral element convergence for the Scordelis-Lo roof benchmark

(b) Triangle element convergence for the Scordelis-Lo roof benchmark

Figure 29 Scordelis-Lo roof benchmark results

The convergence graphs above indicate the ANDES-DKQ and DSG elements agree to the reference solution. Conversely, the Basic-T3 element shows very poor performance. Given that the Basic-DKQ performs well (which is immune to transverse shear locking), it's suspected that transverse shear locking is crippling the Basic-T3 element, while the DSG element technology effectively mitigates this for the DSG element.

7.1.2. Pinched cylinder - good

The second problem of the shell obstacle course is the pinched cylinder, which considers a cylindrical shell fixed by rigid diaphragms at it's axial ends. The loading consists of two opposing compressive point loads at the centre of the shell. Due to symmetry only an eighth of the shell is modelled. The key result is the vertical displacement under the point load, denoted by u in the following diagram. The reference value is $u_{ref} = 1.8248 \times 10^{-5}$.

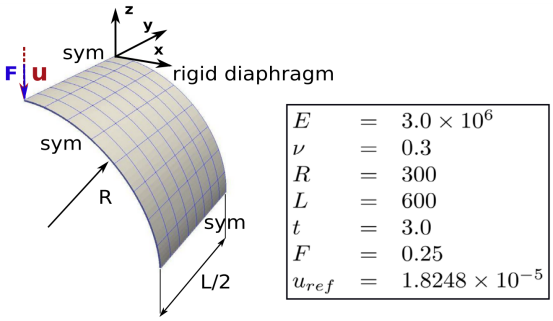

Figure 30 Definition of the pinched cylinder benchmark[13]

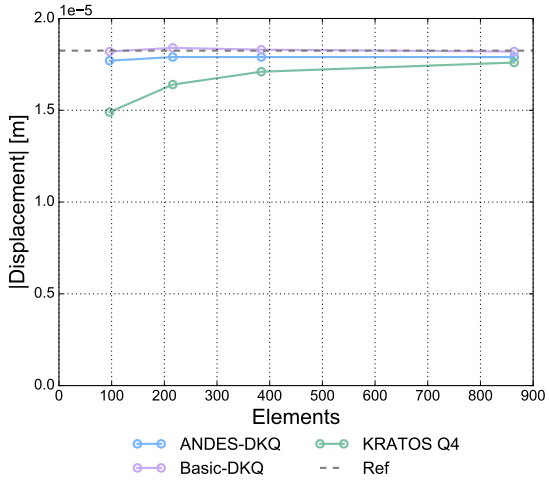

(a) Quadrilateral element convergence for the pinched cylinder benchmark

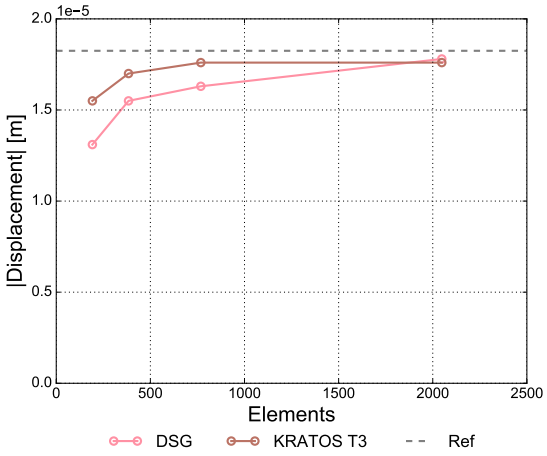

(b) Triangle element convergence for the pinched cylinder benchmark

Figure 31 Pinched cylinder benchmark results

The good performance of both the ANDES-DKQ and DSG elements is demonstrated in the convergence graphs above. The Basic-T3 results were in the order of 1×10^{-3} (roughly 100 times greater than the reference solution) and were omitted from the graph for clarity of scale. Once again, it is clear that the computationally inexpensive DSG element technology drastically improves performance from the un-enhanced Basic-T3 to the DSG element.

7.1.3. Pinched hemisphere - good

The last test in the shell obstacle course is the pinched hemisphere, which considers a hemispherical shell loaded with opposing point loads along it's equator. Due to symmetry only a quarter of the shell is modelled. The key result is the 'x' displacement along one of the point loads, denoted by u in the following diagram. The reference value is $u_{ref} = 0.0924$.

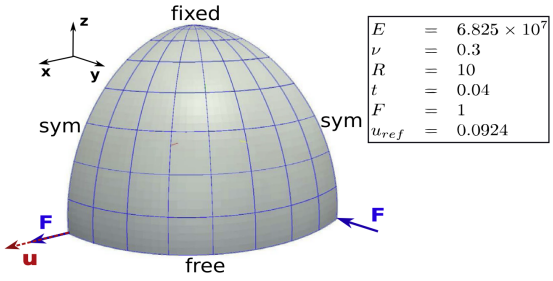

Figure 32 Definition of the pinched hemisphere benchmark [13]

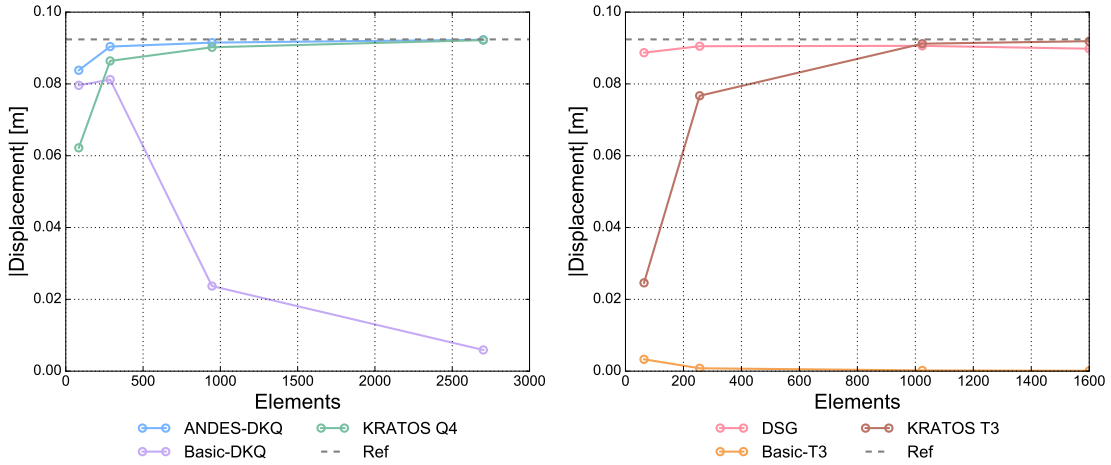

(a) Quadrilateral element convergence for the pinched hemisphere benchmark

(b) Triangle element convergence for the pinched hemisphere benchmark

Figure 33 Pinched hemisphere benchmark results

The ANDES-DKQ and DSG elements both perform well in the final statics test, as per the convergence graphs above. It is observed that the Basic-DKQ element appears to exhibit membrane locking corresponding to the high double curvature of the problem ($R_1 = R_2 = 10$) compared to the Scordelis-Lo roof ($R_1 = 10,\ R_2 = \infty$) and the pinched cylinder ($R_1 = 300,\ R_2 = \infty$). The ANDES element technology clearly prevents this deleterious effect. The poor performance of the Basic-T3 element compared to the DSG element once again highlights the effectiveness of the DSG element technology in preventing transverse shear locking.

7.2. Geometically non-linear tests

Large rotations and displacements mark the departure from geometrically linear to non-linear analyses, however, the assumption of small strains is still maintained. The extension of the elements to geometrically non-linear problems is handled by employing an existing Kratos class which provides co-rotational transformations for shells. At each increment in the non-linear solution, the large displacements and rotations of each element is mapped by rigid body translations and rotations, thus limiting the strains experienced by the element to reasonably small magnitudes. The performance of the element in geometrically non-linear problems is considered with two benchmarks.

7.2.1. Hinged cylindrical roof - good

The first geometrically non-linear benchmark is the snap-through of a hinged cylindrical roof under a central point load $P_{max} = 3000$ [40]. As per the diagram below, the roof geometry is defined with the parameters: $L = 254,\ R = 2540,\ \theta = 0.1\ rad$ and $t = 12.7$. The material is defined with a Young's modulus $E = 3102.75$ and Poisson's ratio of $\nu = 0.3$.

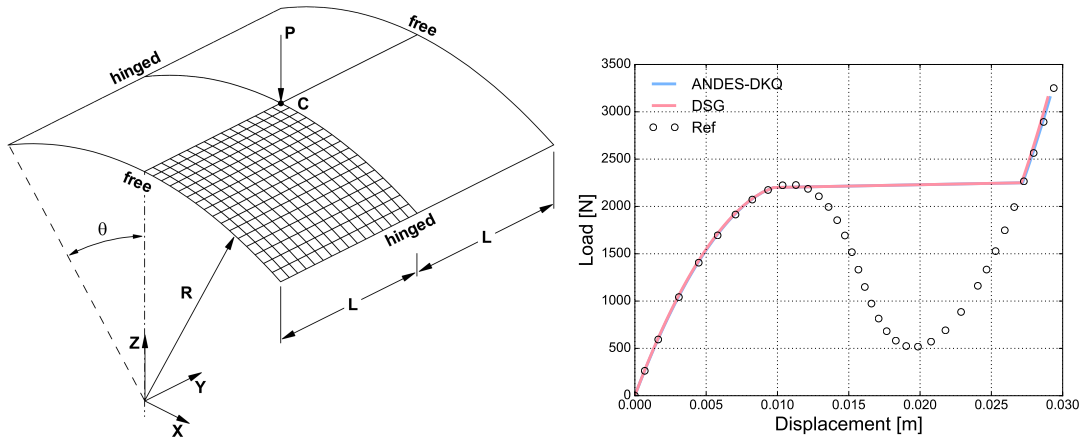

(a) Hinged cylindrical roof definition [40]

(b) Load-displacement curve of hinged cylindrical roof

Figure 34 Hinged cylindrical roof benchmark

The load displacement curve plots the equilibrium path for the ANDES-DKQ and DSG elements against the reference path from [40]. The full equilibrium path isn't resolved because Kratos only has a load control non-linear solution method implemented, translating to the restriction of only resolving monotonically increasing paths. Regardless, both elements clearly follow the initial path, and then rejoin the reference solution to correctly resolve the structure in it's snapped-through state.

7.2.2. Open cylinder pull-out - good

The second geometrically non-linear benchmark is the pull-out of an open cylinder with a load $P_{max} = 40\ 000$. The geometry of the cylinder is $L = 10.35,\ R = 4.953$ and $t = 0.094$ while the linear elastic material is characterised by $E = 10.5 \times 10^6$ and $\nu = 0.3125$. The measured displacement is the vertical deformation u_z at the point of load application.

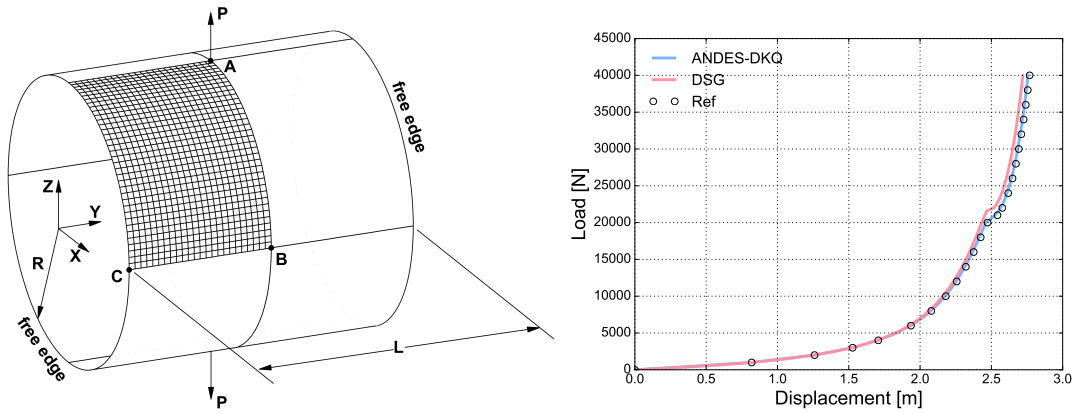

(a) Open cylinder pullout definition [40]

(b) Load-displacement curve of open cylinder pullout

Figure 35 Open cylinder pullout benchmark

The load-displacement curve above plots the equilibrium path for the ANDES-DKQ and DSG elements against the reference solution [40]. Although both elements closely follow the reference path, the ANDES-DKQ performs better in this test than the DSG element. Despite this, the error of the DSG element at maximum load is still only 1.7%.

7.3. Dynamic tests

Dynamic problems introduce inertial effects into the array of phenomena analysed. Combined with the aforementioned co-rotational formulation, it is possible to accurately resolve bodies undergoing large movements over time.

7.3.1. Shell pendulum - good

The first dynamic benchmark is a simple shell pendulum allowed to freely rotate along one hinged edge. The initial horizontal configuration of the $1m \times 1m \times 0.1m$ thick square plate is subject to gravity $g = 9.8\ m/s^2$ acting in the vertical Z direction. The material of the plate is described by $E = 1 \times 10^9 Pa,\ \nu = 0.0$ and $\rho = 7850 kg/m^3$. The key result is the vertical displacement component of the free corner node as drawn below.

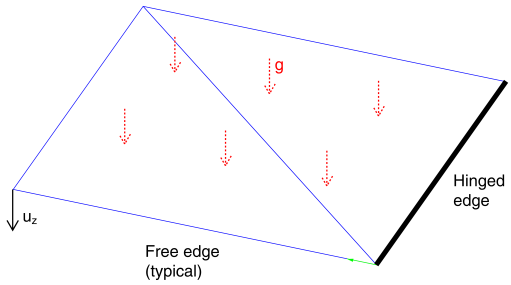

Figure 36 Shell pendulum definition

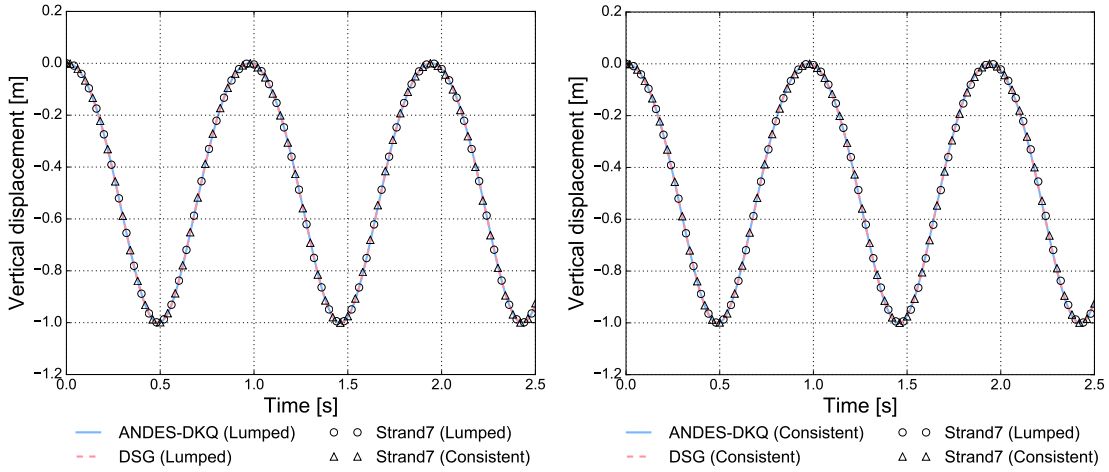

(a) Results using lumped mass matrices

(b) Results using consistent mass matrices

Figure 37 Vertical displacement over time of the shell pendulum analysis

The plot of displacement over time demonstrates the ability of both elements to handle large displacements and rotations, agreeing with the reference solution of the existing Kratos quadrilateral shell element. As expected, the minimum vertical displacement of $u_z = -1m$ corresponds to the position of bottom dead centre of the plate, while the maximum vertical displacement of $u_z = 0m$ corresponds to a fully horizontal plate orientation

7.3.2. Oscillating clamped plate - good

The oscillating clamped plate benchmark subjects a clamped cantilever square plate $2m \times 2m \times 0.1m$ thick to a uniform globally oriented surface pressure of $P_z = -0.25Pa$. The plate material is linear elastic characterised by $E = 1 \times 10^6 Pa$, $\nu = 0.0$ and $\rho = 7850kg/m^3$. The key result is the vertical displacement component of the free corner node as illustrated below.

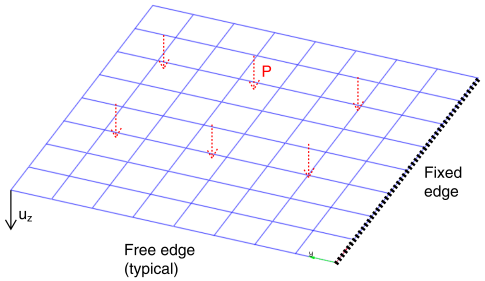

Figure 38 Oscillating clamped plate definition

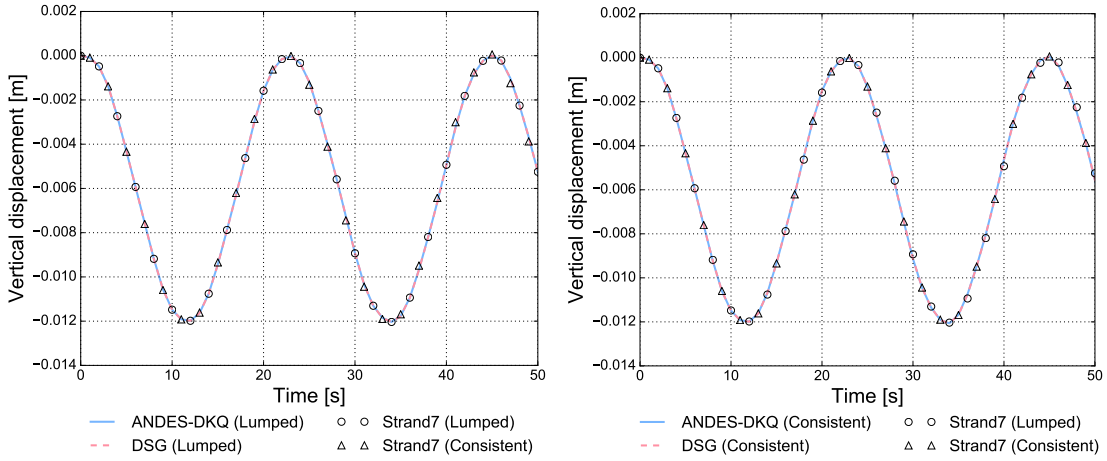

(a) Results using lumped mass matrices

(b) Results using consistent mass matrices

Figure 39 Vertical displacement over time of the oscillating clamped plate analysis

The plot of vertical displacement over time demonstrates both elements agree with the reference solution, which is the existing Kratos quadrilateral element. The overall results correctly correspond to structural dynamics theory by oscillating with the base natural frequency about the static displacement of $u_z = -0.006m$.

7.4. Quantity recovery tests

Write something about recovery of shell resultants, stresses and strains are important.

7.4.1. Simply supported dome with oculus under self weight - done

Meshes were all roughly 3000 elements.

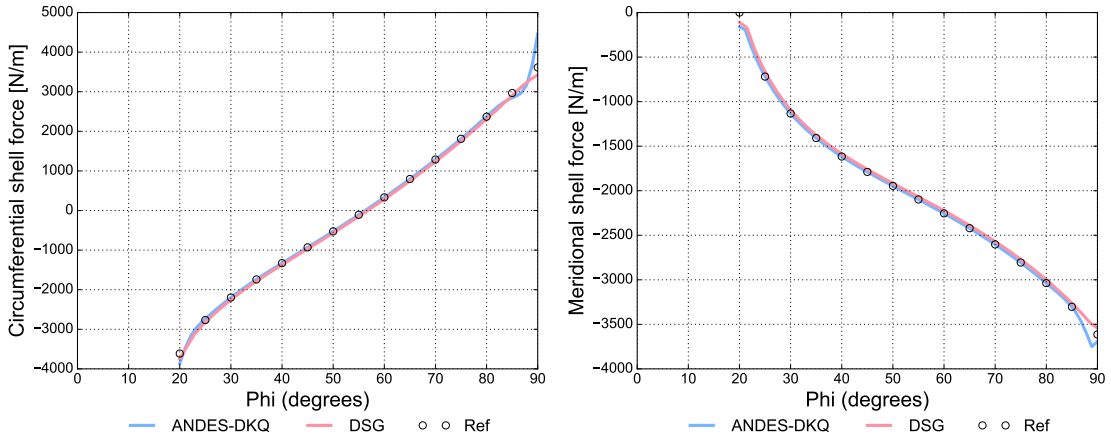

(a) Circumferential shell force over meridian angle

(b) Meridional shell force over meridian angle

Figure 40 Shell forces of the simply supported dome analysis

Ref is shell membrane theory!

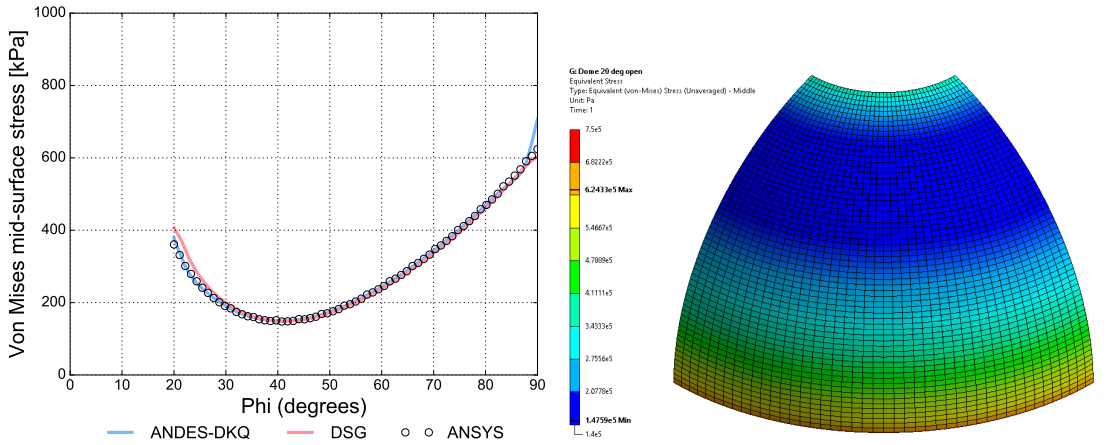

(a) Mid-plane Von Mises stress over meridian angle

(b) Mid-plane Von Mises plot of the reference ANSYS solution

Figure 41 Mid-plane Von Mises stress results of the simply supported dome analysis

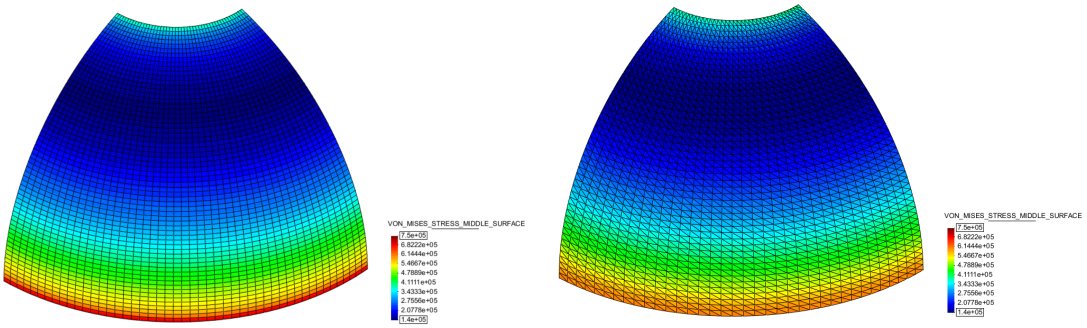

(a) Mid-plane Von Mises plot of the ANDES solution

(b) Mid-plane Von Mises plot of the DSG solution

Figure 42 Mid-plane Von Mises stress plots of the simply supported dome analysis

limits all set to [1.4e5, 7.5e5] !!!!!!

7.4.2. Navier supported plate under sinusoidal load

200x200x10, E=2e11, Poisson = 0.3, pressure = -1e7.

Ref is classical solution as per Reddy [38]. Refer to D.

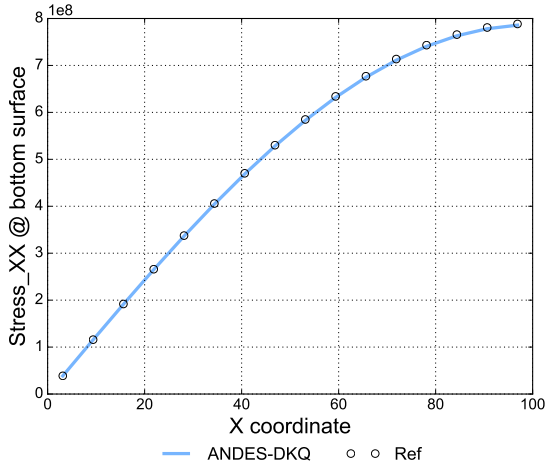

(a) Normal stress (XX) over X coordinate

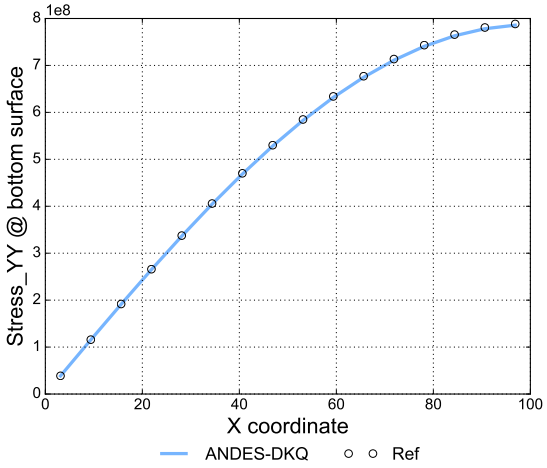

(b) Normal stress (YY) over X coordinate

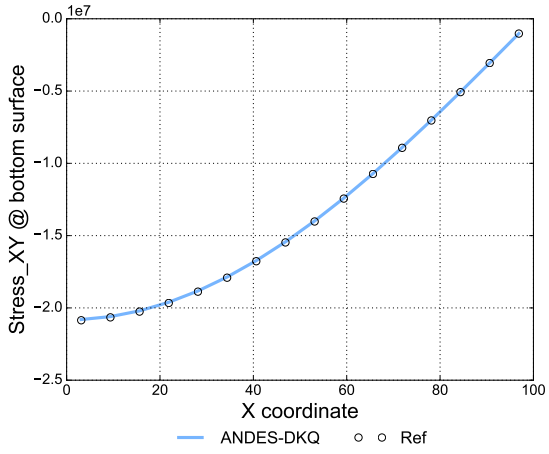

(c) Shear stress (XY) over X coordinate

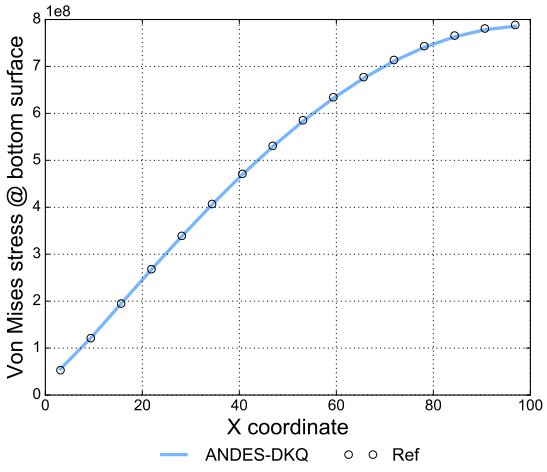

(d) Von Mises stress over X coordinate

Figure 43 Stresses (bottom surface) of the Navier supported plate under sinusoidal load

asdfadsf

7.4.3. Navier supported plate under uniformly distributed load

200x200x10, E=2e11, Poisson = 0.3, pressure = -1e7. Navier edge along y axis had phiX = 0, while navier edge along x axis had phiY = 0.

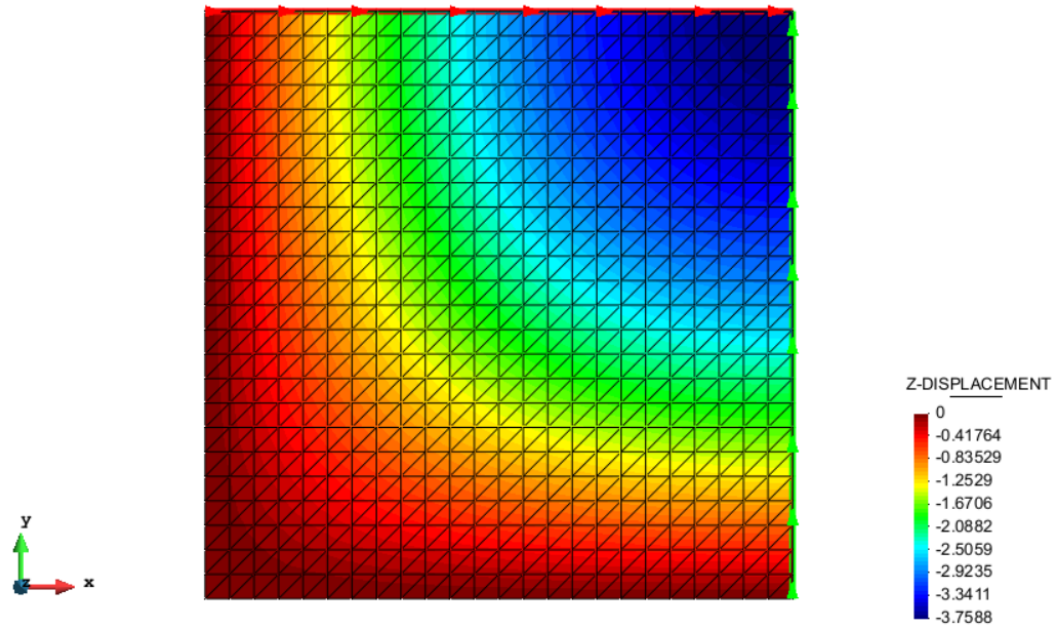

Figure 44 Paths for results: Red = X path and Green = Y path

Ref is ANSYS solution!

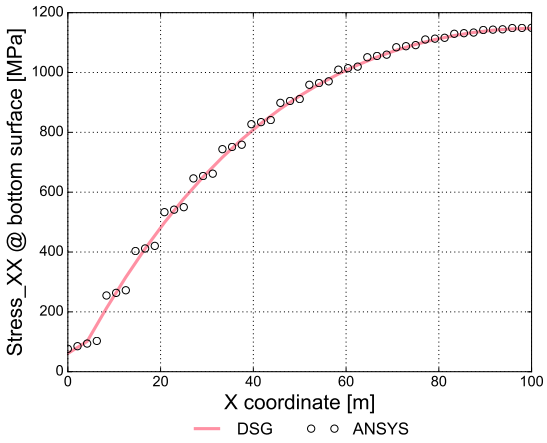

(a) Normal stress (XX) over X coordinate

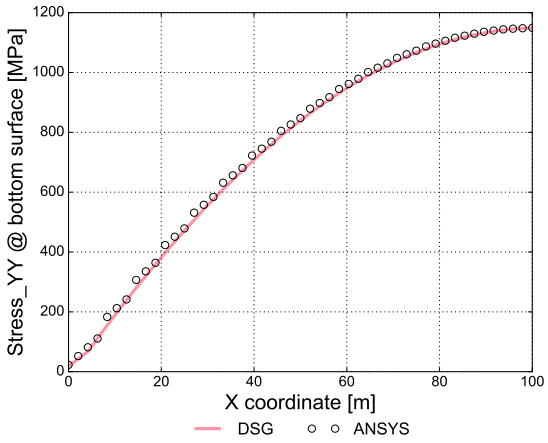

(b) Normal stress (YY) over X coordinate

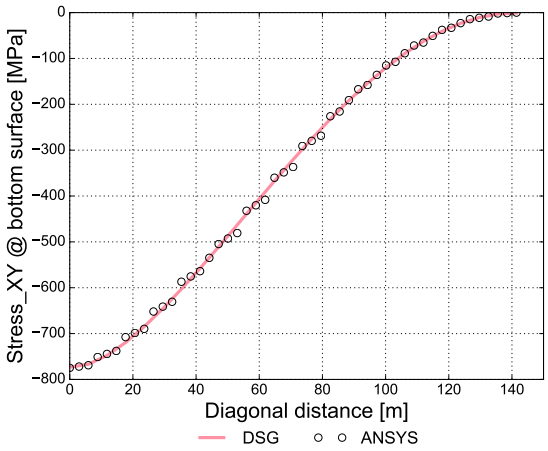

(c) In plane shear stress (XY) over plate diagonal

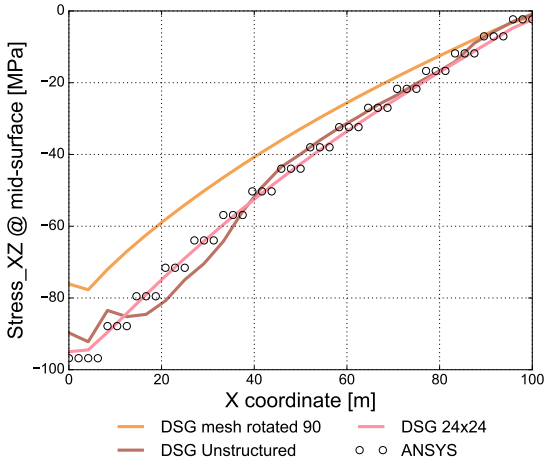

(d) Transverse shear stress (XZ) over X coordinate

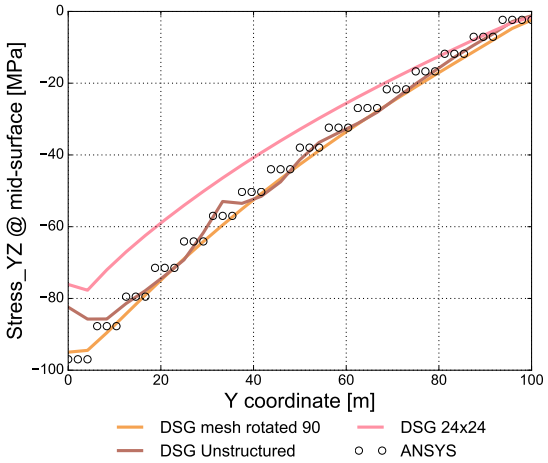

(e) Transverse shear stress (YZ) over Y coordinate

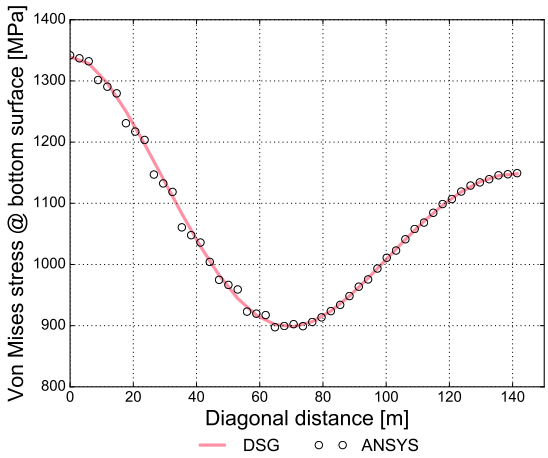

(f) Von Mises stress over plate diagonal

Figure 45 Stresses of the Navier supported plate under uniformly distributed load

asdfadsf

7.5. Composite tests

asdfadsf

7.5.1. Composite linear statics: composite barrel vault

asdfdsf

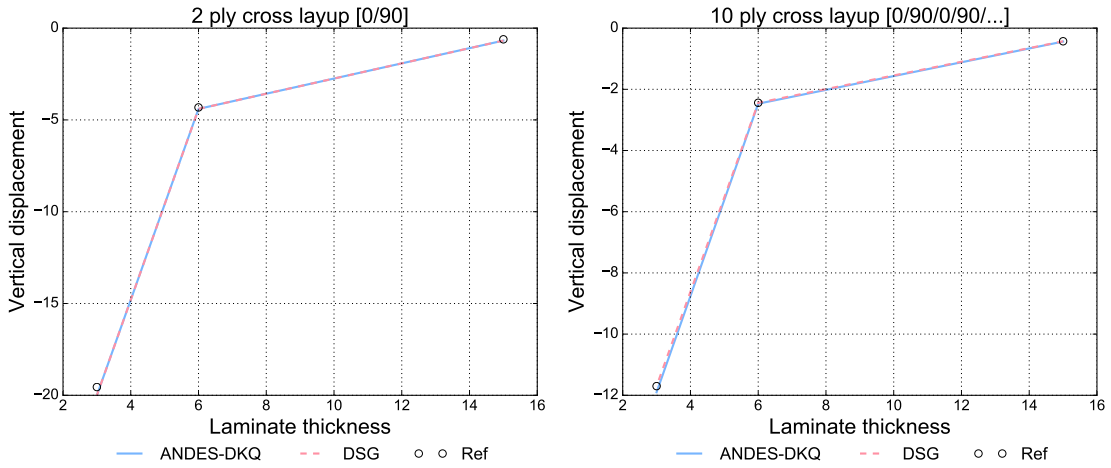

(a) 2 ply cross layup

(b) 10 ply cross layup

Figure 46 Composite barrel vault benchmark: cross layup

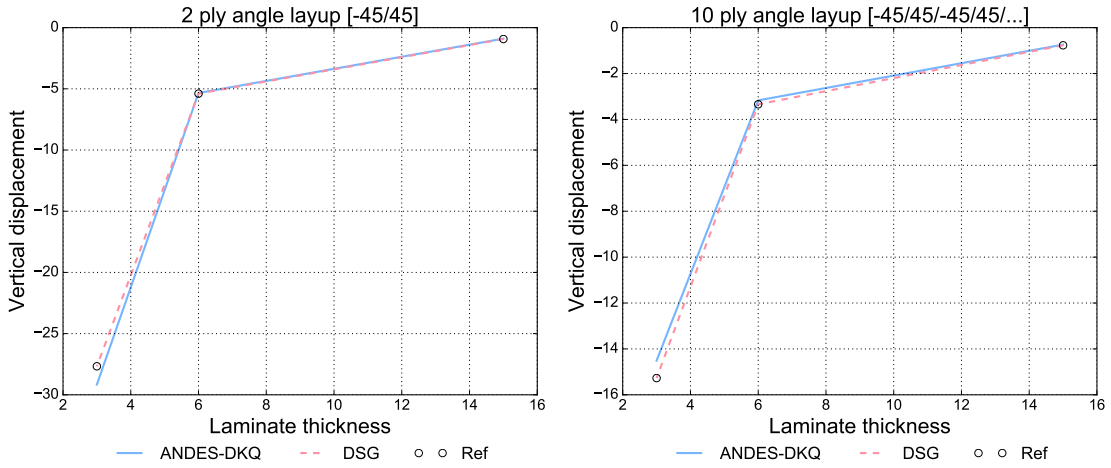

(a) 2 ply angle layup

(b) 10 ply angle layup

Figure 47 Composite barrel vault benchmark: angle layup

reference solution is [38].

asdfad

7.5.2. Composite linear static: clamped cylinder

asdfdsf

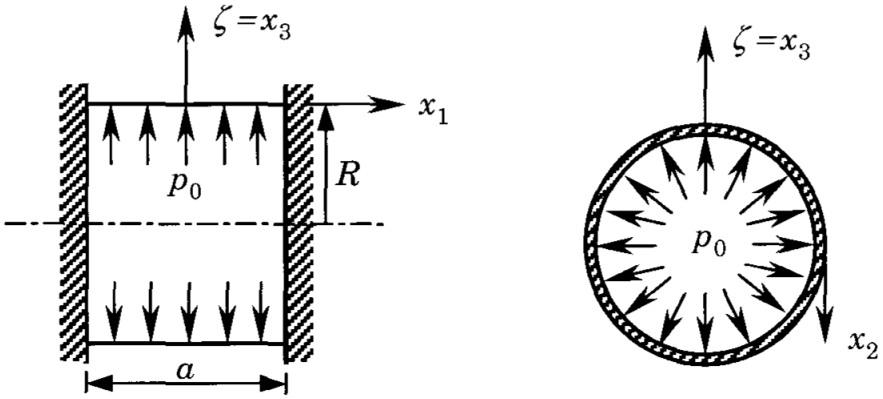

Figure 48 Composite clamped cylinder test definition

asdfasdf

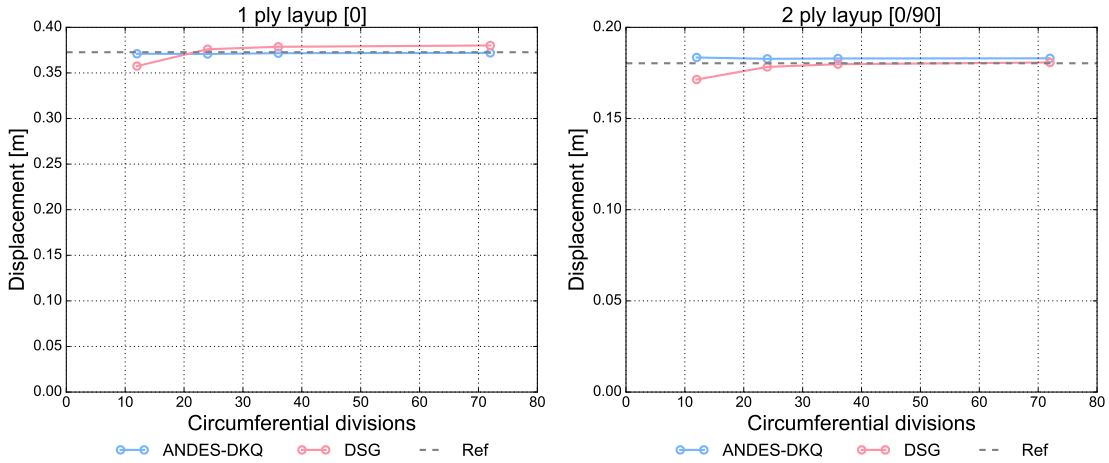

(a) 1 ply layup

(b) 2 ply layup

Figure 49 Composite clamped cylinder analysis convergence

asdfadsf

7.5.3. Composite non-linear static: composite hinged cylindrical roof - update graph

asdfdsf

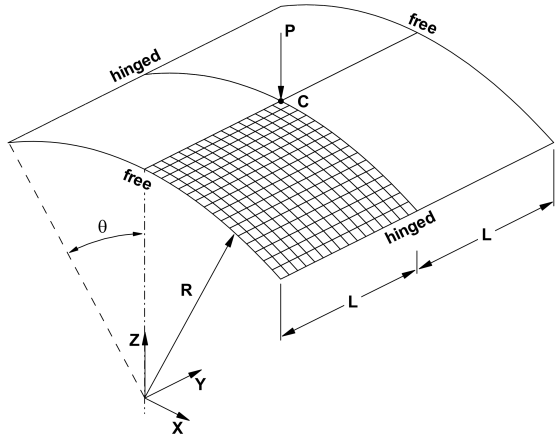

(a) Composite hinged cylindrical roof definition [40]

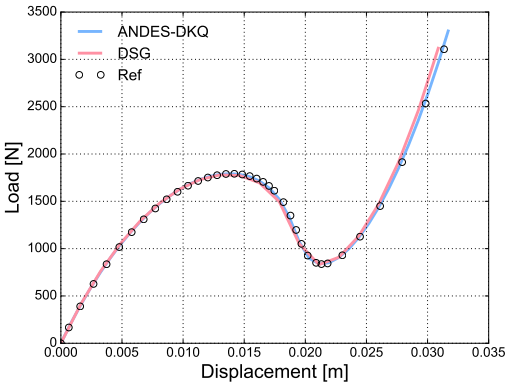

(b) Load-displacement curve of composite hinged cylindrical roof

Figure 50 Composite hinged cylindrical roof benchmark

asdsds

7.5.4. Composite dynamics: shell pendulum - good

asdfdsf

swinging plate material setup:

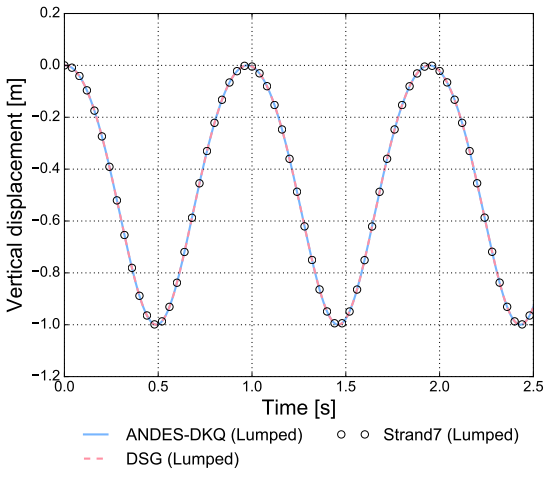

(a) Vertical displacement over time for composite shell pendulum analysis

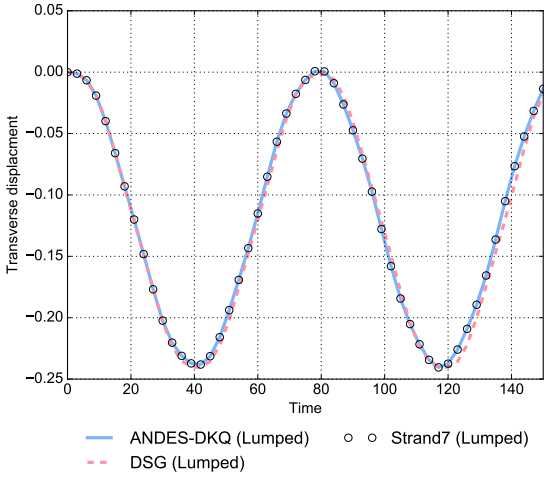

(b) Vertical displacement over time for composite oscillating clamped plate benchmark

Figure 51 Composite dynamic benchmarks

vibrating square material setup:

7.5.5. Composite stress recovery: laminate tensile test

Example from Nasa composite doc, example 3. Tensile test token was 10x2x0.02 total thickness. Layup was [0,45,45,0].

Reference tsai-wu results are "Modified tsai-wu" of the same problem on Strand7 FEA software.

Material was :

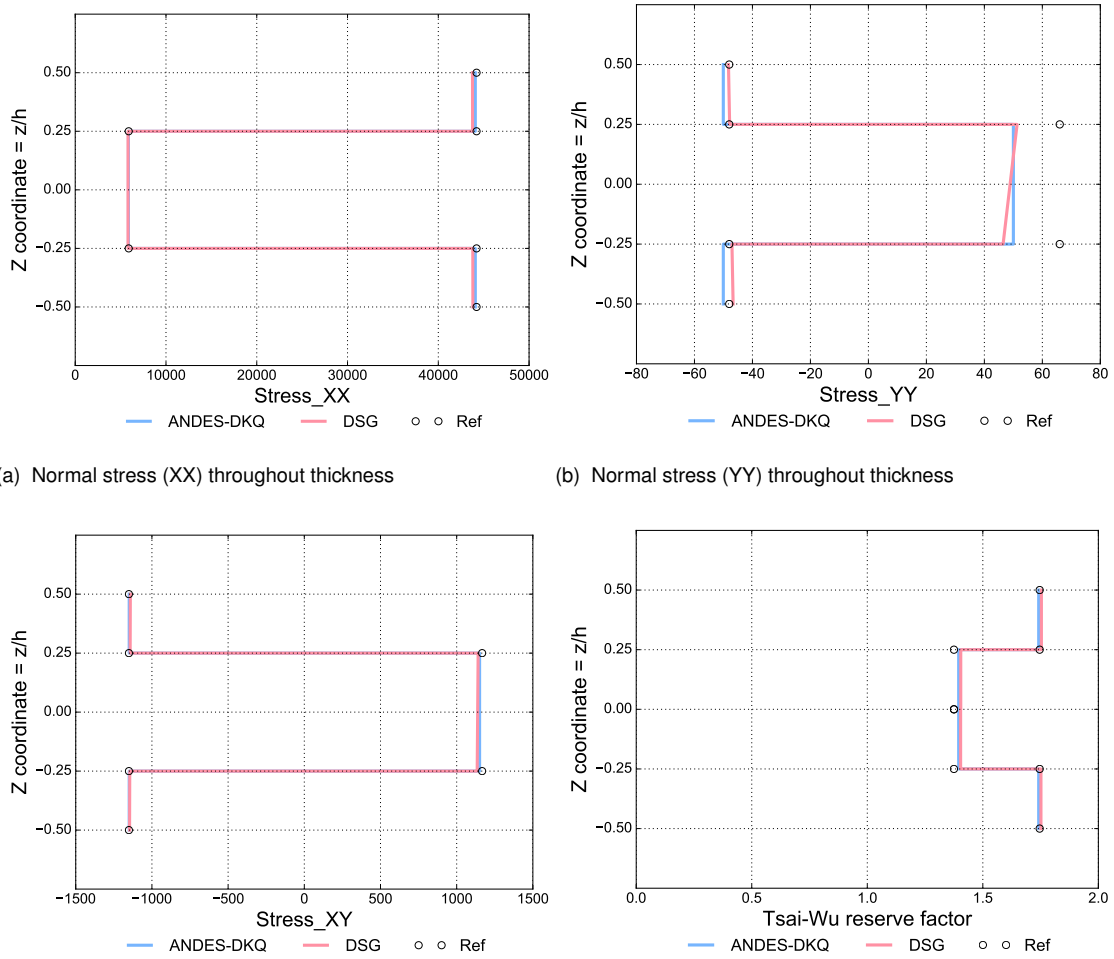

(a) Normal stress (XX) throughout thickness

(b) Normal stress (YY) throughout thickness

(c) In plane shear stress strain (XY) throughout thickness

(d) Tsai-Wu reserve factor throughout thickness

Figure 52 Stresses and Tsai-Wu results of the composite tensile test

asdfdsf

7.5.6. Composite stress recovery: Navier supported laminate under sinusoidal load

Ref is Reddy p527 table 9.3.2. 200x200x10 total thickness.

Thin plate referred to classical plate theory solution. Thick plate referred to CFS analytical solution.

asdfdsf

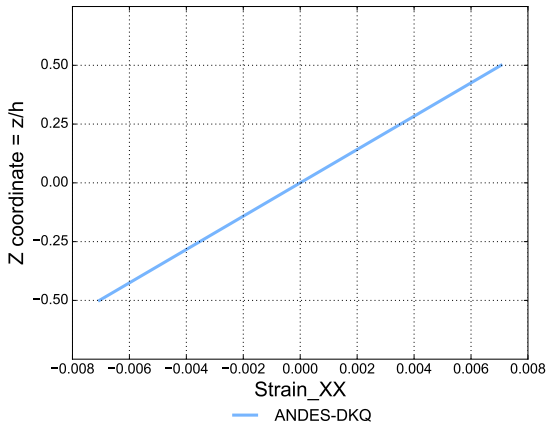

(a) Normal strain (XX) throughout thickness

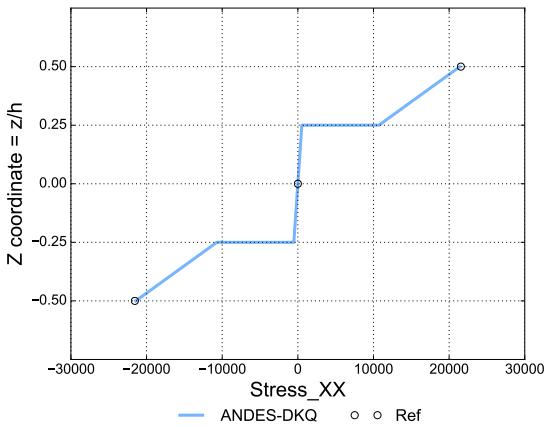

(b) Normal stress (XX) throughout thickness

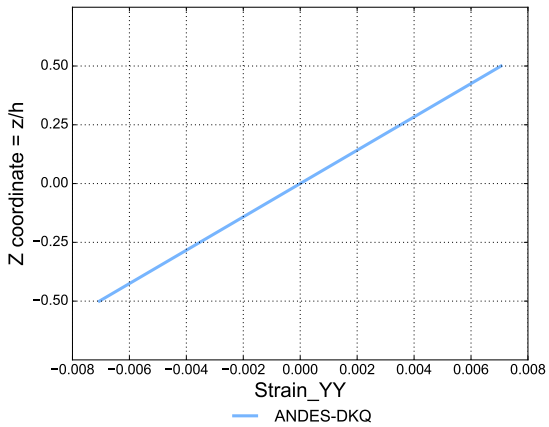

(c) Normal strain (YY) throughout thickness

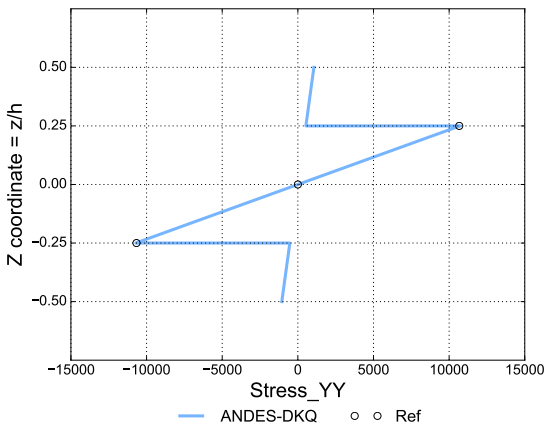

(d) Normal stress (YY) throughout thickness

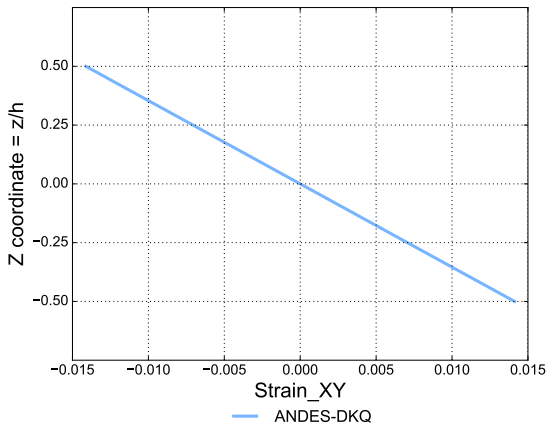

(e) In plane shear strain (XY) throughout thickness

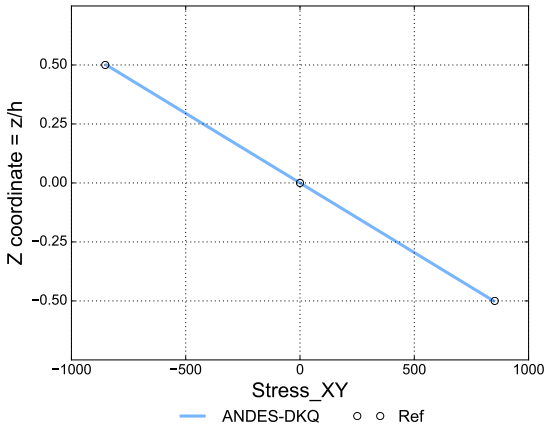

(f) In plane shear stress (XY) throughout thickness

Figure 53 Stresses and strains of the Navier supported ANDES-DKQ laminate under a sinusoidally distributed load

asdfadsf

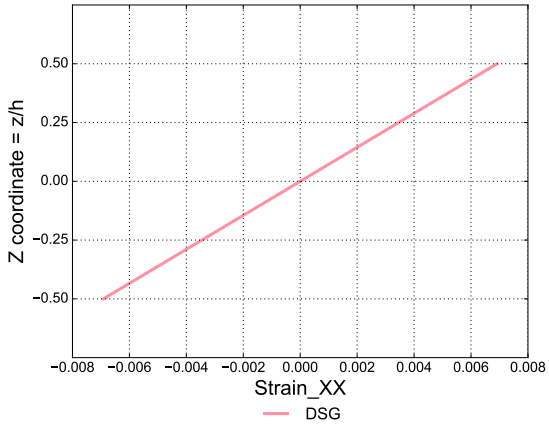

(a) Normal strain (XX) throughout thickness

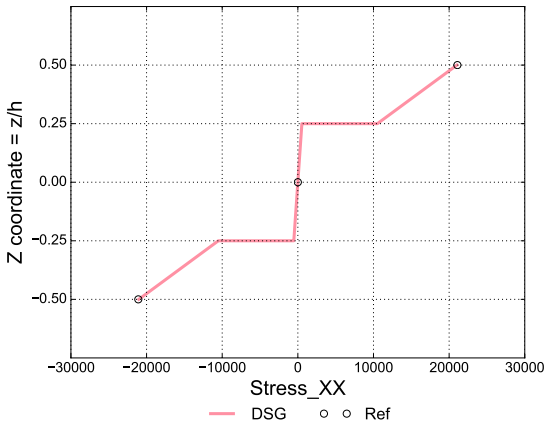

(b) Normal stress (XX) throughout thickness

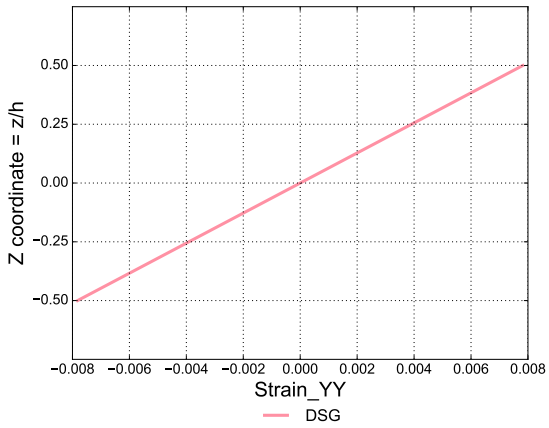

(c) Normal strain (YY) throughout thickness

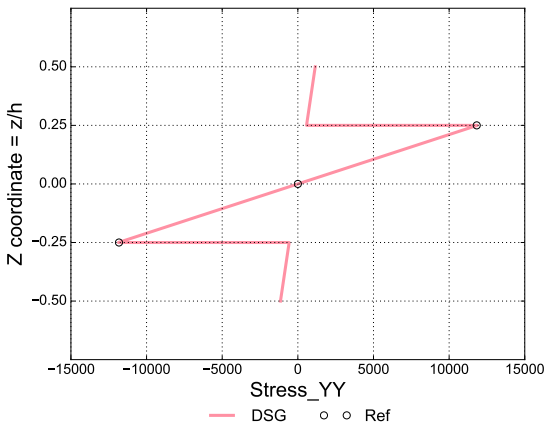

(d) Normal stress (YY) throughout thickness

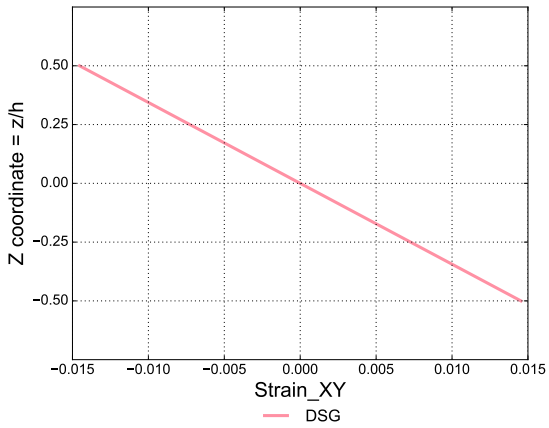

(e) In plane shear strain (XY) throughout thickness

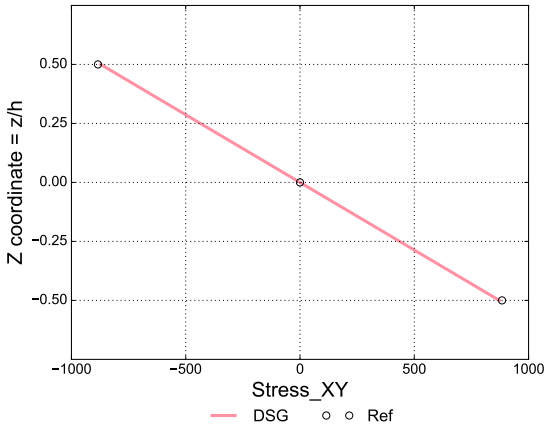

(f) In plane shear stress (XY) throughout thickness

Figure 54 In plane stresses and strains of the Navier supported DSG laminate under a sinusoidally distributed load

asdfadsf

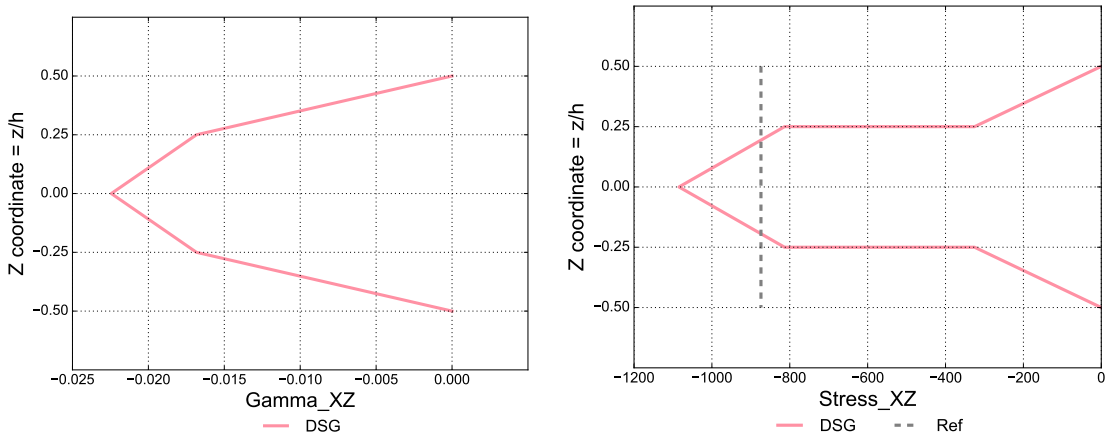

(a) Transverse shear strain (XZ) throughout thickness

(b) Transverse shear stress (XZ) throughout thickness

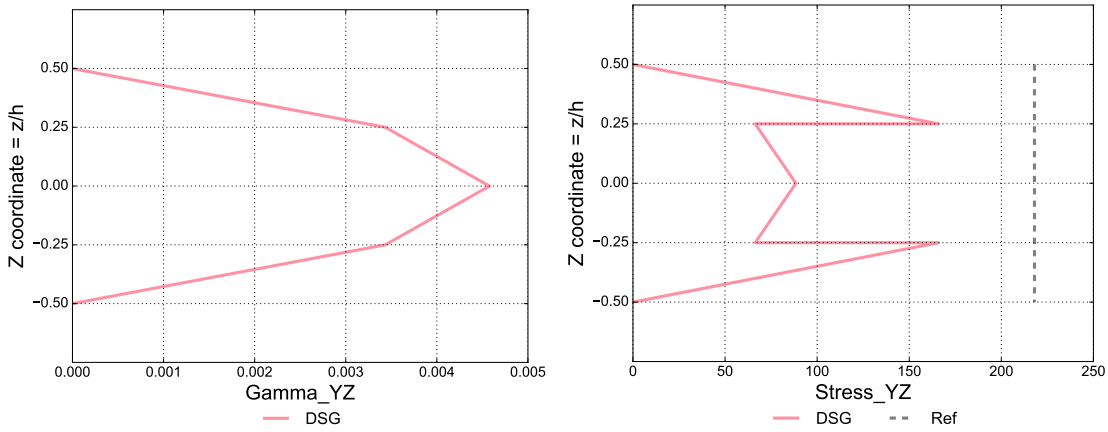

(c) Transverse shear strain (YZ) throughout thickness

(d) Transverse shear stress (YZ) throughout thickness

Figure 55 Transverse shear stresses and strains of the Navier supported DSG laminate under a sinusoidally distributed load

INVESTIGATE WHY THE TRANSVERSE STRESSES ARE DIFFERENT HERE!

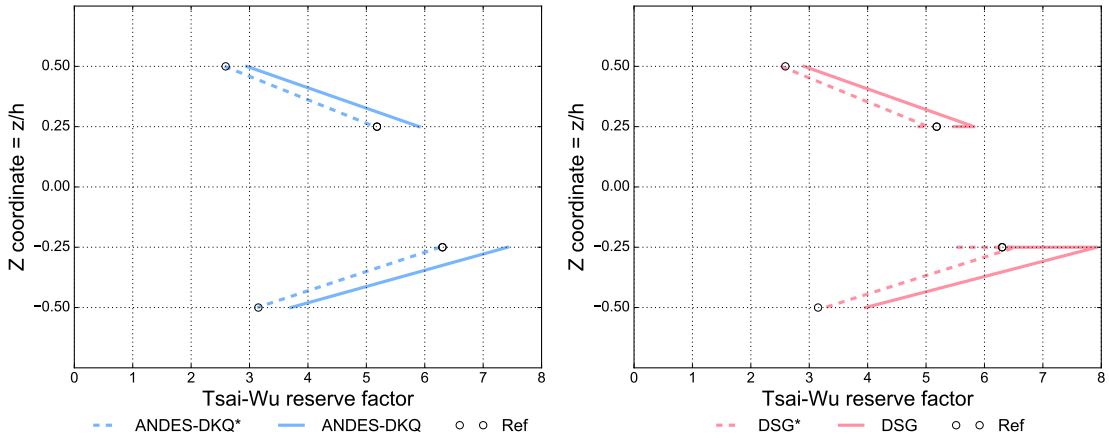

(a) Tsai-Wu reserve factor throughout thickness of ANDES-DKQ element

(b) Tsai-Wu reserve factor throughout thickness of DSG element

Figure 56 Tsai-Wu reserve factor through the thickness of the Navier supported DSG laminate under a sinusoidally distributed load

* indicates the in-plane interaction coefficient of the Tsai-Wu criterion was disabled, as per the internal calculations of Strand7 FEA software.

Tsai-Wu result is discontinuous because the thin shell has no stress on the mid-plane under pure bending, yielding an infinite reserve factor. Contrasting this, the prescence of transverse shear stresses on the mid-plane in the DSG element yields a finite reserve factor of roughly 100, which has been omitted for clarity.

asdfasdf

Chapter 8 Conclusions and Outlook

This work has considered the implementation of a thin quadrilateral shell element for the multiphysics code KRATOS. Section 1 covered the shell formulation, which is split into membrane and bending components. Following this, the element's implementation in KRATOS was presented, which covered key methods employed and the general workflow to calculate the element stiffness matrix. The element considered was subjected to the well known shell obstacle course in Section 3. Although the element correctly converged to the reference solution for the Scordelis-Lo roof and Pinched Cylinder problem, the Pinched Hemisphere benchmark revealed element deficiencies. These deficiencies were identified, with informed direction suggested for future work associated with improving this element.

8.1. Future work

Extend shell elements model into a variety of directions:

- Consider von karman non-linear strains for very thin shells

- Improve transverse shear stress modelling for composites Look at paper: Improved Transverse Shear Stresses in Composite Finite Elements based on First Order Shear Deformation Theory Or, develop separate element with higher order resolving theory

Appendix A **Basic-DKQ formulation**

Introduced in section 7.1, the Basic-DKQ quadrilateral element represents the ANDES-DKQ formulation with the membrane ANDES element technology replaced with an un-enhanced displacement based membrane formulation. The DKQ bending formulation is used as per section 5.1.2.

The membrane stiffness of the Basic-DKQ formulation is purely displacement based and employs the standard bi-linear quadrilateral shape functions:

$$\begin{aligned} N_1(\xi,\eta) &= \frac{1}{4}(1-\xi)(1-\eta) \\ N_2(\xi,\eta) &= \frac{1}{4}(1+\xi)(1-\eta) \\ N_3(\xi,\eta) &= \frac{1}{4}(1+\xi)(1+\eta) \\ N_4(\xi,\eta) &= \frac{1}{4}(1-\xi)(1+\eta) \end{aligned} \tag{A.1}$$

The membrane strains are related to the discrete in-plane membrane displacements $\hat{\mathbf{v}}$ via the differential operator $\mathbf{L}$ and the aforementioned shape functions $\mathbf{N}$ as such:

$$\boldsymbol{\epsilon} = \mathbf{LN}\hat{\mathbf{v}} = \mathbf{B}\hat{\mathbf{v}} \quad with \quad \hat{\mathbf{v}} = \begin{pmatrix} \hat{\mathbf{v}}_1 \\ \hat{\mathbf{v}}_2 \\ \hat{\mathbf{v}}_3 \\ \hat{\mathbf{v}}_4 \end{pmatrix} \quad and \quad \hat{\mathbf{v}}_i = \begin{pmatrix} \hat{v}_{xi} \\ \hat{v}_{yi} \end{pmatrix} \tag{A.2}$$

The differential operator is defined as:

$$\mathbf{L} = \begin{pmatrix} \frac{\partial}{\partial x} & 0 \\ 0 & \frac{\partial}{\partial y} \\ \frac{\partial}{\partial y} & \frac{\partial}{\partial x} \end{pmatrix} \tag{A.3}$$

The matrix of shape functions is structured as follows:

$$\mathbf{N} = \begin{pmatrix} \mathbf{N}_1 & \mathbf{N}_2 & \mathbf{N}_3 & \mathbf{N}_4 \end{pmatrix} \quad with \quad \mathbf{N}_i = \begin{pmatrix} N_i & 0 \\ 0 & N_i \end{pmatrix} \tag{A.4}$$

The basic membrane strain displacement matrix $\mathbf{B}$ is thus:

$$\mathbf{B} = \mathbf{LN} = \begin{pmatrix} \mathbf{B}_1 & \mathbf{B}_2 & \mathbf{B}_3 & \mathbf{B}_4 \end{pmatrix} \quad with \quad \mathbf{B}_i = \begin{pmatrix} N_{i,x} & 0 \\ 0 & N_{i,y} \\ N_{i,y} & N_{i,x} \end{pmatrix} \tag{A.5}$$

The entries of which can be calculated with the help of the Jacobian $\mathbf{J}$:

$$\mathbf{J} = \begin{pmatrix} \frac{\partial x}{\partial \xi} & \frac{\partial y}{\partial \xi} \\ \frac{\partial x}{\partial \eta} & \frac{\partial y}{\partial \eta} \end{pmatrix} \tag{A.6}$$

$$\mathbf{J}^{-1} \begin{pmatrix} N_{1,\xi} & N_{2,\xi} & N_{3,\xi} & N_{4,\xi} \\ N_{1,\eta} & N_{2,\eta} & N_{3,\eta} & N_{4,\eta} \end{pmatrix} = \begin{pmatrix} N_{1,x} & N_{2,x} & N_{3,x} & N_{4,x} \\ N_{1,y} & N_{2,y} & N_{3,y} & N_{4,y} \end{pmatrix} \tag{A.7}$$

The above strain displacement matrix doesn't cover drilling stiffnesses, so an artificial drilling stiffness as per the DSG element formulation equation 4.14 was added for each node after the construction of the element stiffness matrix:

$$K_{\beta_z} = \frac{max(K_{ij}\delta_{ij})}{1000} \tag{A.8}$$

Appendix B **Basic-T3 formulation**

Introduced in section 7.1, the Basic-T3 quadrilateral element corresponds to a basic constant strain triangle element without any DSG enhancements. It shares the same membrane and bending strain displacement matrices as the DSG triangle element (refer equations 4.6 and 4.8), but has a different transverse shear make-up and no correction of the material matrix (as per equation 4.13).

The transverse shear stiffness of the Basic-T3 formulation is purely displacement based and employs the standard linear triangle shape functions as per the DSG element, repeated here:

$$\begin{aligned} N_1(x,y) &= \frac{1}{2A}\left[(x_2y_3 - x_3y_2) + x(y_2 - y_3) + y(x_3 - x_2)\right] \\ N_2(x,y) &= \frac{1}{2A}\left[(x_3y_1 - x_1y_3) + x(y_3 - y_1) + y(x_1 - x_3)\right] \\ N_3(x,y) &= \frac{1}{2A}\left[(x_1y_2 - x_2y_1) + x(y_1 - y_2) + y(x_2 - x_1)\right] \end{aligned} \tag{B.1}$$

The transverse shear strains are related to the derivative of the discrete transverse displacements v_{zi} and the value of nodal rotations β_{xi} and β_{yi} via the following transverse shear strain displacement matrix arrangement:

$$\boldsymbol{\gamma} = (\nabla \mathbf{N}^{v_{zi}} + \mathbf{N}^{\beta})\hat{\mathbf{v}} = \mathbf{B}\hat{\mathbf{v}} = \begin{pmatrix} \mathbf{B}_1 & \mathbf{B}_2 & \mathbf{B}_3 \end{pmatrix} \begin{pmatrix} \hat{\mathbf{v}}_1 \\ \hat{\mathbf{v}}_2 \\ \hat{\mathbf{v}}_3 \end{pmatrix} \tag{B.2}$$

The entries of $\mathbf{B}_i$ and $\hat{\mathbf{v}}_i$ are clarified:

$$\mathbf{B}_i = \begin{pmatrix} N_{i,x} & N_i & 0 \\ N_{i,y} & 0 & N_i \end{pmatrix} \quad and \quad \hat{\mathbf{v}}_i = \begin{pmatrix} \hat{v}_{zi} \\ \hat{\beta}_{xi} \\ \hat{\beta}_{yi} \end{pmatrix} \tag{B.3}$$

Appendix C Analytical membrane analysis of dome

sdfasdfasdf

Appendix D Analytical solution of Navier supported plate

sdfasdfasdf

List of Figures

1 Dimensional reduction of a solid to a shell . . . 3
2 Various shell models . . . 4
3 Deformation, reference and current configuration . . . 4
4 Kirchhoff-Love shell kinematics . . . 6
5 Reissner-Mindlin shell kinematics . . . 9
6 Eigenvalue spectra of various shell models . . . 11
7 Convergence of cylindrical shell problem demonstrating membrane locking . . . 13
8 Reduced integration of a 5 parameter Quad 4 shell . . . 14
9 Assumed shear strain field of the MITC4 element . . . 15
10 Discrete Shear Gap (DSG) concept . . . 16
11 DKQ DOF arrangement and geometry . . . 16
12 Shell assembly benefitting from drilling DOFs . . . 18
13 Material composition of the Boeing 787 . . . 21
14 Components of composite laminates . . . 22
15 Lamina in a plane stress state . . . 24
16 Continuous unidirectional fibre lamina arrangement . . . 25
17 Arbitrary orientation of lamina . . . 26
18 Force and moment resultants of a plate . . . 28
19 Coordinate system and lamina numbering in a laminate . . . 29
20 Deformation of 3 parameter plate . . . 31
21 Stress and strain thickness distribution of 4 ply plate subject to pure bending . . . 34
22 High level overview of DSG element workflow . . . 39
23 ANDES membrane nodal strain gauges . . . 49
24 Geometric dimensions of the quadrilateral element . . . 49
25 Higher order torsional mode of ANDES membrane formulation . . . 50
26 DKQ DOF arrangement and geometry . . . 53
27 High level overview of ANDES-DKQ element workflow . . . 58
28 Definition of the Scordelis-Lo roof benchmark . . . 66
29 Scordelis-Lo roof benchmark results . . . 66
30 Definition of the pinched cylinder benchmark . . . 67
31 Pinched cylinder benchmark results . . . 67
32 Definition of the pinched hemisphere benchmark . . . 68
33 Pinched hemisphere benchmark results . . . 68
34 Hinged cylindrical roof benchmark . . . 69
35 Open cylinder pullout benchmark . . . 70

36 Shell pendulum definition 71
37 Vertical displacement over time of the shell pendulum analysis 71
38 Oscillating clamped plate definition 72
39 Vertical displacement over time of the oscillating clamped plate analysis 72
40 Shell forces of the simply supported dome analysis 73
41 Mid-plane Von Mises stress results of the simply supported dome analysis 73
42 Mid-plane Von Mises stress plots of the simply supported dome analysis 74
43 Stresses (bottom surface) of the Navier supported plate under sinusoidal load . . 75
44 Paths for results: Red = X path and Green = Y path 76
45 Stresses of the Navier supported plate under uniformly distributed load 77
46 Composite barrel vault benchmark: cross layup 78
47 Composite barrel vault benchmark: angle layup 78
48 Composite clamped cylinder test definition 79
49 Composite clamped cylinder analysis convergence 79
50 Composite hinged cylindrical roof benchmark 80
51 Composite dynamic benchmarks 80
52 Stresses and Tsai-Wu results of the composite tensile test 81
53 Stresses and strains of the Navier supported ANDES-DKQ laminate under a sinusoidally distributed load 82
54 In plane stresses and strains of the Navier supported DSG laminate under a sinusoidally distributed load 83
55 Transverse shear stresses and strains of the Navier supported DSG laminate under a sinusoidally distributed load 84
56 Tsai-Wu reserve factor through the thickness of the Navier supported DSG laminate under a sinusoidally distributed load 85

List of Tables

1 Summary of selected element technologies 19
2 Selected formulations of implemented shell elements 20

List of Algorithms

1 DSG triangle element stiffness matrix pseudocode 41
2 DSG triangle element stress and strain recovery 44
3 ANDES-DKQ element stiffness matrix pseudocode 59
4 ANDES-DKT quadrilateral element stress and strain recovery 62

Bibliography

[1] Bhagwan D Agarwal, Lawrence J Broutman, and K Chandrashekhara.
Analysis and performance of fiber composites.
John Wiley & Sons, 2006.

[2] Fabian Rojas Barrales.
"Development of a nonlinear quadrilateral layered membrane element with drilling degrees of freedom and a nonlinear quadrilateral thin flat layered shell element for the modeling of reinforced concrete walls".
Dissertation. Los Angeles, California: University of Southern California, 2012.

[3] Klaus-Jürgen Bathe and Eduardo N. Dvorkin.
"A formulation of general shell elements—the use of mixed interpolation of tensorial components".
In: *International Journal for Numerical Methods in Engineering* 22.3 (1986), pp. 697–722.

[4] Jean-Louis Batoz, Klaus-JÜRgen Bathe, and Lee-Wing Ho.
"A study of three-node triangular plate bending elements".
In: *International Journal for Numerical Methods in Engineering* 15.12 (1980), pp. 1771–1812.

[5] Jean-Louis Batoz and Mabrouk Ben Tahar.
"Evaluation of a new quadrilateral thin plate bending element".
In: *International Journal for Numerical Methods in Engineering* 18.11 (1982), pp. 1655–1677.

[6] Ted Belytschko et al.
"Stress projection for membrane and shear locking in shell finite elements".
In: *Computer Methods in Applied Mechanics and Engineering* 51.1-3 (1985), pp. 221–258.

[7] P. G. Bergan and M. K. Nygård.
"Finite elements with increased freedom in choosing shape functions".
In: *International Journal for Numerical Methods in Engineering* 20.4 (1984), pp. 643–663.

[8] M. Bischoff et al.
“Models and Finite Elements for Thin-Walled Structures”.
In:
Encyclopedia of Computational Mechanics.
John Wiley and Sons, Ltd, 2004.

[9] Manfred Bischoff and Kai-Uwe Bletzinger.
“Improving stability and accuracy of Reissner-Mindlin plate finite elements via algebraic subgrid scale stabilization”.
In: *Computer Methods in Applied Mechanics and Engineering* 193.15 - 16 (2004), pp. 1517 –1528.

[10] Manfred Bischoff and Kai-Uwe Bletzinger.
“Stabilized DSG Plate and Shell Elements”.
In: *Trends in Computational Structural Mechanics* (2001), pp. 253 –263.

[11] Kai-Uwe Bletzinger.
Lecture notes in Plates.
2016.

[12] Kai-Uwe Bletzinger, Manfred Bischoff, and Ekkehard Ramm.
“A unified approach for shear-locking-free triangular and rectangular shell finite elements”.
In: *Computers and Structures* 75.3 (2000), pp. 321 –334.

[13] Robin Bouclier, Thomas Elguedj, and Alain Combescure.
“Efficient isogeometric NURBS-based solid-shell elements: Mixed formulation and -method”.
In: *Computer Methods in Applied Mechanics and Engineering* 267 (2013), pp. 86 –110.

[14] *Composites vs. Aluminum*.
American Composites Manufacturers Association.
2017.
URL: http://compositeslab.com/composites-compared/composites-vs-aluminum/.

[15] Eduardo N. Dvorkin and Klaus-Jürgen Bathe.
“A continuum mechanics based four node shell element for general non-linear analysis”.
In: *Engineering Computations* 1.1 (1984), pp. 77–88.

[16] Ralph Echter.
“Isogeometric Analysis of Shells”.
Dissertation. Stuttgart: Universitaet Stuttgart, 2013.

[17] C.A. Felippa.
Kirchhoff Plates: Field Equations.
2017.

[18] C.A. Felippa and C. Militello.
“Variational formulation of high-performance finite elements: Parametrized variational principles”.
In: *Computers and Structures* 36.1 (1990), pp. 1 –11.

[19] CA Felippa and KC Park.
“Fitting strains and displacements by minimizing dislocation energy”.
In: *Proceedings of the Sixth International Conference on Computational Structures Technology, Prague, Czech Republic*.
2002,
Pp. 49–51.

[20] Carlos A. Felippa.
“A study of optimal membrane triangles with drilling freedoms”.
In: *Computer Methods in Applied Mechanics and Engineering* 192.16 - 18 (2003), pp. 2125 –2168.

[21] William Hansen.
“The The Significance and Measurement of the Tsai-Wu Normal Interaction Parameter F12”.
MA thesis. Oregon State University, 1992.

[22] Bjørn Haugen.
“Buckling and Stability Problems for Thin Shell Structures Using High Performance Finite Elements”.
Dissertation. Colorado: University of Colorado, 1994.

[23] Woo-Young Jung and Sung-Cheon Han.
“An 8-Node Shell Element for Nonlinear Analysis of Shells Using the Refined Combination of Membrane and Shear Interpolation Functions,”
In: *Mathematical Problems in Engineering* 2013 (2013).

[24] Athanasios J Kolios and Stefano Proia.
“Evaluation of the reliability performance of failure criteria for composite structures”.
In: (2012).

[25] Ireneusz Kreja.
“A literature review on computational models for laminated composite and sandwich panels”.
In: *Open Engineering* 1.1 (2011), pp. 59–80.

[26] Mikko Lyly, Rolf Stenberg, and Teemu Vihinen.
“A stable bilinear element for the Reissner-Mindlin plate model”.
In: *Computer Methods in Applied Mechanics and Engineering* 110.3 (1993), pp. 343 –357.

[27] Richard H. Macneal.
“Derivation of element stiffness matrices by assumed strain distributions”.
In: *Nuclear Engineering and Design* 70.1 (1982), pp. 3 –12.

[28] Carmelo Militello and Carlos A. Felippa.
“The First ANDES Elements: 9-DOF Plate Bending Triangles”.
In: *Computer Methods in Applied Mechanics and Engineering* 93 (2 1991), pp. 217–246.

[29] P. Mohan.
“Development and applications of a flat triangular element for thin laminated shells”.
Dissertation. Virginia: Virginia Polytechnic Institute and State University, 1997.

[30] Mohammadreza Mostafa.
“A geometric nonlinear solid-shell element based on ANDES, ANS and EAS concepts”.
Dissertation. Colorado: University of Colorado, 2011.

[31] Alan T Nettles.
“Basic mechanics of laminated composite plates, NASA RP-1351”.
In: (1994).

[32] T. Nguyen-Thoi et al.
“A cell-based smoothed discrete shear gap method (CS-DSG3) using triangular elements for static and free vibration analyses of shell structures”.
In: *International Journal of Mechanical Sciences* 74 (2013), pp. 32 –45.

[33] Hieu Nguyen-Van, Nam Mai-Duy, and Thanh. Tran-Cong.
“An improved quadrilateral flat element with drilling degrees of freedom for shell structural analysis”.
In: *CMES: Computer Modeling in Engineering and Sciences* 49.2 (2009), pp. 81 –112.

[34] Ozden Ochoa and Junuthula Narasimha Reddy.
Finite element analysis of composite laminates.
Dordrecht ; Boston : Kluwer Academic Publishers, 1992.

[35] Gil Rama, Dragan Marinkovic, and Manfred Zehn.
“Efficient Co-Rotational 3-Node Shell Element”.
In: *American Journal of Engineering and Applied Sciences* 9 (2 2016), pp. 420–431.

[36] E. Ramm and W. A. Wall.
“Shell structures - a sensitive interrelation between physics and numerics”.
In: *International Journal for Numerical Methods in Engineering* 60.1 (2004), pp. 381 –427.

[37] Ekkehard Ramm.
Heinz Isler, Schalen: Katalog zur Ausstellung.
Zurich: vdf Hochschulverlag AG, 2002.

[38] Junuthula Narasimha Reddy.
Mechanics of laminated composite plates and shells: theory and analysis.
CRC press, 2004.

[39] J. C. Simo and M. S. Rifai.
“A class of mixed assumed strain methods and the method of incompatible modes”.
In: *International Journal for Numerical Methods in Engineering* 29.8 (1990), pp. 1595–1638.

[40] K.Y. Sze, X.H. Liu, and S.H. Lo.
"Popular benchmark problems for geometric nonlinear analysis of shells".
In: *Finite Elements in Analysis and Design* 40.11 (2004), pp. 1551 –1569.

[41] Wolfgang A Wall, Michael Gee, and Ekkehard Ramm.
"The challenge of a three-dimensional shell formulation-the conditioning problem".
In: *Proceedings of ECCM*.
Vol. 99.
2000.

[42] Henry T. Y. Yang et al.
"A survey of recent shell finite elements".
In: *International Journal for Numerical Methods in Engineering* 47.1-3 (2000).

[43] O.C. Zienkiewicz and R.L. Taylor.
The Finite Element Method. Volume 2: Solid Mechanics.
Oxford: Butterworth-Heinemann, 2000.

[44] Olgierd Zienkiewicz.
The Finite Element Method.
New York City: McGraw-Hill, 1977.

Declaration

I hereby declare that the thesis submitted is my own unaided work. All direct or indirect sources used are acknowledged as references. In addition, I declare that I make the present work available to the Chair of Structural Analysis for academic purposes and in this connection also approve of dissemination for academic purposes.

Ort, Datum, Signature